Physics Reports 1092 (2024) 1–64

Contents lists available at ScienceDirect

Physics Reports

journal homepage: www.elsevier.com/locate/physrep

Overview of the advances in understanding chaos in low-dimensional dynamical systems subjected to parameter drift

Parallel dynamical evolutions and "climate change" in simple systems

Dániel Jánosi [a,b,*], Tamás Tél [a,c]

[a] Department of Theoretical Physics, Eötvös Loránd University, Pázmány Péter Sétány 1/A, Budapest, H-1117, Hungary
[b] HUN-REN Institute of Earth Physics and Space Science, Csatkai Endre utca 6-8, Sopron, H-9400, Hungary
[c] HUN-REN-ELTE Theoretical Physics Research Group, Pázmány Péter Sétány 1/A, Budapest, H-1117, Hungary

ARTICLE INFO

Article history:
Received 22 June 2024
Accepted 19 August 2024
Available online xxxx
Editor: Itamar Procaccia

Keywords:
Chaos theory
Dynamical systems
Parameter drift
Snapshot chaotic attractor
Snapshot torus
Snapshot chaotic saddle

ABSTRACT

This paper offers a review while also studying yet unexplored features of the area of chaotic systems subjected to parameter drift of non-negligible rate, an area where the methods of traditional chaos theory are not applicable. Notably, periodic orbit expansion cannot be applied since no periodic orbits exist, nor do long-time limits, since for drifting physical processes the observational time can only be finite. This means that traditional Lyapunov-exponents are also ill-defined. Furthermore, such systems are non-ergodic, time and ensemble averages are different, the ensemble approach being superior to the single-trajectory view. In general, attractors and phase portraits are time-dependent in a non-periodic fashion. We describe the use of general methods which remain nevertheless applicable in such systems. In the phase space, the analysis is based on stable and unstable foliations, their intersections defining a Smale horseshoe, and the intersection points can be identified with the chaotic set governing the core of the drifting chaotic dynamics. Because of the drift, foliations and chaotic sets are also time-dependent, snapshot objects. We give a formal description for the time-dependent natural measure, illustrated by numerical examples. As a quantitative indicator for the strength of chaos, the so-called ensemble-averaged pairwise distance (EAPD) can be evaluated at any time instant. The derivative of this function can be considered the instantaneous (largest) Lyapunov exponent. We show that snapshot chaotic saddles, the central concept of transient chaos, can be identified in drifting systems as the intersections of the foliations, possessing a time-dependent escape rate in general. In dissipative systems, we find that the snapshot attractor coincides with the unstable foliation, and can consist of more than one component. These are a chaotic one, an extended snapshot chaotic saddle, and multiple regular time-dependent attractor points. When constructing the time-dependent basins of attraction of the attractor points, we find that the basin boundaries are time-dependent and fractal-like, containing the stable foliation, and that they can even exhibit Wada properties. In the Hamiltonian case, we study the phenomenon of the break-up of tori due to the drift in terms of both foliations and EAPD functions. We find that time-dependent versions of chaotic seas are not always fully chaotic, they

* Corresponding author at: Department of Theoretical Physics, Eötvös Loránd University, Pázmány Péter Sétány 1/A, Budapest, H-1117, Hungary.
E-mail addresses: daniel.janosi@ttk.elte.hu (D. Jánosi), tel@general.elte.hu (T. Tél).

https://doi.org/10.1016/j.physrep.2024.09.003
0370-1573/

can contain non-chaotic regions. Within such regions we identify time-dependent non-hyperbolic regions, the analogs of sticky zones of classical Hamiltonian phase spaces. We provide approximate formulas for the information dimension of snapshot objects, based on time-dependent Lyapunov exponents and escape rates. Besides these results, we also give possible applications of our methods e.g. in climate science and in the area of Lagrangian Coherent Structures.

Contents

1. Introduction

The problem of deterministic dynamical systems subjected to parameter drift, a subclass of non-autonomous systems, attracts increasing interest. Within the realm of dynamical systems theory only some modest attempts have been made in this direction, and the main motivation for their understanding comes from the need to describe physical processes of this type. One root in the background of this trend is certainly the phenomenon of climate change, since the forcing of the climate system, e.g. the CO_2 content, changes in time. There is by now a considerable climate-related literature on this (for reviews see, e.g., [1–4]). Within low-dimensional problems, perhaps the first field in which the importance of treating chaotic-like systems subjected to a driving of arbitrary time-dependence was consistently emphasized is fluid dynamics, and the concept of Lagrangian Coherent Structures, with some environmental concern [5–13]. Haller and coworkers emphasize that physical observations always extend over finite time intervals, therefore, theory should also be compatible with this: we have to abandon infinite-time asymptotes and accept that the time window of observation is an essential part of the problem. We share this view, and therefore take it over for general dynamical systems, implying a novel approach.

The subject of this paper is the dynamics of problems in the class of equations

$$\dot{\mathbf{x}} = \mathbf{F}(\mathbf{x}, t, \boldsymbol{\mu}(t)) \quad t_0 \le t \le t_{max}, \tag{1}$$

where $\mathbf{x}$ is a vector of state variables, $\mathbf{F}$ is a nonlinear function, where the explicit t-dependence, if present, is only of periodic character, and $\mu(t)$ represents a set of parameters of general time-dependence. The bounds on time express the constraint of finite observation time, which is assumed to be valid throughout the paper. It is also important to emphasize that Eq. (1) represents a *two-time, non-translation invariant* dynamics, i.e. a dynamics which does not depend only on time differences, rather both on the initial and final time instances, i.e. not only on $t_{max} - t_0$, but on both t_0 *and* t_{max} themselves.

In the approach presented here one must consider time-dependent phase space objects, due to the presence of changing parameters. We build on the following basic elements: *snapshot chaotic attractors, snapshot tori and chaotic seas*, and *snapshot chaotic saddles*, briefly introduced below. They all provide instantaneous patterns (hence the term snapshot), and arise via monitoring an *ensemble* of trajectories.

For *dissipative* cases, the concept of *snapshot attractors* has been available since 1990, originating from the work of Romeiras, Grebogi and Ott [14]. These attractors are instantaneous distributions of an ensemble of trajectories, initiated sufficiently (but not an infinite time) earlier, exhibiting chaotic dynamics and a fractal-looking appearance. A related concept is that of *pullback attractors* that appeared in the mathematics literature, see, e.g., [15–17], and became widely popularized in the context of climate science by Ghil and coworkers, even in low-dimensional cases [18,19]. A pullback attractor should be initialized in the remote past (i.e. the starting time of the integration tends to $-\infty$), and it represents the evolution of the attractor along the time axis. The term pullback refers to the property that by pulling back the initial conditions to the infinite past, the system will forget the initial conditions upon arriving at the present due to dissipation. An instantaneous slice of the pullback attractor corresponds to the snapshot attractor. Both types of attractors can be noisy or deterministic. We shall be interested in noiseless dynamical systems, and keep using the language of snapshot attractors. A number of papers appeared emphasizing the relevance of parameter drifts in problems describable by deterministic snapshot attractors, covering phenomena such as general aspects of dynamical systems [20–22], fluid dynamics [23–27], high dimensional problems [28–30], and epidemics in the presence of changing vaccination coverage [31]. In addition, there is a vast climate change related literature involving snapshot attractors, which will be detailed in Section 9.1. Here we only emphasize, that the nature of the process is chaotic, i.e., there exist many permitted co-evolving states, for which a qualitative term, the *theory of parallel climate realizations* was proposed in [32–34].

The *Hamiltonian* analogs of snapshot attractors, *snapshot tori and snapshot chaotic seas* were identified and determined in a simple time-continuous model and in a discrete-time version of such problems only recently, in [35,36], respectively. These time-dependent objects are the images of the ensembles of KAM tori and chaotic seas of the drift-free system taken in the non-autonomous dynamics. Pulling back the system to minus infinity does not help here, since initial conditions are never forgotten. Thus, "snapshot" is the only proper adjective for the description of instantaneous objects in non-dissipative contexts, which is why we keep using it for other objects as well, and avoid using the term pullback.

In *transient chaos* describing non-autonomous systems, the concepts of a *snapshot chaotic saddle* and its manifolds have been available for more than a decade (for a review see e.g. [37]). In this case, because of the parameter drift, the central concept of transient chaos, the chaotic saddle, is itself changing in time. Such objects have been identified in the process of dying chaos [38,39]. Their unstable manifolds were shown to play a central role in chaotic advection in open flows of arbitrary time dependence, as locations where advected particles accumulate while being transported away [6,26,40–42]. Even observational evidences have been provided for the existence of time-dependent, snapshot saddles in the dynamics of the advection of pollutant particles in the atmosphere [43], and in the solar plasma [44].

In [45], an attempt was made to provide a unifying picture for both dissipative and Hamiltonian non-autonomous chaos by identifying the time-dependent analogs of one of the most important concepts of standard chaos, stable and unstable manifolds of hyperbolic periodic orbits. Since, however, there is no hope for a systematic identification of a large number of the time-dependent analogs of periodic hyperbolic orbits, in [46], a further step was made towards generality: time-dependent stable and unstable *foliations* were shown to exist and being easily accessible in numerics. As we will

illustrate, these foliations coincide with the manifolds of snapshot chaotic saddles. A key object of chaos, a snapshot *Smale horseshoe* can then be identified as the transverse intersection pattern of these foliations.

In non-autonomous systems, since the phase space contains time-dependent objects, the usual chaos indicators cannot be computed. In [35], a method was given to determine one of such quantities: the time-dependent version of the largest Lyapunov exponent. The method is based on the investigation of the distance of trajectory pairs and averaging it with respect to the ensemble used. This results in the time-dependent function called the *ensemble-averaged pairwise distance (EAPD)*, and its slope can be considered an instantaneous, time-dependent Lyapunov exponent. The wide applicability of the concept of both the foliations and the EAPD method will be illustrated in this paper.

On an interpretative level, in [45], the concept of *parallel dynamical evolutions* was introduced as an essential feature of the dynamics of chaotic systems subjected to a non-negligible parameter drift, in analogy with the theory of parallel climate realizations mentioned above. Generalizing similar phrases of earlier papers (see e.g. [47,48]), paper [45] also claims that a dynamical system can be considered to undergo *its own climate change* whenever it is subjected to a parameter drift whose timescale is roughly comparable to that of the internal dynamics.

The present work offers a review, as well as an extension and generalization of the above-mentioned concepts to provide a better understanding of the dynamics of drifting systems. The main novel features treated here are the following:

- *time-dependent Lyapunov exponents* are defined as the derivative of the EAPD function, and are shown to characterize the evolution of the strength of chaos in non-autonomous systems in a wide variety of scenarios,
- *time-dependent natural measures* are identified and given a formal description not considered before,
- *time-dependent escape rates* are used to characterize chaotic saddles of changing intensity,
- *time-dependent information dimensions* of snapshot objects are estimated based on the existence of the natural measure, using time-dependent quantifiers and classical formulas,
- *time-dependent basins of attraction* are identified and studied in detail,
- *time-dependent non-chaotic regions* are found to typically exist within snapshot chaotic seas,
- *time-dependent non-hyperbolic regions* are shown to exist along the border of snapshot tori, and are identified as the analogs of the so-called "sticky" regions of autonomous chaotic Hamiltonian systems,

where in all bullet points the adjective "time-dependent" implies aperiodic time-dependence. A number of potential applications will also be given both within dynamical systems theory and in different disciplines of science.

In the bulk of the paper we focus on point mechanics, a subclass of (1), within which a general class of problems is described by the equation of motion

$$\ddot{x} = F(x, \dot{x}) + \varepsilon(t) d(x, \dot{x}, t), \tag{2}$$

describing one-dimensional problems, where F represents a nonlinear autonomous force which might be either of dissipative or Hamiltonian character, d is a driving assumed to be periodic in time, and ε is a prescribed driving amplitude. For $\varepsilon(t) = \varepsilon_0 =$ constant (2) describes driven nonlinear oscillators. We show that the presence of a time-dependent driving amplitude $\varepsilon(t)$, implying an *aperiodic* driving, leads to phenomena completely different from those known in autonomous or periodically driven systems, and requires a novel type of treatment, in particular if the dynamics is chaotic, examples of which are mentioned in the bullet points above.

We focus on a particular subclass of (1): the driving d is chosen to be state-independent and trigonometrically time-dependent. This latter feature enables us to take over a traditional method of dynamical systems theory: the stroboscopic map, i.e. observing the dynamics at integer multiples of the driving period. We note that this can also be done with any form of the time-dependent driving, simply by repeating the observation of the system at integer multiples of a convenient pre-selected time. The advantage of using the map is that it enables us to follow the dynamics on a two-dimensional plane. With a non-constant driving amplitude $\varepsilon(t)$ the strobospic map is of course itself non-autonomous, and can therefore be written as

$$\mathbf{x}_{n+1} = \mathbf{f}_n(\mathbf{x}_n, \mu_n) \quad n_0 \le n \le n_{max}. \tag{3}$$

This is the discrete-time analog of Eq. (1) in which the presence of the drift is reflected by index n on the mapping function $\mathbf{f}$ and parameter μ.

As for the nonlinear force F, besides a linear term, we choose a cubic nonlinearity in the x-variable, with a linear damping. We thus investigate the paradigmatic Duffing system [49–51], augmented with a time-dependent driving amplitude in the dimensionless equation of motion [45,46]

$$\ddot{x} = x - x^3 - 2\beta\dot{x} + \varepsilon(t)\cos\omega t, \tag{4}$$

with β as a damping constant, and ω being the driving frequency. The driving amplitude $\varepsilon(t)$ for simplicity, and in keeping with the analogy of climate change, is chosen to be *linearly changing* in time. Furthermore, the trigonometric time dependence mimics another feature present in climate, *seasonal periodicity*. As we will see, much insight can be gained even from this very simple case. We thus write

$$\varepsilon(t) = \varepsilon_0 + \alpha t, \quad 0 \le t \le t_{max}, \tag{5}$$

where α is the *rate* of the parameter drift. In discrete time, we write

$$\varepsilon_n = \varepsilon(t = nT) = \varepsilon_0 + \alpha n T, \quad 0 \le n \le n_{max}, \tag{6}$$

where $T = 2\pi/\omega$ is the driving period. Note that, in comparison with (1), we have arbitrarily set $t_0 = 0$ (and $n_0 = 0$ compared to (3)). We emphasize that in contrast to some earlier papers (see e.g. [39,52,53]), this monotonic change is kept *without* any crossover into an asymptotic plateau behavior (which would allow for a trivial identification of attractors). The introduction of minimum and maximum observation times in (5) and (6) is natural since the driving amplitude must not increase without any limit in reality, in accordance with the view of finite observation time.

Note that formally Eq. (4) can also be written in autonomous form, by considering three independent variables, described by

$$\dot{x} = v, \quad \dot{v} = x - x^3 - 2\beta v + \varepsilon(t)\cos\omega t, \quad \dot{t} = 1. \tag{7}$$

This is a set of three first-order differential equations, indicating that the phase space is three dimensional. This we shall call the (x, v, t) phase space.

A *scenario* is defined by the triplet of the initial driving amplitude, ε_0, the rate of the parameter drift, α, and the time, t_{max}, until which the dynamics is monitored, to which driving amplitude ε_{max} belongs. For convenience, we monitor the dynamics via the stroboscopic map (3). The maximum time of observation will be denoted in the map by n_{max}, and the stroboscopic phase space will be called the (x, v) phase space.

It is important to emphasize that our investigations are carried out in a *non-adiabatic* framework. The ratio

$$R = \frac{|\alpha|T}{\varepsilon_0} = \frac{|\alpha|2\pi}{\varepsilon_0\omega} \tag{8}$$

measures the significance of the parameter shift during a period compared to the initial driving amplitude. The condition of adiabaticity is most often expressed by means of parameter R as it being much smaller than unity, as described in classical mechanics [54], and also discussed in modern literature [55–57]. Here, the existence of a maximal allowed time in (5) makes the definition of another ratio possible as

$$R' = \frac{|\alpha|t_{max}}{\varepsilon_0} = \frac{|\varepsilon_{max} - \varepsilon_0|}{\varepsilon_0} = R n_{max}, \tag{9}$$

which measures the significance of the total shift during the scenario. For scenarios appearing in this paper, typical R values are on the order of 0.01, and R' values are on the order of unity or somewhat smaller (as n_{max} can be up to 100). We interpret this large value of R' as an indication for the *possibility* of non-adiabatic effects during the whole scenario.

The small (but certainly not very small) value of R at the same time makes the concept of adiabaticity not conclusive. In order to have a clear answer, the introduction of a further concept, that of *tracking* can be beneficial. Tracking holds if a phase space object monitored during the scenario remains close to its frozen, i.e. non-drifting counterpart all the time. The concept was introduced in relation to rate induced tippings by Ashwin and coworkers [58], describing phenomena where tracking breaks down upon increasing the rate of parameter drift. In this context, traditionally attractors – most often regular attractors – are tracked. We are going to extend the tracked objects to saddles (including chaotic ones), and to tori and chaotic seas, in the Hamiltonian context. As it turns out, for typical small R values tracking can be broken for certain phase space objects. Thus, we define a *non-adiabatic phase space object* as one for which tracking is broken in the course of the scenario. This formulation implies that within the same scenario the concept of adiabaticity might depend on the object monitored (on e.g. attractors or saddles), which will be illustrated by examples in the paper. Furthermore, we say that in our case one can consider a scenario to be non-adiabatic when the corresponding R' value is large, and there are objects for which tracking is broken. The conclusion is that in a complex system where chaos is present, single numbers like (8) or (9) are not sufficient to decide if a process is adiabatic or not.

The paper is organized as follows. Section 2 investigates the simplest, non-chaotic snapshot objects, *moving points* of different stability properties, in the phase space of (4). Already here, special emphasis is put on the fact that snapshot objects *differ from their analogs in the non-drifting counterpart*, indicating non-adiabaticity. Explicit results are obtained in the limit of weak driving, with technical details relegated to Appendix.

Section 3 reviews the basic characteristics of time-dependent chaos and presents the main features of chaotic snapshot attractors, snapshot tori and snapshot chaotic seas. To this end foliations, EAPD functions and time-dependent Lyapunov exponents, as well as time-dependent natural measures are used. It is again shown, now in the context of chaotic systems, that drifting systems are significantly different from frozen, i.e. non-drifting ones at the same driving amplitude.

Section 4 is devoted to finding a general relation between snapshot chaotic saddles, and snapshot attractors and chaotic seas. We demonstrate the so-called sprinkler method widely used to obtain chaotic saddles in time-independent cases. We then apply this method to drifting systems in both the dissipative and Hamiltonian cases. We show that snapshot attractors and chaotic seas certainly contain snapshot chaotic saddles, which are characterized by time-dependent escape rates. We also show that the stable and unstable manifolds of the saddles run within the stable and unstable foliation of the problem.

Section 5 discusses advanced features found in dissipative systems. We find that simple, time-dependent attractor points can coexist with chaotic motion, within a single snapshot attractor. The chaotic set in such a snapshot attractor is

shown to be an extended snapshot chaotic saddle. We also study the basin of attraction of the regular attractors. These basins are found to accumulate on the fractal-looking stable foliation of the chaotic component of the snapshot attractor. Having an example with three simple attractors, the boundaries appear to exhibit the Wada property, and the three sets together occupy the phase space in a space filling way.

Concerning Hamiltonian systems (Section 6), we point out that the break-up of a snapshot torus starts at the first instant from where the stable foliation, iterated backwards, first intersects the torus at its initial state. We find that the chaotic set can be approximated either by the unstable or the stable foliation, depending on whether the strength of chaos is increasing or decreasing within the scenario. Furthermore, we identify non-chaotic regions inside the snapshot chaotic sea, occupying the areas where the snapshot chaotic sea does not correspond to the snapshot chaotic saddle. Within non-chaotic regions, time-dependent non-hyperbolic regions are found to exist along the boundary of yet existing snapshot tori, thus exhibiting similar behavior as traditional non-hyperbolic regions.

An effort estimating the dimension of snapshot objects is given in Section 7. Traditional relations for the information dimension are applied using the time-dependent Lyapunov exponents and escape rates determined earlier.

In Section 8 we look at some theoretical aspects that could benefit from or are variations of the results discussed here. Typical non-linear scenarios are reviewed, and their relevance is explored. Undriven non-autonomous Hamiltonian systems of four-dimensional phase spaces are discussed, a so far untouched class where we expect that the same methods could be applied after considering Poincaré sections. Another type of investigated systems are undriven autonomous dissipative systems, exhibiting so-called doubly transient chaos where all motion ceases eventually, while the dynamics of the phase space shows similarities to the previous system type.

In Section 9 we provide possible applications of the discussed concepts. Regarding climate science, we discuss different approaches applied for understanding the climate snapshot attractor, while expecting the EAPD method to be useful, despite the very high dimensionality of the attractor. When looking at Lagrangian Coherent Structures (LCSs), one can make a correspondence between hyperbolic LCSs and stable and unstable foliations, as well as elliptic LCSs and snapshot tori, the break-up of which can even be observed following experimental and oceanic eddies. Galaxy dynamics is often described by simple Hamiltonian maps, providing an example for undriven non-autonomous Hamiltonian problems. In plasma physics, the dynamics of particles in a tokamak reactor can easily be transformed into a Hamiltonian dynamical system. If this is non-autonomous, all of the methods described here could be beneficial, especially in determining time-dependent non-hyperbolic regions concerning the transport of runaway electrons. Lastly, in relation to engineering applications, we discuss a case with the drift in the driving frequency, where snapshot attractors similar to the ones presented in this paper are found.

Finally, we give our conclusions in Section 10.

2. Snapshot points: the simplest moving objects with regular dynamics

2.1. The significant difference between the drifting and non-drifting dynamics

The conservative force of the equation of motion (4) derives from a double-well potential of the form

$$V(x) = -x^2/2 + x^4/4. \tag{10}$$

The origin is a local maximum, and corresponds to an unstable state, while the minima at $x = \pm 1$ represent stable states. In the undriven case, they are a hyperbolic fixed point and two fixed point attractors in the dissipative, two elliptic fixed points in the Hamiltonian case, respectively. Fig. 1 shows the shape of the potential (10) (panel a), as well as the structure of the corresponding Hamiltonian phase space (panel b), with the elliptic and hyperbolic fixed points, as well as the separatrix highlighted. In the presence of a *strictly periodic driving* they become periodic orbits of analogous stability properties (unstable limit cycle, limit cycle attractors and neutrally stable limit cycles), represented by a hyperbolic point and two point attractors or elliptic points on a stroboscopic map taken with the period of the driving. In the general case of *aperiodic* driving, the analogs of these orbits are themselves points moving with an aperiodic time-dependence, and are aperiodically jumping even on stroboscopic maps [35,45]. To express this difference, these moving points are called *snapshot points* [35], and are defined as points which *keep their stability character* (unstable, stable, neutral) *for long times*. The three classes mentioned are *snapshot hyperbolic points (SHPs), snapshot nodal points (SNPs)* or snapshot attractor points, and *snapshot elliptic points (SEPs)*.

It is worth knowing that in the physics literature a nonchaotic, regular snapshot attractor was identified by Pikovsky [59] 40 years ago, under the term "synchronization by common noise", an SNP in our terminology. The mathematics literature goes back to [60] and ranges up to recent publications [16,17,61] with many examples on moving regular attractors. SNPs of low order differential equations were also used for illustrating climate-related problems, see e.g. [18,33,62]. SHPs have been considered in the LCS literature (see e.g. [7,63–65]), termed as moving hyperbolic points, distinguished hyperbolic orbits, or hyperbolic cores. We intend to apply the adjective "snapshot" to emphasize the common feature of all such points: time-dependence. The literature on *rate induced tippings* (see e.g. [58,66–70]) initiated by Ashwin and co-workers, also investigates moving attractor points, when the system is in the process of transitioning from one state to another, i.e. tipping. The case of snapshot elliptic points was first treated in [35].

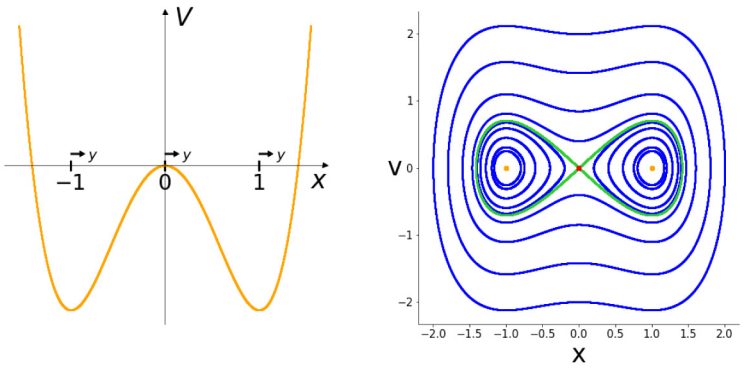

Fig. 1. (a) The shape of the double-well potential (10) with the direction of the small deviations y about the extrema used in (11) indicated by arrows (not to scale). The time-dependent location $y^*(t)$ of snapshot points appears primarily in variable y in the linearized approach. (b) Phase space trajectories in the undriven Hamiltonian case, with the elliptic fixed points denoted by orange dots, the hyperbolic fixed point denoted by a red dot, and the separatrix shown in light green.

Table 1
Summary of the different snapshot points and the corresponding parameters, along with their coordinates in the original variable (x), and their Lyapunov exponents. The particular form of $y^*(t)$ depends on $\varepsilon(t)$.

Type of snapshot point	Snapshot hyperbolic point (SHP)	Snapshot nodal point (SNP)	Snapshot elliptic point (SEP)
Parameters in y^*	$\omega_0^2 = -1, \beta \geq 0$	$\omega_0^2 = 2, \beta > 0$	$\omega_0^2 = 2, \beta = 0$
x coordinate	$x^*_{SHP}(t) = y^*(t)$	$x^*_{SNP}(t) = \pm 1 + y^*(t)$	$x^*_{SEP}(t) = \pm 1 + y^*(t)$
Instability exponent	$\lambda_\pm = -\beta \pm \sqrt{\beta^2 + 1}$	$\lambda_\pm = -\beta \pm \sqrt{\beta^2 - 2}$	$\lambda_\pm = \pm i\sqrt{2}$

To have more insight on snapshot points, we linearize the equation of motion (4) about the origin and about ± 1 to obtain the equation

$$\ddot{y} = -\omega_0^2 y - 2\beta\dot{y} + \varepsilon(t)\cos\omega t, \tag{11}$$

where y denotes the small deviation about the extrema of the potential, see Fig. 1(a), and ω_0^2 is the second derivative of potential (10) in these points (see e.g. [71]): $\omega_0^2 = -1$ and $\omega_0^2 = 2$ corresponds to the behavior about the unstable and the stable points, respectively. This implies that we consider the weak driving limit of $|\varepsilon(t)| \ll 1$, so that the investigated orbits do not leave the vicinity of the aforementioned points, at least for some time. In a linear differential equation like (11), the snapshot points correspond to *particular* solutions, denoted by $y^*(t)$, of the inhomogeneous equation which have *no* exponential contribution form the solutions of the homogeneous equation, as shown e.g. in [33,45]. Solution $y^*(t)$ depends of course on the time-dependent $\varepsilon(t)$ driving amplitude.

The stability properties of the possible solutions of (11) *only* follow from its homogeneous part. Table 1 summarizes these for the different snapshot orbits, also providing the results in the original x variable. The last line displays the instability or Lyapunov exponents which are *independent* of time along the trajectory of the snapshot point. The stability property along $y^*(t)$ follows form the homogeneous part of (11) and is therefore the same as that of the *undriven* problem, and is hence independent of t and of ω.

For the scenario $\varepsilon(t) = \varepsilon_0 + \alpha t$ of (5) we search for y^* in the form of

$$y^*(t) = a_0\varepsilon(t)\cos\omega t + b_0\varepsilon(t)\sin\omega t + a_1\dot{\varepsilon}(t)\cos\omega t + b_1\dot{\varepsilon}(t)\sin\omega t \tag{12}$$

since a substitution of this into the linear Eq. (11) leads to no additional types of terms. The substitution $\alpha = \dot{\varepsilon}$ is made in order to remain compatible with other types of parameter drift. The solution is of course valid as long as $|\, y^*(t)\,| \ll 1$. The general scheme of the approach is outlined in the Appendix, where also the explicit forms of the coefficients are given, along with the case of quadratically time-dependent driving amplitudes. It is important to see that the coefficients depend only on ω_0, ω, β, but *not* on the scenario, and have *no free parameters*. The dependence on the driving scenario $\varepsilon(t)$ only appears via the terms explicitly written out in (12).

It is worth mentioning that the periodic orbits of the frozen system with a *fixed* driving amplitude ε are given by

$$y^*_{frozen}(t) = a_0\varepsilon\cos\omega t + b_0\varepsilon\sin\omega t \tag{13}$$

with the *same* amplitudes a_0, b_0 as in (12). This clearly shows that y^* at $\varepsilon(t) = \varepsilon$ and y^*_{frozen} belonging to ε are different: *the snapshot points differ from their frozen counterparts* at any instant of time.

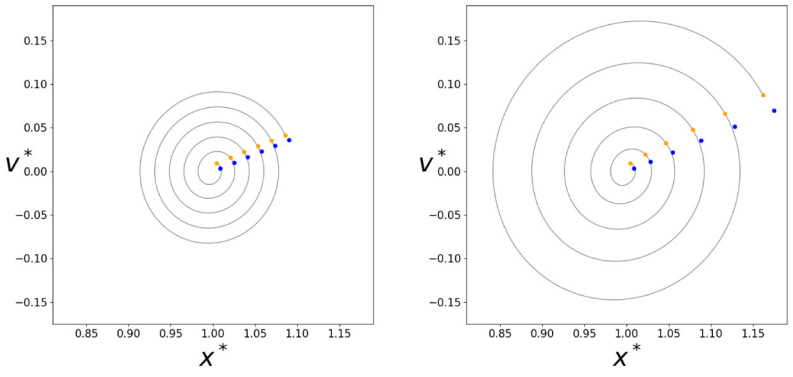

Fig. 2. Stroboscopic images of SNPs (orange dots) close to $(x, v) = (1, 0)$ compared with the frozen fixed point attractors (blue dots) of the corresponding ε values, for $\beta = 0.2$ and $\omega = 1$. The images in (a) correspond to a linear drift with $\varepsilon_0 = 0.01$, $\alpha = 0.003$ and $n_{max} = 5$ ($\varepsilon_{max} = 0.104$) where the coordinates of the orange dots follow from (17) with $x_n^* = 1 + y_n^*$. The blue dots follow the same rule with $\alpha = 0$. In panel (b) a case of quadratic drift is shown with the same ε_0, $\alpha_1 = \alpha$, and $\alpha_2 = 0.0001$ as the coefficient of the quadratic term (see Appendix). In the former case, the SNPs are not the same as the frozen attractors but are translated by a constant distance, while for the quadratic drift their distance grows in time as well. The gray lines denote the continuous trajectory of the SNPs in the respective cases. Parameters R and R' (Eqs. (8) and (9)) turn out – applied formally to the quadratic case as well – to be 2 and 10, hence the drifting process is not adiabatic, also supported by the observation that a spiraling curve is qualitatively different from an ellipsis or a circle.

In order to find the phase space pattern of the moving snapshot points, let us rewrite (12) as

$$y^*(t) = A\varepsilon(t)\cos(\omega t + \phi) + B\dot{\varepsilon}(t)\cos(\omega t + \theta) = A\varepsilon(t)\cos(\omega t + \phi) + y_0^*(t). \tag{14}$$

where the new parameters follow from the previous ones from trigonometric identities, and $y_0^*(t)$ depends only on the rate of the parameter drift. Similarly, the velocity v^* of the snapshot point can be written as

$$v^*(t) = \dot{y}^*(t) = -A\omega\varepsilon(t)\sin(\omega t + \phi) + v_0^*(t), \tag{15}$$

where $v_0^*(t)$ contains all the terms proportional to $\dot{\varepsilon}(t)$. One sees therefore that the phase space trajectory fulfills

$$(y^* - y_0^*)^2 + \frac{(v^* - v_0^*)^2}{\omega^2} = A^2\varepsilon^2(t), \tag{16}$$

the trajectory is *spiral-like* around the moving center $(y_0^*(t), v_0^*(t))$. For comparison, the periodic orbits of the frozen system are *ellipses* around the origin. In the particular case of $\omega = 1$, the spirals are of *Archimedean* type: $r(t) = A\varepsilon(t)$ where r is the distance from the moving center, while the periodic orbits are *circles*, $r = A\varepsilon$, where r is the distance from the origin.

On a stroboscopic map, at times $t = nT = n2\pi/\omega$, the coordinates of the snapshot points are from (12)

$$y_n^* = a_0\varepsilon_n + a_1\alpha, \quad v_n^* = b_0\omega\varepsilon_n + (a_0 + b_1\omega)\alpha, \tag{17}$$

where abbreviation (6) has been used. Since both expressions depend linearly on n (via (6)) the snapshot point moves along a straight line segment. The linear shift on the map, just like the spiraling orbit in continuous time, are valid for any snapshot point.

Out of the three possible choices, in Fig. 2 we show the trajectory of moving attractor points (SNPs), in gray, as well as their stroboscopic images in orange. The latters are compared with the frozen fixed point attractors (blue) belonging to the same driving amplitude as the orange points. Panel (a) shows the case of linear drift (5), while panel (b) exhibits the results obtained for the quadratic drift $\varepsilon(t) = \varepsilon_0 + \alpha_1 t + \alpha_2 t^2$, see Appendix. Note the considerable difference between the SNP and the fixed point attractor, which might even increase in time (panel b).

The difference between the frozen and the snapshot points is present at time zero too (where $\varepsilon_0 \neq 0$), even if the derivative of the amplitude is continuous. This suggests that the endpoint of a general scenario valid for $t \leq 0$ will not continuously join the snapshot orbit valid for $t \geq 0$: all snapshot points typically *jump* when a new scenario starts at $t = 0$.

2.2. The jumps of snapshot orbits at the beginning of scenarios

Here we investigate a peculiar feature not yet fully explored in the literature concerning regular snapshot orbits. As such, readers mainly interested in chaotic aspects might skip to Section 3. We ask the question if a snapshot point can be continuously continued when a new scenario starts in (11) with (5) at $t = 0$. Let the (y, v) coordinates of the endpoint at time $t = 0$ of a previous scenario be denoted by (y_{end}, v_{end}). The general solution of the inhomogeneous Eq. (11) is the

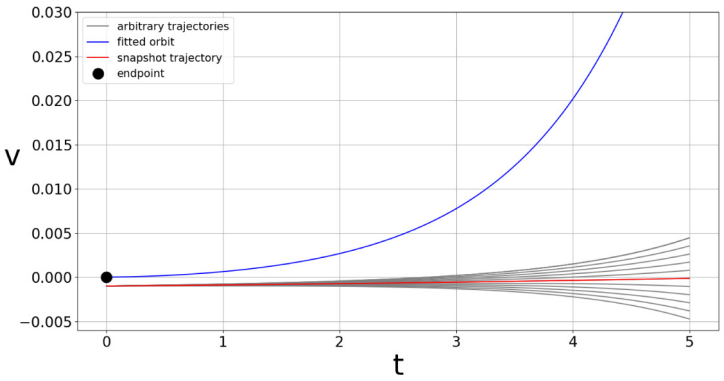

Fig. 3. Jump of the solution from a previous scenario to the orbit of a snapshot point in a hyperbolic case with $\varepsilon_0 = 0.01$, $\alpha = 0.001$, $\beta = 0.1$, $\omega = 0.1$. Blue curve: orbit fitted to the endpoint of the previous scenario, red curve: snapshot hyperbolic point, SHP, valid for $t \geq 0$, gray curves: 11 nearby trajectories initiated uniformly distributed around the SHP.

sum of the general solution of the homogeneous part and a particular solution. By means of the snapshot point solution given in (12), which is at the same time a particular solution, this reads as

$$y(t) = c_+ e^{\lambda_+ t} + c_- e^{\lambda_- t} + y^*(t). \qquad t \geq 0 \tag{18}$$

A fitting of this to the endpoint at $t = 0$ leads to the constraints

$$y_{end} = c_+ + c_- + y^*(0), \tag{19}$$

$$v_{end} = c_+ \lambda_+ + c_- \lambda_- + v^*(0), \tag{20}$$

where the stability exponents are taken from Table 1 for the different snapshot points, and $y^*(0)$, $v^*(0)$ are the initial coordinates of the snapshot point solution (12). This set of equations uniquely determines c_+, c_-, and the solution $y(t)$ obtained with these coefficients we call the orbit fitted to the endpoint $y_{fitted}(t)$, a smooth continuation of the snapshot orbit ending in (y_{end}, v_{end}). We shall investigate the relation of this fitted orbit to the snapshot orbit $y^*(t)$ existing for $t \geq 0$ with driving amplitude (5). For simplicity, we choose the endpoint coordinate and its derivative as the frozen limit cycle solution at fixed driving amplitude ε_0, $y^*_{frozen}(0)$ given by (13) at $t = 0$. We thus illustrate a new facet of the difference between the frozen and the drifting dynamics, and emphasize that, when joining two scenarios, only the endpoints count, which could follow from *any* type of scenario in the $t < 0$ past.

We start the investigation with the hyperbolic behavior since this is the basic building block of chaotic dynamics. The blue fitted curve in Fig. 3 deviates quickly from the SHP (red curve). This strong difference is due to the fact that the instability exponent λ_+ is *positive* for this case, see Table 1, and represents an exponentially exploding contribution, always present unless $c_+ = 0$ in exceptional cases. The tendency for deviation from the SHP is present for any typical initial condition, even for nearby ones, as the set of gray curves illustrate. We thus conclude that *the orbit of the snapshot hyperbolic points cannot be continuously fitted to previous ones*. The only exception is when the functional form of $\varepsilon(t)$ is the same before and after $t = 0$.

Fig. 4 shows similar plots for the snapshot nodal point. The fitted blue trajectory itself converges to the red SNP, just as the 11 neighboring trajectories initiated at $v^*(0)$ but with initial coordinates differing from $y^*(0)$. Note that any other initial condition would lead to a similar convergence to the SNP. The frequency of the oscillation is the imaginary part of $\lambda_\pm$, $\omega' = \sqrt{2 - \beta^2} \approx 1.411$ leading to a period $T' = 4.45$. Note that the driving frequency is chosen to be $\omega = 0.1$, in order to illustrate the separation of the period $T = 2\pi/\omega = 62.8$ of the SNP solution from that of any other. All other possible solutions oscillate, in the process of converging to the snapshot solution, with the frequency ω'. The decay is governed by β, leading to a characteristic e-folding relaxation time 10. After a few multiples of this, all trajectories are close to the orbit of the snapshot nodal point in harmony with its attracting character. This means that here a continuous fitted orbit *does* exist, and this orbit (the blue curve) itself can be considered as a snapshot attractor. This is in harmony with the spirit of pullback attractors [16,17] according to which such an attractor should be a continuous solution of the problem existing over long stretches of time. Note, however, that the blue attractor is oscillating much faster before reaching the SNP solution than the latter, there is thus a change in the character of the attractor's dynamics. We prefer to accept only the SNP as *the* snapshot attractor, meaning that it does not continuously fit the previous one, and consider the oscillatory part of the blue curve a *transient* to the SNP, just like any of the gray curves.

The elliptic case is the $\beta \to 0$ limit of the attracting one. Fig. 5 is similar to Fig. 4 without of course any sign of relaxation. The blue curve is oscillating about the snapshot elliptic point, representing a quasiperiodic motion about it, just like all the gray curves. No continuous fit to the previous snapshot solution is possible, because $\lambda_\pm$ has no negative real part (see Table 1).

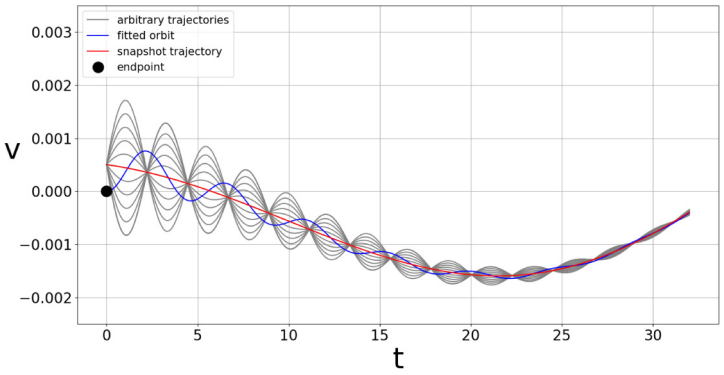

Fig. 4. Jump of the solution from a previous scenario to the orbit of a snapshot point in an attracting case with $\varepsilon_0 = 0.01$, $\alpha = 0.001$, $\beta = 0.1$, $\omega = 0.1$ Blue curve: orbit fitted to the endpoint of the previous scenario, red curve: snapshot nodal point, SNP, valid for $t \geq 0$, gray curves: 11 nearby trajectories initiated uniformly distributed around the SNP. The time interval shown is half the period of the SNP solution.

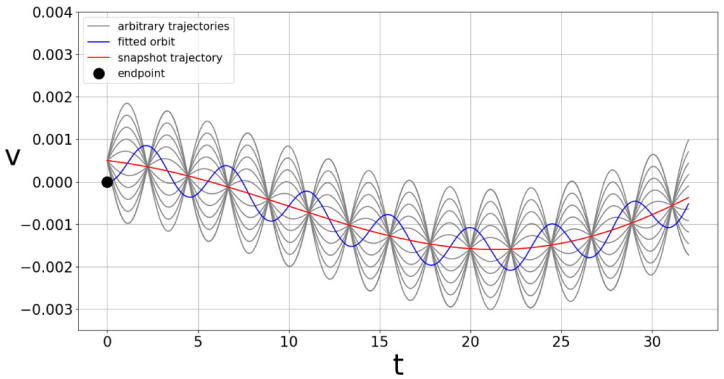

Fig. 5. Jump of the solution from a previous scenario to the orbit of a snapshot point in an elliptic case with $\varepsilon_0 = 0.01$, $\alpha = 0.001$, $\omega = 0.1$. Blue curve: orbit fitted to the endpoint of the previous scenario, red curve: snapshot elliptic point, SEP, valid for $t \geq 0$, gray curves: 11 nearby trajectories initiated uniformly distributed around the SEP. The time interval shown is half the period of the SEP solution.

These considerations suggest the view that all snapshot points typically jump when a new scenario starts at $t = 0$. There is thus *no need* to know the past before $t = 0$. This observation helps accepting the relevance of finite observational time windows, and allowing for any time, e.g. $t = 0$, to be the starting point of observation. At the same time it also illustrates that we cannot speak about pullback hyperbolic and elliptic points, and that this is not a must in relation to attractor points either. In general, when $\varepsilon(t)$ is not small, all snapshot points should be searched numerically for $t > 0$. A peculiarity of the case of point attractors is that the search is certainly successful since any initial point converges to the attractor after some convergence time t_c (a few times $1/\beta$ in our example). We can thus be sure that time t_c after initialization the snapshot attractor is reached even if the past before the instant of initialization is not known. The features discussed in this section, as we shall see later, hold for chaotic snapshot objects, as well. In particular, the convergence time t_c will be relevant in the context of chaotic attractors too.

3. Basic features of chaotic drifting systems

In chaotic systems subjected to parameter drifts of non-negligible rate a number of basic methods of standard chaos theory cannot be applied:

- The famous periodic orbit expansion [72] has to be discarded since no periodic orbits exist.
- Individual trajectories are not representative as they differ from any member of the trajectory ensemble used [39], and are numerically unreliable. Furthermore, not even a single long trajectory would have any meaning (even if it was allowed), since it would not trace out the snapshot attractor or the chaotic sea, see next point.
- Such systems are non-ergodic, time and ensemble averages are different as detailed in [14,73,74], one cannot fully rely on the celebrated paper of Eckmann and Ruelle [75]. The finite observation does not provide sufficient temporal, single-trajectory based statistics, therefore the ensemble view allowing for accurate statistics is superior to the single-trajectory view. This means that chaotic snapshot objects and their natural measures can only be provided by means of ensembles evolved from different initial conditions, governed by the *same* dynamics.

- Strict fractality cannot exist because really fine-scale structures cannot be generated with finite-term simulations, and, furthermore, self-similarity across all scales is lost, as it was shown in [76].

Furthermore, the finite observational time in physical processes is of enhanced importance in chaotic cases, since the opportunity of comparison with asymptotic results is not possible because of the perpetual qualitative change of the dynamics.

The aim of this section is to explore methods which can, nevertheless, be used for the identification of chaotic structures of the phase space in such cases, both for dissipative and Hamiltonian dynamics. After presenting the characteristic phase space objects in Section 3.1, two general approaches are discussed, one about the geometrical organization of the phase space, via *foliations* (Section 3.2), while the other is more quantitative, based on the ensemble-averaged pairwise distance (EAPD) function (Section 3.3), providing a generalization of Lyapunov exponents to *time-dependent Lyapunov exponents*. We discuss the relevance of natural measures and present the theoretical background with numerical illustrations in Section 3.4. As an extension of Section 2, we show in Section 3.5 the essential differences between drifting and non-drifting irregular dynamics.

3.1. Snapshot objects in the phase space

In dissipative systems, the relevant phase space objects are snapshot attractors. The initial shape of the ensemble used for generating them can be completely arbitrary, since every point eventually converges to the attractor. In practice, usually an extended ensemble (i.e. a grid initial condition) is used, which we will also do often. The number of trajectories in such an extended initial ensemble will be denoted as N_{ext}.

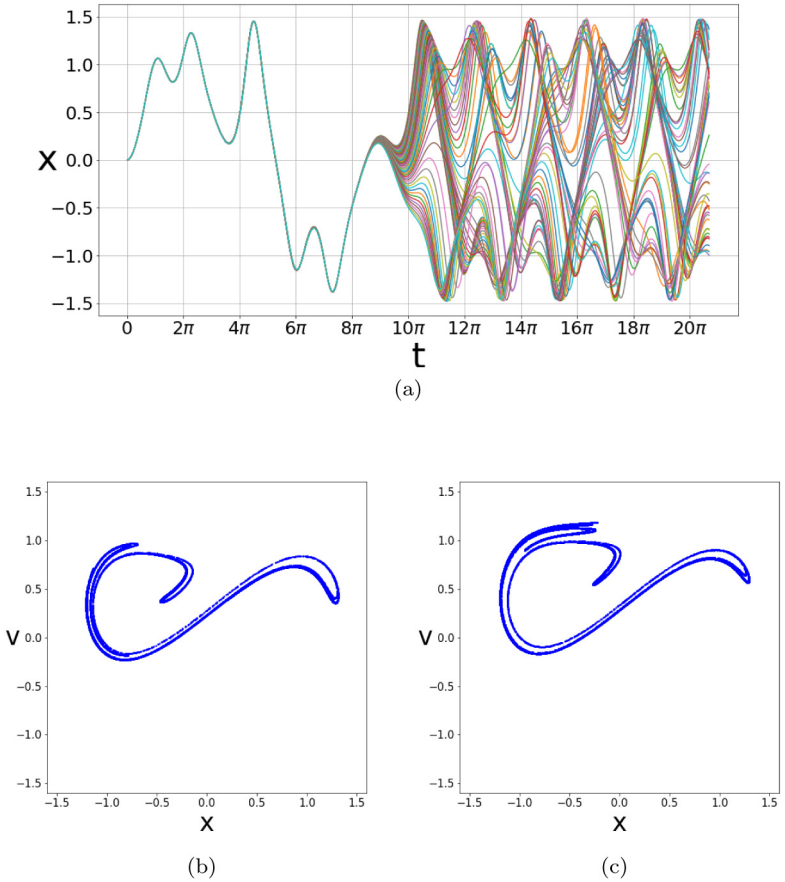

Fig. 6. Snapshot attractor in the scenario $\varepsilon_0 = 0.4$, $\alpha = 0.00045$, $n_{max} = 100$ ($\beta = 0.2$, $\omega = 1$). (a) Plume diagram evolving from 50 initial conditions uniformly distributed between $x_0 = -0.001, \ldots, 0.001$, $v_0 = 0$. (b)–(c) The shape of the ensemble, i.e. the snapshot attractor, at times $n = 60{,}100$, from an extended initial distribution centered on the origin, of linear size 4, with $N_{ext} = 40000$.

In Fig. 6(a) we numerically illustrate[1] that system (4) exhibits sensitivity to initial conditions by showing a plume diagram for an ensemble of initially close trajectories distributed on an x-interval of length $2 \cdot 10^{-3}$, not discernible by naked eye. We choose the parameter drift according to scenario $\varepsilon_0 = 0.4$, $\alpha = 0.00045$, $n_{max} = 100$, in which $R = 0.007$ and $R' = 0.7$ of (8) and (9). These values allow for non-adiabatic features, which will be detailed in Section 3.5. The other parameters of (4) are $\beta = 0.2$ and $\omega = 1$, and the latter choice will be kept throughout the paper. After about 4.5 periods, a deviation between the trajectories, plotted with different colors, becomes visible, and within one additional period a full spread over a large range of x values occurs. The difference between parallel dynamical evolutions from nearby initial conditions has started to show. Note, however, that the graphs of Fig. 6(a) might also depend on the numerical accuracy, as another consequence of chaos, thus reliable statements can only be made by means of ensemble statistics.

In panels (b) and (c) the snapshot attractor is shown on the stroboscopic (x, v) phase plane with a much larger ensemble than in panel (a) after $n = 60$ and 100 periods (at the values of around $\varepsilon_{60} = 0.569$ and $\varepsilon_{100} = 0.682$ respectively[2]). A change in its shape is clearly observable. It is at this point where the qualitative view of parallel dynamical evolutions can be illustrated. Any dynamical evolution leads to a blue point on panel (b) and their set is going to evolve further into the pattern of panel (c) some time later. They do not have a meaning on the individual level, only their ensemble represents physics and it traces out the snapshot attractor.

We emphasize that the convergence to the snapshot attractor requires some time t_c. This convergence time can be estimated by running a second ensemble from a remote initial distribution from that of the first ensemble. In practice, the convergence time is the time after which the averages of the phase space variables x, v taken with respect to the

[1] In all numerical integrations throughout the paper, the *odeint* differential equation solver of the *scipy* Python library was used. Note that in order to obtain statistically accurate results in chaotic cases, the relative and absolute tolerances have to be set smaller than e.g. 10^{-10}.

[2] The ε_n values will always be given with 3-digit accuracy.

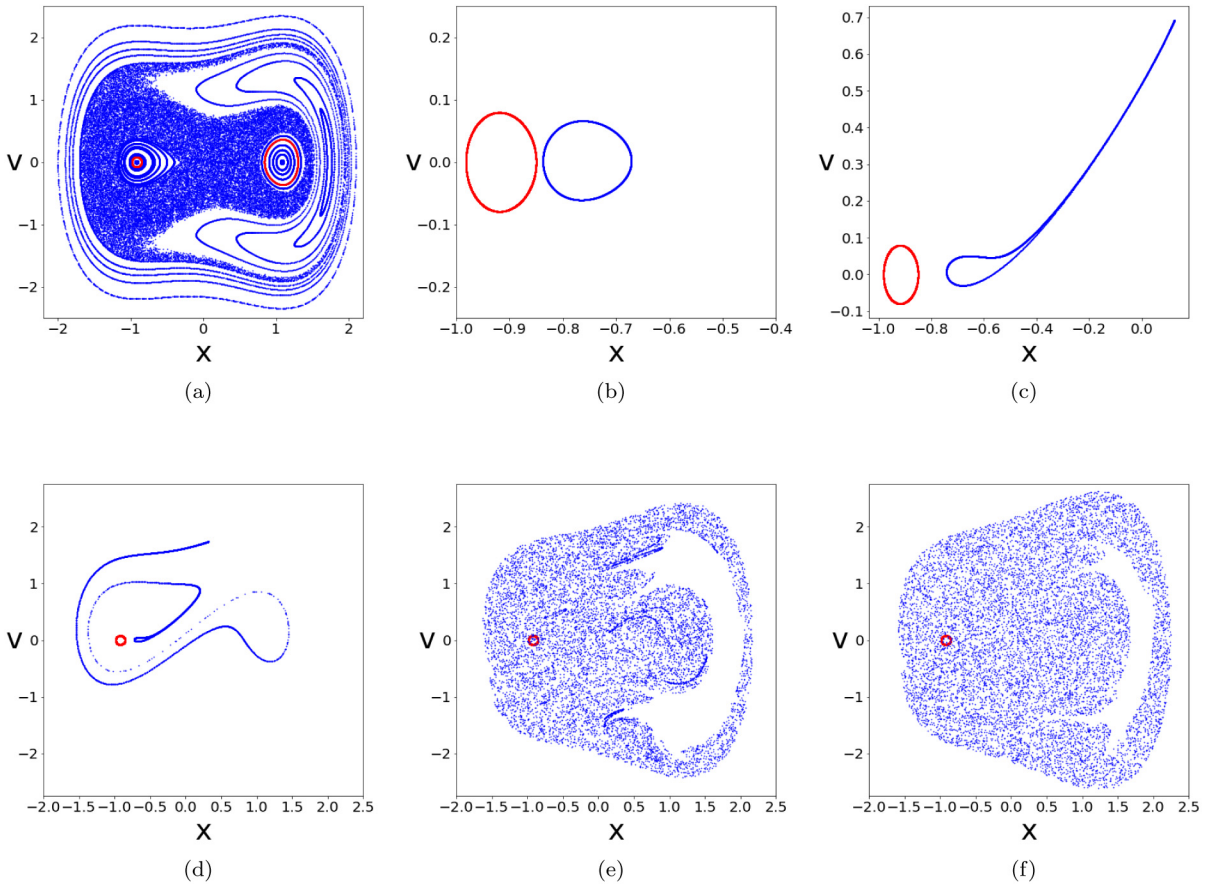

Fig. 7. Evolution of a snapshot torus. (a) Phase portrait of the drift-free problem generated form 41 uniformly distributed initial conditions between $x_0 = -2 \ldots +2$ with $v_0 = 0$ and followed up to $N_{tor} = N_{cha} = 2000$ iterations at $\varepsilon_0 = 0.08$, $\beta = 0$. The red torus on the left belongs to $x_0 = -0.85$, the other red torus to $x_0 = 1.3$. (b)–(f) Evolution of the left red torus in the scenario $\varepsilon_0 = 0.08$, $\alpha = 0.0005$, $n_{max} = 100$ of (21), generated from an ensemble of $N_{tor} = 10000$ members on it, shown at time instants $n = 40, 52, 53, 65, 100$. The red curve shows in all the panels the original shape of the left torus of panel (a).

ensembles are practically identical, although time dependent (a more detailed discussion of the convergence time will be given in Section 3.4). In our case t_c is about 7 periods.

The main observation from panels (b), (c) is that the phase space is entirely dominated by one object, no other snapshot attractors (neither simple nor chaotic) coexists with the one shown. We call this type of snapshot attractor a *chaotic snapshot attractor* [46]. Note, however, that besides relying on indicators such as the extended nature and the fractal-like appearance of the attractor, as well as the fast divergence of trajectories in the plume diagram, at this point we are not in the position to quantitatively prove if the attractor is chaotic, and if so, how much chaotic it is. This problem will be discussed below in Sections Section 3.3.

In Hamiltonian systems the basic components of the time-independent (divided) phase spaces are KAM tori and chaotic seas. If we use these as non-trivial initial ensembles in the time-dependent system (the number of trajectories in them denoted by N_{tor} and N_{cha} respectively), we obtain snapshot tori and snapshot chaotic seas that, just like the snapshot attractor, also change their shapes in time. In addition to this, a delicate interplay can also take place by the intrusion and breaking up of tori into chaotic seas, as first observed in [35].

Before proceeding, it is worth writing down the Hamiltonian corresponding to Eq. (4) with $\beta = 0$:

$$H(x, p, t) = \frac{p^2}{2} + V(x) - x\varepsilon(t)\cos\omega t, \tag{21}$$

where $V(x)$ is given by (10). The equation of motion appears in this context in the form of the canonical equations [54,71]. One of these is $\dot{x} = \partial H/\partial p = p$. According to Liouville's theorem, which is also valid for non-autonomous Hamiltonians, the phase space area is conserved in the (x, p) plane. Because of the coincidence of p and v this also holds for the (x, v) plane in this case.

In panel (a) of Fig. 7 the phase space is shown before the scenario starts. A number of initial conditions are used in a simulation of length 2000 periods without any drift to reveal the phase space patterns. Of particular importance will

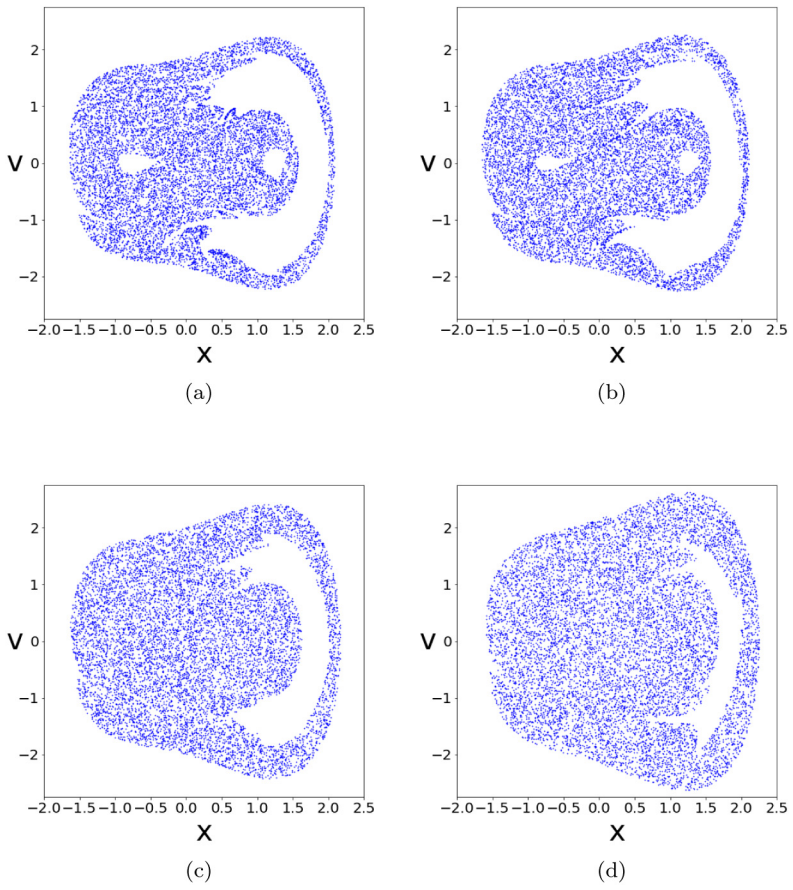

Fig. 8. Snapshot chaotic sea in the scenario of Fig. 7. The initial chaotic sea is obtained from the initial condition $x_0 = 0.1$, $v_0 = 0$ with $N_{cha} = 10000$ iterates, and corresponds to the dense blue region in Fig. 7(a). Panels (a)–(d) show the image of this set after $n = 35, 40, 65, 100$ time units, respectively, in the scenario. Observe the close similarity of the shape of the snapshot chaotic sea in panel (d) to Fig. 7(f), the shape of the snapshot torus at the same instant.

be the red torus on the left since the points constituting it will be used as initial conditions, and thus its shape will be followed in the course of the scenario (the one on the right will be used later in Section 6.1).

A first example of the evolution of a snapshot torus in the phase space is provided by panel (b) in scenario $\varepsilon_0 = 0.08$, $\alpha = 0.0005$, $n_{max} = 100$ where the original torus (at $\varepsilon_0 = 0.08$) and its image (in blue) after 40 periods (at $\varepsilon_{40} = 0.206$) are shown. The torus has moved to the right and became slightly deformed. 12 periods later (at $\varepsilon_{52} = 0.243$) the torus is stretched and elongated (panel c). Due to Liouville's theorem, the area of the snapshot torus remains unchanged. Within one more period it stretches in a folded way over a broad range of the phase space (panel (d) at $\varepsilon_{53} = 0.246$, note the difference in the scales along the axes). The shape has no resemblance with a usual torus, the snapshot torus is said [35,36] to have started to break up. The last two panels (e and f) show later images of the red torus, after 65 and 100 periods (at $\varepsilon_{65} = 0.284$ and $\varepsilon_{100} = 0.394$ respectively). Their appearance is similar to that of chaotic seas in traditional chaos, but changes with time. The scatter of points in panels (e), (f) indicates that a huge number of strongly different dynamical evolutions became possible in the course of the scenario.

The process illustrated by panels (b)–(f) shows that tracking certainly breaks down by instant $n = 52$ (panels c). The process is *non-adiabatic* for the snapshot torus followed here. The corresponding parameters are $R = 0.04$ and $R' = 4$. Section 3.5 discusses adiabaticity in more detail for the Hamiltonian case as well.

The appropriate concept in relation to chaos in drifting Hamiltonian systems is that of snapshot chaotic seas. To illustrate their relation with snapshot tori, in Fig. 8 we show the images of the chaotic sea of Fig. 7(a). These are slightly deformed and enlarged images of the original one, shifted to the right. This is not in contradiction with Liouville's theorem, because the tori originally encircling the chaotic sea also break up and become entrained into it. A comparison with Fig. 7(b), taken at the same time, indicates no relation between the snapshot torus and the chaotic sea at $n = 40$ (panel b). By time 65, however (Fig. 8(c)), the two sets become quite similar, and at $n = 100$ (Fig. 8(d)) the chaotic sea and the image of the torus (panel (f) of Fig. 7) are practically identical. We can thus conclude that the broken up torus becomes mixed across the full snapshot chaotic sea.

3.2. Time-dependent foliations

In search for a topological identification of time-dependent chaos, and a possible relation to time-dependent Smale horseshoes, the stable and unstable manifolds of time-dependent hyperbolic points (SHPs in the terminology of Section 2) appear to be natural candidates, but the identification of a large number of such orbits is hopeless. In [46], therefore, a method without a need for the existence of such orbits was proposed. It relies on the concept of stable and unstable *foliations*, well known within the framework of the mathematical description of traditional chaos (see e.g. [77–80]). Qualitatively speaking the unstable (stable) foliation is a *direction field* of long-term stretching in the forward (backward) dynamics. In other words, unstable and stable foliations are curves whose tangents point in the local stretching direction of the forward (backward) dynamics. In contrast to the field lines of e.g. electromagnetism or streamlines of velocity fields, foliations are not necessarily defined in any point of the phase space as strong stretching is an exceptional property. A Smale horseshoe [81] arises if the two foliations intersect each other roughly perpendicularly. Intersection points remain intersection points in the course of the dynamics, and are of special importance since they are considered to be the points of a (not necessarily attracting) chaotic set. These points are subject to two contradictory types of dynamics, stretching and compression at the same time, their time evolution is therefore "hesitant", i.e. chaotic.

Foliations turn out to be easy to generate in systems subjected to parameter drift. The method leading to such a snapshot foliation is the following [46]: take a large number N_{fol} of points distributed on a not necessarily short interval of length dl inside the chaotic region and follow their time evolution. To obtain the unstable foliation belonging to discrete time instant n, the initialization should be at time instant $n - k$, where k is an auxiliary time parameter. In principle it should be large, but the constraint of finite-time observation sets an upper limit on it. Its value can be on the order of 10 time units in practice. This value turns out to be sufficient enough for showcasing the main role foliations play in these systems. For the stable foliation the algorithm is similar, just the time-reversed dynamics should be followed between time units $n + k$ and n.

Before proceeding, let us make a general comment. Given an observational time window $[0, n_{max}]$, the simulation of the unstable foliation belonging to time instant n cannot go further back in the past than $n = 0$, i.e. $k \leq n$, while that of the stable foliation cannot go further into the future than n_{max}, implying $k \leq n_{max} - n$. In cases when the same auxiliary time k is used for both foliations at time n, the maximum allowed value of it is

$$k_{max} = \begin{cases} n, & \text{for} \quad n < n_{max}/2, \\ n_{max} - n & \text{for} \quad n > n_{max}/2. \end{cases} \tag{22}$$

It should be noted, that in our approach the foliations cannot be considered exact, due to the limit on k; with a given observational window, one cannot expect better results than those consistent with the window. Nevertheless, an exponential convergence is expected towards them due to the strong contraction in the perpendicular direction, around their intersections at least. Thus, in the example of constructing both foliations with the same k, an error can only follow from using a k value smaller than k_{max} given in (22), but it is expected to be small due to the exponential convergence. Thus, the inaccuracy in generating the foliations can indeed be exponentially small in the auxiliary time k. We note that a vanishing k value is certainly not sufficient for generating foliations, thus relation (22) implies that a faithful representation

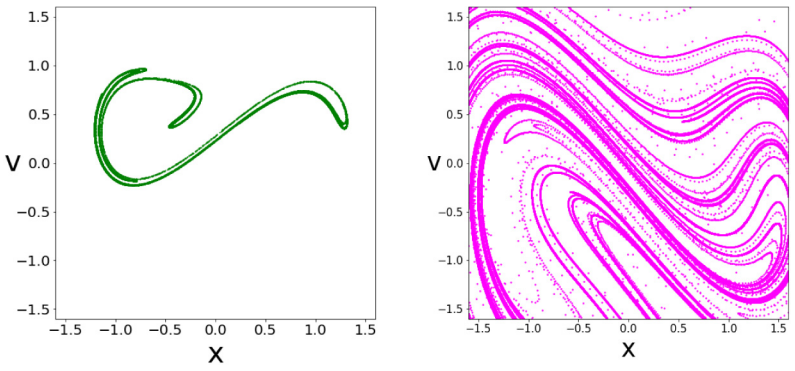

Fig. 9. Snapshot (a) unstable and (b) stable foliations in the dissipative scenario of Fig. 6, at time $n = 60$, using $k = 40$. The initialization occurs on 3 vertical segments of length $dl = 0.2$ around points $(-1, 0.75)$, $(-0.5, 0.25)$, $(0.75, 0.75)$ chosen to be close to the snapshot attractor, with (a) $N_{fol} = 20000$ and (b) $N_{fol} = 10^6$ points. In the latter case, at every step new points are added along the same segments.

of both foliations is hopeless at the ends of the observation time window. Even when using different ks, at the endpoints of the window one of the foliations is impossible to construct.

Due to the finite window, the intersection points of the foliations are also not exact, and their number is certainly finite in the simulation, but their topology might indicate dynamical complexity. We shall consider as an indication of the existence of a chaotic set if a large number of transverse intersection points between the foliations are present. In a few cases where SHPs can be determined at least approximately, like e.g. in the weak driving limit of our model studied in Section 2, their unstable (stable) manifolds can be determined in the usual sense as curves emanated from small balls about the SHP in forward (backward) dynamics, and were numerically found to run parallel to the corresponding foliations in [38,45,46].

For the dissipative scenario of Fig. 6 the foliations are given, for time instance $n = 60$, in Fig. 9. Both turn out to be strongly folded, a feature characterizing usual chaos as well. For the unstable foliation (green curve), panel (a), initialization is taken on 3 segments of length $dl = 0.2$ with $N_{fol} = 20000$ particles on each, at time instant $k = 40$ earlier. Numerically, the pattern observed on the scale of the figure is *independent* of the used auxiliary time k (if it is not too small), as well as parameters dl, N_{fol}. It can thus be meaningfully considered as the unstable foliation of the dynamics. This foliation should be compared with the blue attractor of panel (b) of Fig. 6. The concurrence suggests the rule: *a snapshot attractor is nothing but the snapshot unstable foliation*, provided no other attracting objects are present. Strictly speaking, this is a consequence of the attracting nature of the snapshot attractor, but using initial line segments instead of areas provides a filament-based approximation of the attractor.

The stable foliation is expected to be more extended, therefore it is generated with $N_{fol} = 10^6$ points on the 3 segments, with the backward iteration started at time instant $n+k = 100$. In order to keep the number of points high enough in the range shown (due to the anti-dissipation in the time-reversed dynamics, there is considerable escape to remote regions of the phase space), at every step new points are initiated on the 3 segments originally chosen. The pink foliation obtained this way in panel (b) is consistent with the view that the *snapshot stable foliation is space filling* as long as no other attractors exist. On the image of Fig. 9(b), of course, a considerable amount of white regions can be observed, where seemingly no point of the foliation exists. This however is only a numerical effect, as our simulation cannot fully keep up with the very strong anti-dissipation of the phase space, not even with the point-inserting method described above. Anticipating the space-filling nature of the snapshot stable foliation (to be illustrated in Section 4.2), any point of the snapshot attractor is thus an intersection of the two foliations: *chaos populates densely the attractor*.

The algorithms for the Hamiltonian case are similar. Fig. 10 shows both snapshot foliations for the scenario of Figs. 7 at $n = 35$. Here the large scale shapes of both foliations are found to be independent of k (if its value is not too small). A striking observation is that the *snapshot stable and unstable foliations are different*, due to the lack of time-reversal symmetry, which would be impossible without the parameter drift. Observe that the shape of the stable foliation is different than the snapshot chaotic sea of Fig. 8(a), however, the unstable foliation is similar to it: the latter of course has a more filament-like appearance, while the chaotic sea appears more bulky, but their overall shape is indeed the same. In this scenario, the asymmetry in the role of the stable and unstable foliations is a consequence of the torus break-up mechanism. Another surprising feature is that, while chaos exists at the intersections of the foliations, but, given their difference in shape, these intersections cannot be present everywhere, i.e. chaos does not need to be dense in snapshot chaotic seas. A detailed investigation of these issues will be given in Section 6.

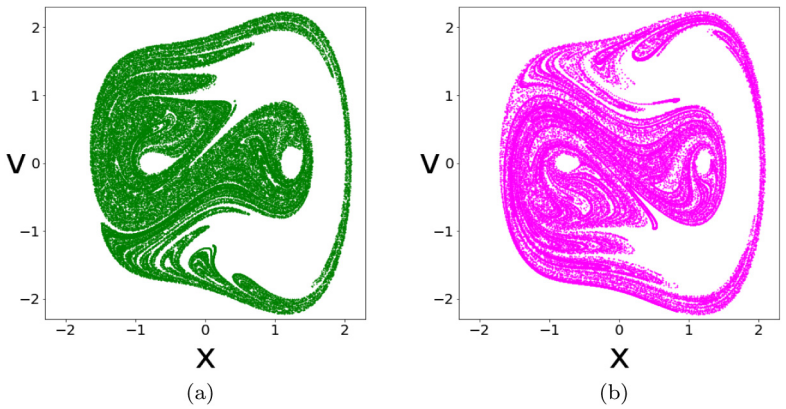

Fig. 10. Snapshot (a) unstable and (b) stable foliations in the Hamiltonian scenario of Fig. 7, shown at time instant $n = 35$, with $k = 10$. Initialization occurs on 3 vertical segments of length $dl = 0.2$ around points $(-0.5, 0.5)$, $(0, 0)$, $(0.5, -0.5)$, chosen to be inside the chaotic sea, with $N_{fol} = 20000$ points.

3.3. Ensemble-averaged pairwise distance and time-dependent Lyapunov exponents

An important feature of drifting systems is that long-time limits are meaningless because of the finite observation windows. Traditional Lyapunov exponents [82] are thus ill-defined. For the quantitative identification of chaos in such systems, an entropy-based answer is available in [83], along with time-average-based approaches [84,85], and one based on the size of the snapshot attractor [38]. A general moral of ensemble simulations is that time averages should be avoided. In this spirit, a quantity reflecting sensitivity to initial conditions, an analog of the largest Lyapunov exponent was proposed [35,45,46] to be extractable from the so-called *ensemble-averaged pairwise distance* (EAPD) function, whose local slope can be considered an *instantaneous* Lyapunov exponent.

The function ρ of the EAPD in continuous time t is defined as

$$\rho(t) = \langle \ln r(t) \rangle, \tag{23}$$

where the average is taken over an ensemble of trajectories. To any member of the ensemble a test particle is ordered at an initial distance r_0. Quantity $r(t)$ is the dimensionless phase space distance between a test particle and an ensemble member at time t. In discrete time, such as on the stroboscopic map used here, only the instants $t = nT$ are considered, and the formula becomes

$$\rho_n = \langle \ln r_n \rangle, \tag{24}$$

where $r_n = r(t = nT)$. The EAPD function is in general nonlinear (in t or n), the possibility of considering the local slope as an instantaneous Lyapunov exponent arises from the analogy with traditional chaos, where the function ρ_n vs n is linear and its slope is the usual (largest) Lyapunov exponent. Strictly speaking, the local slope at $n > 0$ can only be considered a Lyapunov exponent if the typical distance between pairs is very small. In practice, we say that it is sufficient if the average distance is still much smaller than the global size of the investigated phase space object. We therefore only associate any meaning with the slope if this is the case. In our examples, we consider this as a cutoff value at $1/100$ the size of the available dimensionless phase space at the end of the scenario ($\approx e^{-5}$) when applicable.[3] Note that for times shorter than the convergence time to the attractor t_c (found to be about 7 periods in Section 3.1) the ensemble averaging is not reliable.

Fig. 11 provides examples of EAPD functions. Panel (a) corresponds to the ensemble of the snapshot attractor arising in the scenario of Fig. 6. A monotonous increase is observed up to about time 40, after which a plateau follows indicating that the initially very nearby points ($r_0 = \sqrt{2} \cdot 10^{-10}$, a value kept throughout the paper) have spread over the snapshot attractor of size unity. The kink at about $n = 25$ turns out to correspond to the fact that the system passes through a periodic window of the bifurcation diagram of the drift-free problem around $\varepsilon = 0.46$, see later Fig. 14 in Section 3.5. The slope in this region is smaller than outside, but clearly still positive, indicating chaos in this region as well.

The cutoff value is indicated by the horizontal dashed line. The overall message of the local slopes (red lines) given in panel (a) is that the attractor is strongly chaotic initially, then, in the range of the kink, it becomes weakly chaotic,

[3] Following only one set of point pairs, as we do, the EAPD function sooner or later breaks this constraint, since the algorithm works with non-infinitesimally small distances. This breaking could be remedied by discarding the test particles when their distance to the ensemble members exceeds a threshold, and ordering new test particles to the trajectories again at r_0 distance. We argue however, that aside from being easier to compute, the slope of the EAPD used is also a good approximation of, and therefore can be called as, an instantaneous Lyapunov exponent.

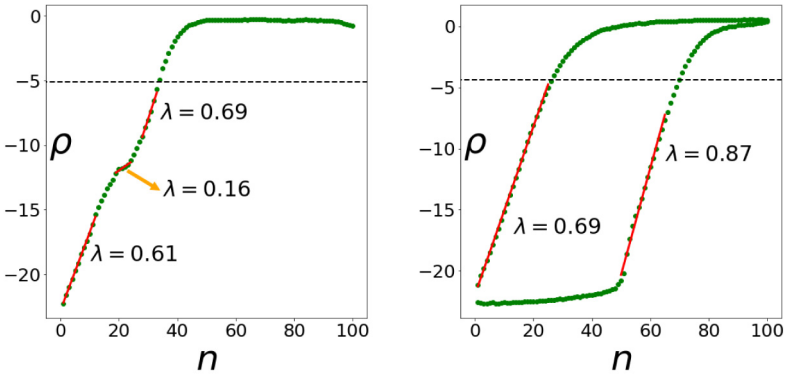

Fig. 11. EAPD curves (a) for the snapshot attractor in the dissipative scenario of Fig. 6 and (b) for the Hamiltonian scenario of Figs. 7 and 8. The left and the right curve belongs to the snapshot chaotic sea and to the snapshot torus, respectively. The initial distance is $r_0 = \sqrt{2} \cdot 10^{-10}$ in all cases. The dashed line is the cutoff value beyond which the slope of the EAPD curve cannot be considered an instantaneous Lyapunov exponent. Note that the function in panel (a) provides here the same slope before and after the convergence time (about 7).

while around the end of the region permitted for extracting instantaneous Lyapunov exponents, chaos is strong again, even somewhat stronger than initially.

In the Hamiltonian case (panel b) two curves are shown. The left one corresponds to the chaotic sea evolving in the scenario of Fig. 8. The right one is based on the ensemble of the snapshot torus followed in Fig. 7. Initially, function ρ hardly changes, but about $n = 52$, where the torus break-up starts, the function crosses over into a rapid increase. The slope of the latter is slightly larger than that of the one on the left, indicating that the chaotic sea into which the torus became entrained is not the same as the one governing the first about 30 periods, the one after time instant 52 appears to be more chaotic. Another thing to note is that the image of the snapshot torus after 65 iterations, shown in Fig. 7(e), only closely resembles a snapshot chaotic sea, since the distribution of the points is not as uniform as the chaotic sea of Fig. 8(c), some denser regions can be observed. Looking at Fig. 11(b), this state of the snapshot torus fits into the break-up process: $n = 65$ is in the middle of the slope of the right EAPD curve, meaning that at this point the break-up has already started, but is not yet completed. In contrast, at $n = 100$ the EAPD curve has already started to go into saturation, indicating the end of the break-up process, as the near-uniform distribution of points in Fig. 7(f) illustrates. The dashed line again indicates the cutoff value.

The qualitative statement according to which the slope of the EAPD curve is an instantaneous average largest Lyapunov exponent can be made quantitative by introducing the notation $\lambda(t)$ and writing

$$\lambda(t) = \dot{\rho}(t). \tag{25}$$

In discrete time we write

$$\lambda_n = \frac{\Delta\rho}{\Delta t} = \rho_{n+1} - \rho_n = \rho_n', \tag{26}$$

since $\Delta t = 1$ in stroboscopic units, and we have introduced the notation ρ_n'. The relevance of the discrete time form is emphasized by the usage of the stroboscopic view throughout the paper. The prime in (26) denotes the discrete time derivative with respect to the time unit T defining the stroboscopic map. In our case, $T = 2\pi/\omega$. The numerical value of $\lambda(t)$ thus corresponds to λ_n/T. These relations are valid as long as ρ does not exceed the threshold value.

Examples for the discrete time Lyapunov exponent are given in Fig. 12, based on the derivatives[4] of the EAPD curves of Fig. 11. The example starting with a pronounced positive value characterizes the chaotic snapshot attractor and has a dip around $n = 21$, where the system passes through parameters ε belonging to a periodic window. The other curve initially oscillates about values close to zero, in harmony with the existence of a snapshot torus, but switches over to large positive values after the break-up, i.e., the conversion of the torus into chaos. The EAPD curve characterizing the snapshot chaotic sea in Fig. 11(b) is not converted into a λ_n sequence since it would provide practically constant values up until the cutoff.

In dynamical systems with one positive Lyapunov exponent, there should exist a λ' negative one as well because of the overall phase space contraction. Their relation is determined by the phase space contraction rate σ. The latter is given

[4] The discrete time derivatives here and in every following case in the paper are calculated using the *polyfit* and *polyder* functions of the *numpy* Python library. The algorithm fits a polynomial function to the whole investigated dataset, where the order of the polynomial depends on the particular data. The derivative is then evaluated from this polynomial at the datapoints.

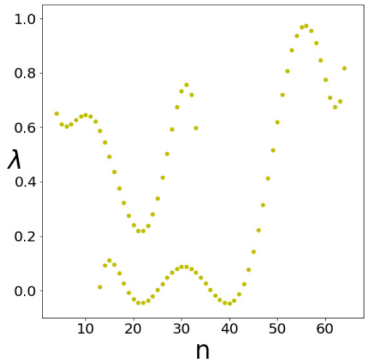

Fig. 12. Time-dependent largest Lyapunov exponent λ_n in the stroboscopic picture for the chaotic snapshot attractor of Fig. 11(a) (shorter curve) and for the torus break-up process described by the lower graph in Fig. 11(b) (longer curve). The Lyapunov exponents are calculated until the EAPD curves reach the cutoff value.

by the negative divergence of the vector given by the right hand sides of the first order autonomous equations of motion. In our case, based on (7), we obtain

$$\sigma = -\mathrm{div}\mathbf{F} = -\left(\frac{\partial \dot{x}}{\partial x} + \frac{\partial \dot{v}}{\partial v} + \frac{\partial \dot{t}}{\partial t}\right). \tag{27}$$

Evaluating the partial derivatives, from (7) we get

$$\sigma = 2\beta, \tag{28}$$

meaning that the phase space contraction rate is only set by the constant dissipation rate. Its value is the same in both the three and two dimensional phase spaces, since there is no contraction along the time axis. Then we have the special case of a constant phase space contraction rate, in which case in traditional chaos the second Lyapunov exponent λ' can be expressed by means of the first one and the phase space contraction rate [82,86] as

$$\lambda + \lambda' = -\sigma. \tag{29}$$

Since this relation has to hold for any time instant, for time-dependent Lyapunov exponents we have

$$\lambda(t) + \lambda'(t) = -\sigma. \tag{30}$$

From here

$$|\lambda'(t)| = \lambda(t) + \sigma. \tag{31}$$

The modulus of the second Lyapunov exponent is obtained by shifting the value of the first one with σ. In discrete time

$$|\lambda'_n| = \lambda_n + \sigma T, \tag{32}$$

where in our case $T = 2\pi/\omega$. The modulus of the time-dependent second Lyapunov exponent of the snapshot attractor in Fig. 6 is thus obtained by adding $\sigma T = 2\beta 2\pi = 0.8\pi \approx 2.5$ to the λ_n values of Fig. 12, using (28) with $\beta = 0.2$ and $\omega = 1$. In such cases the EAPD curve determines the time-dependence of both Lyapunov exponents.

3.4. Natural measure

Chaotic systems are unpredictable, individual time series are not representative, but a probabilistic description of the dynamics is always possible, and can be made arbitrarily precise. The background is that a so-called *time evolution equation* (or generalized Liouville equation) can be ordered to any dynamical system [72,82,86,87], as worked out mainly for traditional chaos. It specifies the time evolution of a P phase space probability density. The ideas we present here are specifically applied for drifting chaotic systems.

In time-continuous cases, for the equation of motion (1) with a time-dependent vector $\mathbf{F}(t)$ this time-evolution equation is of the form of

$$\frac{\partial P}{\partial t} = -\mathrm{div}(\mathbf{F}(t)P), \tag{33}$$

where we did not indicate the explicit $\mathbf{x}$ and $\mu(t)$ dependence present in (1). This is nothing but the *Fokker–Planck equation* (see e.g. [87–89]), expressing the conservation of probability, thus ensuring normalization. Here it appears *without* the diffusion term, of course, since we deal with deterministic systems (there is no noise term in (1)). To any smooth

initial distribution $P_0(\mathbf{x})$ valid at time t_0, this equation determines the distribution $P(\mathbf{x}, t, t_0)$ for any time $t > t_0$. (In an autonomous case ($\mathbf{F}$ time-independent) P only depends on the time difference $t - t_0$, but in drifting systems, it is a bivariate function of t and t_0.)

To gain some insight, let us factorize the right-hand side and write

$$\frac{\partial P}{\partial t} = -\mathrm{div}\mathbf{F}\, P - (\mathbf{F}\mathrm{grad})\, P = \sigma(\mathbf{x}, t)P - (\mathbf{F}\mathrm{grad})P, \tag{34}$$

where we have used that the negative divergence of the flow $\mathbf{F}$ is the phase space contraction rate $\sigma \geq 0$ (27). Bringing the last term to the left, what appears there is the hydrodynamic derivative D/Dt of P in the flow provided by $\mathbf{F}$ in the phase space:

$$\frac{DP}{Dt} = \frac{\partial P}{\partial t} + (\mathbf{F}\mathrm{grad})\, P = \sigma(\mathbf{x}, t)P. \tag{35}$$

This simple form says that if we are *co-moving* with a phase space element, the density on it is continuously increasing in time (exponentially, if σ is constant). This is of course due to the contraction of the phase space volume (with rate σ, which vanishes in Hamiltonian cases) since the "material content" in a phase space volume does not change. In this picture, the support of P is moving along a deterministic path, and converges, therefore, to the snapshot attractor, or traces out the chaotic sea. Consequently, the density also converges to the density of the nature measure, the density on either the snapshot attractor or the snapshot chaotic sea. This density we are going to denote by P^* but indicate that it depends on time, and write therefore $P^*(\mathbf{x}, t)$. (In traditional chaos $P^*(\mathbf{x})$ - just like $\mathbf{F}$ - is independent of time, or depends on it at most periodically).

The more conventional view provided by (33) (as opposed to (35)) provides the density $P(\mathbf{x}, t)$ at a fixed location. As any solution of the Fokker–Planck equation converges to a limiting distribution, this P converges to the natural measure $P^*(\mathbf{x}, t)$, provided only one exists. This convergence is determined by the *spectrum* of the linear operator $-\mathrm{div}(\mathbf{F}(t)\cdot)$ (sometimes also called the transfer operator) on the right hand side of (33). Here we proceed by fixing the time in the operator to the initial time t_0 and consider the operator $-\mathrm{div}(\mathbf{F}(t_0)\cdot)$. This, as any stationary Fokker–Planck operator, is expected to have a discrete spectrum [88,89] apart from special cases (like e.g. intermittency), the elements of which describe an exponential decay $P \sim \exp(-\lambda_{FP,i}(t_0)t)$. The largest eigenvalue $\lambda_{FP,1}(t_0)$ is expected to be 1, expressing that if the initial distribution corresponds to the natural measure, it would remain so forever. From the point of view of convergence, the *second largest* eigenvalue $\lambda_{FP,2}(t_0)$ is relevant, which governs a decay of the type $\exp(-\lambda_{FP,2}(t_0)t)$, and the notation indicates that the eigenvalue depends on the time of initialization. The reciprocal of the eigenvalue (of its real part if the eigenvalue is complex) sets a time scale, and we can write

$$P(\mathbf{x}, t, t_0) \quad \rightarrow \quad P^*(\mathbf{x}, t) \quad \text{for} \quad t - t_0 \gg \frac{1}{Re\ \lambda_{FP,2}(t_0)}. \tag{36}$$

The probability distribution thus *forgets* its initial form, and after the characteristic time set by the second eigenvalue the distribution evolves into $P^*(\mathbf{x}, t)$, i.e. the one characterizing the snapshot attractor or the chaotic sea (provided, there is a single such object present).[5]

The case of Hamiltonian problems is special, since because of the disappearance of the phase space contraction rate, a possible solution of (34) is a location- and time-independent P^*. Quantity $1/\lambda_{FP,2}(t_0)$ is then the time-scale after which an initially localized distribution approaches this constant density. Non-trivial examples of natural measures are thus expected in dissipative cases only, discussed in what follows.

The distribution $P^*(\mathbf{x}, t)$ is the analog of the celebrated SRB measure [75] for usual chaotic attractors. We are evaluating statistics over the ensemble, this is however the same as determining averages (e.g. the EAPD function or the information dimension) with respect to $P^*(\mathbf{x}, t)$, these averages are therefore time-dependent. We can thus say that even if chaos is unpredictable on the level of single time series, chaos is *fully predictable in a probabilistic sense even in drifting systems.* It is to be mentioned that the natural measure can also be reconstructed using response theory, see e.g., [90]. The only examples of natural measures on snapshot attractors that we know of have been given in low-dimensional climate-related models, see e.g. [91–93], as well as in an epidemics related model [31].

We note here that an important aspect of numerical simulations is the time after which the simulation can be thought to faithfully represent the natural measure of the snapshot attractor. An estimation of this convergence time, t_c, was given in Section 3.1 as the time for when the averages of all the phase space variables taken with respect to two initially different ensembles are practically identical. (A more strict definition might request the identity of other statistical quantifiers, too.) This t_c typically depends on the particular choice of initial conditions, but is certainly *on the order of the characteristic time set be the second eigenvalue* of the Fokker–Planck operator (which is independent of initial conditions):

$$t_c \sim \frac{1}{Re\ \lambda_{FP,2}(t_0)}. \tag{37}$$

[5] Note that the negative Lyapunov exponent λ' might be comparable in modulus with $\lambda_{FP,2}(t_0)$, it is, however, conceptually different as it does not say anything about the convergence of a distribution.

It is worth emphasizing that for a time instant t for which $t - t_0 < t_c$ an ensemble simulation might produce a distribution, but this is not yet the natural measure, and averages taken with respect to it are *not* characterizing the snapshot attractor at time t.

In a different vain, it is also worth thinking about what the shortest observational time interval should be in order to allow for the extraction of reliable dynamical information. As a straightforward tool, the convergence time discussed here can be used to find an answer, the first constraint being that t_{max} should be larger than t_c. In addition, we can also find another kind of convergence time in relation to foliations, concerning the auxiliary time k: for times longer than a threshold, the shape of the foliations does not change on large scales. The numerical value of this "auxiliary convergence time" turns out to be comparable with t_c in our examples. We note that there is a conceptually somewhat different convergence time characterizing the convergence to chaotic saddles and their distributions, too. It is a good approximation if we assume that t_c is roughly the same for all chaos-related phase space objects (and independent of t_0) and coincides with the auxiliary convergence time. This provides a lower bound on the length of the time window as

$$2t_c < t_{max}, \qquad 2t_c/T < n_{max}, \tag{38}$$

where the factor 2 comes from the need to provide a faithful foliation-based characterization of the dynamics, see Eq. (22). This relation also shows that a novelty of the constraint of finite observational time windows is that the convergence time (related to the second eigenvalue of the evolution operator) fits only a *limited number* of times on the full window.

For a non-autonomous two-dimensional stroboscopic map (3) taken with time unit T the process is the following. Let $P_n(\mathbf{x}, n_0)$ denote the density at discrete time n evolved from an initial distribution $P_0(\mathbf{x})$ prescribed at n_0. The integral of this density over a small area dA about point $\mathbf{x}$ is $P_n dA$, and can be called the "material content". The map brings the phase space point into $\mathbf{f}_n(\mathbf{x})$, and the area into a dA'. The new density $P_{n+1}(\mathbf{f}_n(\mathbf{x}), n_0)$ at the image of $\mathbf{x}$ follows from the invariance of the "material content": $P_{n+1}dA' = P_n dA$, from which

$$P_{n+1}(\mathbf{f}_n(\mathbf{x}), n_0) = \frac{P_n(\mathbf{x}, n_0)}{J_n(\mathbf{x})}, \tag{39}$$

where we have used that dA'/dA is the Jacobian J_n of the map at the original point at time n. This is the time-evolution equation for invertible non-autonomous maps, also called the *Frobenius–Perron* equation (see e.g. [72,82,86]). Here, again, one observes that the solution $P_n(\mathbf{x}, n_0)$ of (39) converges, after some time, to $P_n^*(\mathbf{x})$, the time-dependent natural density on the snapshot attractor. The Jacobian in (39) and the phase space contraction rate in (33) are related, e.g. for a constant phase space contraction $J = \exp(-\sigma T)$. In fact, by taking the limit $T \to 0$, one sees that (39) goes over into the two-dimensional version of (33), (34).

The ensemble simulations of snapshot attractors presented in this paper are in full harmony with the mathematical concepts applied above. We start typically with a uniform distribution of initial points in a phase space region, defining (after normalization) an initial distribution P_0. All the trajectories are followed in time, and the 'material content' corresponds here to the number of trajectories in a phase space volume. Since no new trajectories are initiated, their total number is constant over time, and those who are in a region once will remain in the image of that region later. Due to the dynamics and phase space contraction, the distribution does not remain constant, and when stopping the simulation at some time t, the distribution of the trajectory points at this time t defines (after normalization) a density $P(\mathbf{x}, t, t_0)$. This density is determined with the accuracy of the numerical simulation, which can be made – in principle – arbitrarily small. There is no sign of unpredictability when working with probabilities.

In practice, a simple two-dimensional histogramming of the points of the snapshot attractor in a given instant provides, up to the smallness of the bin sizes, an approximation of the distribution in that instant. In all examples throughout the

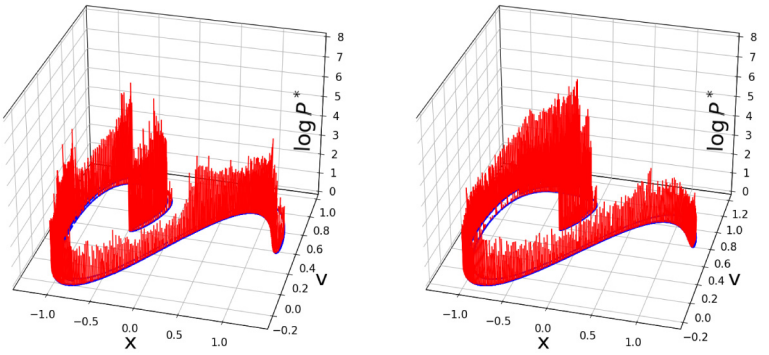

(a) (b)

Fig. 13. Natural measure (red) of the snapshot attractor of Fig. 6 belonging to time instances $n = 60$ (a) and $n = 100$ (b), with $N_{ext} = 40000$ (with the same initial ensemble used for plotting the attractor). The snapshot attractor, the support of the distribution, is plotted in blue.

paper, the number of bins is set to be on the order of $\sqrt{N_{ext}}$ in both x and v directions, where N_{ext} is the number of trajectories in the ensemble. This implies several hundred bins and an average column height of non-empty bins on the order of 100, which provides sufficient statistics for visual representations.

Fig. 13 exhibits the natural distribution obtained this way for the snapshot attractors shown in panels (b) and (c) of Fig. 6. One clearly sees that not only the support, the attractor, changes in time, but also the distribution. Differences can be observed nearly anywhere, a particularly striking feature is the rather dense appearance of the distribution at about $x = -0.5$, $v = 1$ in panel (b). In this region a new folded structure has appeared by time $n = 100$ in the pattern of the attractor (see Fig. 6(c)), and the vertical funnels of the density on this structure lead to the appearance of the new columnar pattern in panel (b) of Fig. 13. (Note that the unicolor representation of the density applied here does not allow for a clear distinction of individual columns lying behind each other.) Its is also clear that the distribution itself is fractal-like, and its information dimension is time-dependent (we are going to give an estimate of this later, see Section 7). More generally, any statistical characteristics evaluated with respect to the natural measure (like. e.g mean values, standard deviations) will be time-dependent. Concerning the view of parallel dynamical evolutions, Fig. 13 also illustrates that the different evolutions do not contribute with equal weights, and these weights depend on time.

3.5. Comparison with the frozen dynamics

In Section 2 we saw that snapshot points are different from their counterparts in the frozen systems. The difference between the two classes is even more pronounced in the context of chaos. In the dissipative case, the bifurcation diagram of the frozen system is shown in Fig. 14 for $\beta = 0.2$. The green and red lines mark the start and end of the scenario used in Fig. 6, while the blue line at $\varepsilon = 0.46$ indicates a periodic window with three fixed point attractors.

An example of the drastically different behavior of the drifting system is provided by Fig. 15 where we show the chaotic snapshot attractor at the value of the driving amplitude ε to which the three fixed point attractors belong in the frozen system, marked by the blue line in Fig. 14. *The snapshot attractor is extended and chaotic, while the attractors of the frozen system are periodic and point-like.* A closer observation (see inset) reveals that the attractor points (red dots) are not on the snapshot attractor (blue set of points). The snapshot attractor and its counterpart of the frozen system can be *distinct geometric sets*. The only connection between them is that some global features of the usual bifurcation diagram, the existence of a periodic window, can have influence on the drifting system, by weakening chaos in this region, which can only be observed on the EAPD function and the Lyapunov exponent, which we saw in Figs. 11(a) and 12.

Another interesting aspect is the fate of the analogs of the regular (red) points with increasing rates. We are not in the regime where the perturbative approach of Section 2 would apply. Therefore, we can only speculate if the counterparts of the red points in the presence of a drift are snapshot points. Attractive snapshot points are not likely to exist here since there is no sign of coexisting attractors in the simulation. It is the natural measure on the snapshot attractor which can provide a hint on the existence of these points as *unstable SHPs which are embedded into the chaotic snapshot attractor*. The natural measure of the snapshot attractor of Fig. 15 is plotted in Fig. 16(b). For comparison panels (a) and (c) correspond to an earlier time, $n = 10$, and a later time, $n = 30$, respectively. In panel (b) three *narrow peaks* have appeared in the distribution at locations close to those of the red points in Fig. 15, marked here by black vertical dashed lines. The fact that these are somewhat off the peaks is natural since the frozen cycle points are not on the snapshot attractor as illustrated by Fig. 15. Furthermore, snapshot points in drifting systems always differ from the frozen ones (now even more than in the perturbation expansion of Section 2). The fact that the mentioned peaks are somewhat larger than any other peaks, suggests that the underlying hyperbolic points are *weakly* unstable, and can thus be traces of the red points being converted into SHP-s by the drift.

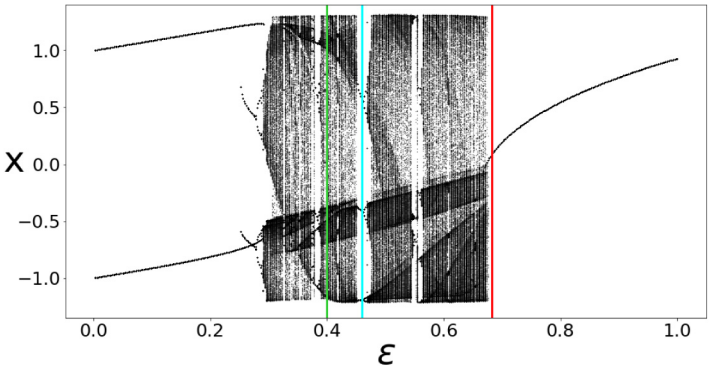

Fig. 14. Traditional bifurcation diagram of the stroboscopic map of (4) with a time-independent driving amplitude ε and damping constant $\beta = 0.2$. Transients of length 200 time units are discarded. The green, light blue and red lines mark characteristic values of the driving amplitudes along the scenario of Fig. 6 of $\varepsilon = \varepsilon_0 = 0.4$, $\varepsilon = \varepsilon_{21} \approx 0.46$ and $\varepsilon = \varepsilon_{100} = 0.682$, respectively.

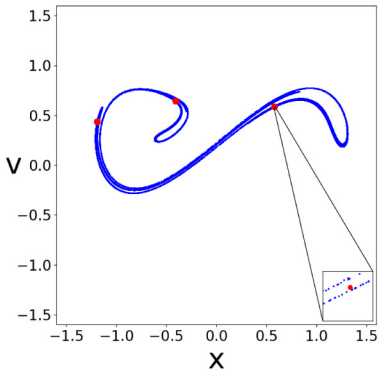

Fig. 15. Comparison of attractors. The snapshot attractor of Fig. 6 ($n = 21$, $\varepsilon_{21} = 0.459$) is plotted along with the three fixed point attractors (red points) of the frozen system existing at the *same* value of ε (see the blue line in the periodic window of Fig. 14). The inset is a blow-up of the neighborhood of the rightmost red point.

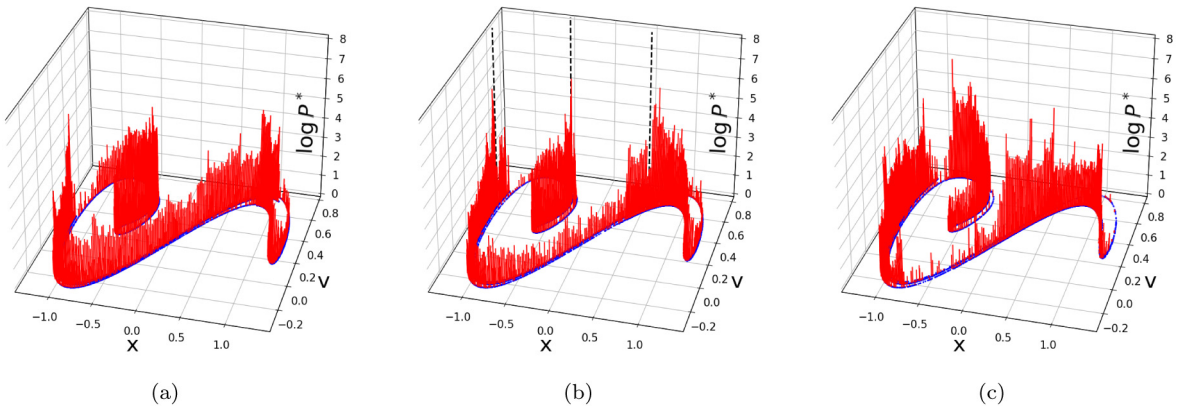

Fig. 16. Natural measure on the snapshot attractor of Fig. 15 belonging to a periodic window of the frozen system, at instant $n = 21$, $\varepsilon_{21} = 0.459$, displayed in panel (b). Black vertical lines show the location of the three attractor points in the frozen system, marked as red dots in Fig. 15. Panels (a) and (c) display the natural measures at earlier and later times, at $n = 10$, $\varepsilon_{10} = 0.428$ in (a) and $n = 30$, $\varepsilon_{30} = 0.484$ in (c).

The appearance is similar to that of noise induced chaos in the framework of which periodic attractors of a deterministic system become embedded into a noise-induced chaotic attractor when the noise strength increases beyond a threshold (yet remaining weak). The distribution of the natural measure on the snapshot attractor of noise-induced chaos has then large peaks about the original fixed point attractors, indicating that the attractor points are converted into weakly unstable points due to noise as demonstrated in [94,95]. What we see in Fig. 16(b) is very similar to this, thus the phenomenon can be called *drift induced chaos*. Earlier and later, these peaks do not exist, while other peaks of similar height might appear at other locations, see Fig. 16(a) and (c), respectively.

Regarding Hamiltonian systems, in Fig. 17(a) the snapshot torus appearing in Fig. 7(b) at $n = 40$ (blue) is shown to not coincide with any tori in the frozen system of the corresponding $\varepsilon_{40} = 0.205$ value. Some tori from the frozen island at the corresponding amplitude $\varepsilon = 0.205$ are plotted in red. One of these tori was initiated from the leftmost point of the snapshot torus, meaning that they have at least one common point. A magnification reveals (see inset), that this torus is clearly different from the snapshot torus, meaning that all the others have to be different as well. Thus *the snapshot torus does not coincide with any of the frozen tori*, not even with ones tangent to it. Of course, the difference would be even more pronounced if an already broken-up snapshot torus was compared to frozen tori.

We can also look at chaotic seas, as shown in Fig. 17(b). In blue we see the snapshot chaotic sea in the same scenario and time instant ($n = 40$) as that of Fig. 17(a), i.e. the same snapshot chaotic sea as in Fig. 8(a). Underneath it the frozen chaotic sea belonging to the corresponding ε value is shown in red, and we can observe that the frozen one is of larger extension than the snapshot chaotic sea, as the latter does not cover the former fully. In fact, the differences between the two sets can be observed around the edges of the outermost snapshot tori (not shown).

In Section 2.1 we have briefly mentioned rate induced tippings [58,66–70] in relation to snapshot points. Qualitatively, this phenomenon implies that the behavior in the drifting system becomes completely different from the frozen one. In the context of chaos, frozen and snapshot attractors can only be similar with a very slow rate of the parameter drift. This means that in processes with increasing rates α, the system should go through a kind of rate induced tipping,

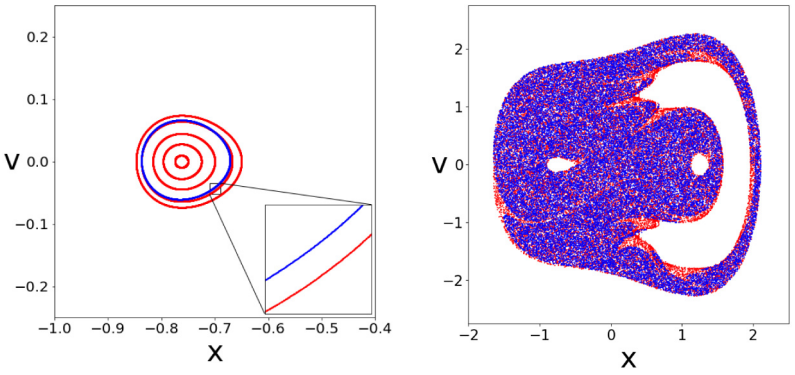

Fig. 17. (a) Comparison of tori: blue snapshot torus in Fig. 7(b), $n = 40$, $\varepsilon_{40} = 0.205$, and tori of the frozen system (red) belonging to the *same* ε value generated from initial conditions $x_0 = -0.65, -0.7, -0.725, -0.75$, $v_0 = 0$, as well as one generated from the leftmost point of the blue snapshot torus. The inset is a blow-up showing parts of the snapshot torus and the frozen torus touching it on the left. (b) Comparison of chaotic seas. Blue points indicate the snapshot chaotic sea in the phase space of the blue snapshot torus in panel (a), while the frozen chaotic sea, shown in red, belongs to the phase space at $\varepsilon = 0.205$, lying outside the red frozen tori in panel (a). Both sets consist of $N_{cha} = 30000$ points.

a tipping from periodic into chaotic behavior, the result of which is illustrated by Fig. 15. An analogous process in Hamiltonian systems is the tipping from quasi-periodic to chaotic behavior in relation to the evolution of snapshot tori with increasing α. The case of snapshot tori not breaking up during a finite time interval is illustrated in Fig. 17(a), while the break-up process of a torus is shown in Fig. 7. To our knowledge, such tippings have not yet been investigated in the rate-induced-tipping literature.

At the end of this section, we are reformulating some of the observations made here considering the question of adiabaticity. Fig. 15 clearly illustrates that tracking of the frozen attractors is not ensured by the existence of the extended snapshot attractor in the drifting process. The process is thus *non-adiabatic* from the point of view of attractors. The Hamiltonian case depicted in Fig. 17 shows that tracking is valid up to $n = 40$ for both objects shown. Concerning the snapshot torus, even though it clearly deviates from the frozen one, this deviation is small, while for the chaotic seas, though there are notable differences between the two, these are somewhat small in area compared to the whole of any of the sets. Therefore, if we were to observe the process up to $n_{max} = 40$ only, the corresponding parameter would be $R' = 1.6$ (allowing for non-adiabaticity), but the process would be adiabatic for both the snapshot torus and the chaotic sea. Fig. 7 illustrated that with $n_{max} = 100$, tracking is broken for the torus by $n = 52$, and then the process is *non-adiabatic* for the torus, in harmony with $R' = 4$ being large.

Here we gave a short summary of the question of adiabaticity in both dissipative and Hamiltonian systems, and additional comments will be given concerning dissipative cases in what follows (Sections 4 and 5). We note that most generally speaking, any process in which rate-induced tipping is present for a phase space object is non-adiabatic for that object, if followed with a rate higher than the tipping threshold.

4. The relationship between snapshot chaotic saddles, manifolds and foliations

4.1. Generating saddles and manifolds with the sprinkler method

The theory of transient chaos is a well-established field of nonlinear science (for a monograph see [37]). The traditional subject of this field is chaotic behavior existing over a finite time. The central objects in the phase space are *non-attracting chaotic sets*, typically a fractal set of zero volume on which the dynamics is chaotic, but from whose neighborhood an escape occurs. In invertible systems these sets are *chaotic saddles*, the elements of which are saddle-point-like. The full set is not globally repelling, but possesses *stable manifold*, the set along which the saddle can be reached, which is of zero volume (and therefore cannot be called a basin of attraction in the classical sense). The analog set in the time reversed dynamics is the *unstable manifold*. A quantity specific for transient chaos is the rate of the emptying of any region surrounding the chaotic saddle, called the *escape rate*. The reciprocal of it can be used for estimating the lifetime of chaos for points originally close to the saddle.

As a traditional case, we consider a periodic window (a typical occurrence of transient chaos), marked by the light blue line of Fig. 14 at $\varepsilon = 0.46$. A straightforward and easily applicable method for the construction of a chaotic saddle is the *sprinkler method* (see e.g. [37,96]). This is based on distributing a large number of points in a pre-selected region. Trajectories starting from each point are followed and only those are kept which *remain* in the pre-selected region up to $2n + 1$ time units, starting at time $-n$ and ending at n. The number of surviving points up to time n is denoted by N_n. The length of the time interval $2n + 1$ should be a few times $1/\kappa$ to ensure that the majority of the original trajectories

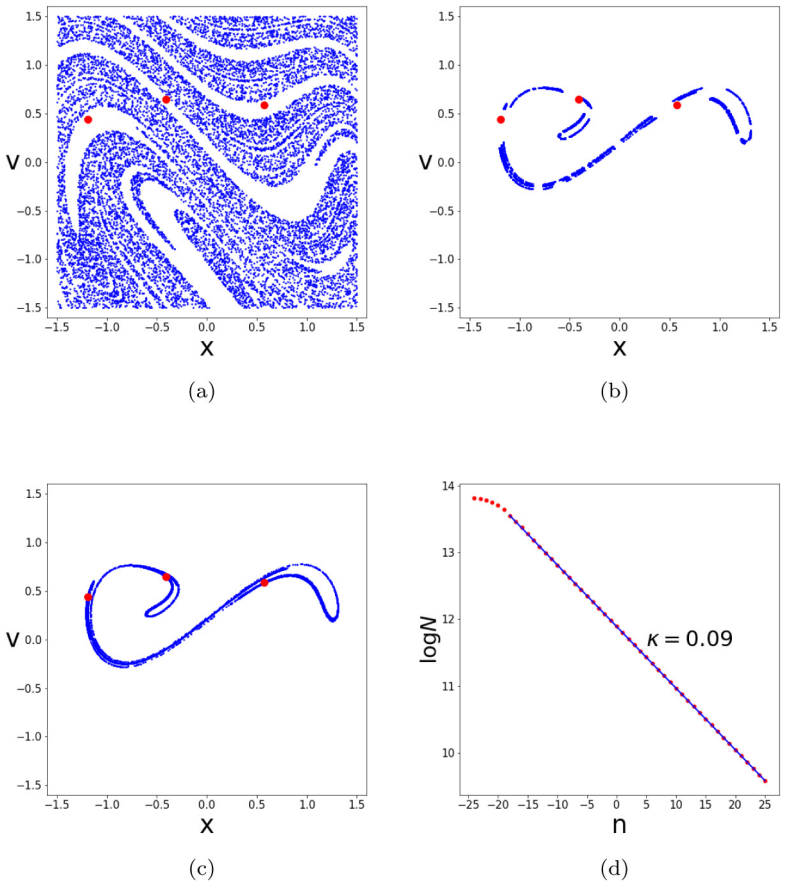

Fig. 18. Characteristic sets of a time-independent chaotic saddle with $\varepsilon = 0.46$, $\beta = 0.2$. The number of initial points, distributed on a square between $-1.5, 1.5$ in both directions, is $N_{ext} = 10^6$. (a) Stable manifold (b) chaotic saddle, (c) unstable manifold, obtained as the points of the non-escaped trajectories at $n = -25$, $n = 0$, and $n = 25$, respectively, excluding three small disks around the attractor points, shown in red. Panel (d): number N_n of non-escaped points as a function of time n (red) and the fitted straight line (blue).

has escaped the region by the end of the simulation. The kept trajectories are thus long lived, which can only happen if they started very close to the stable manifold of the saddle, and visited later points of the saddle with good accuracy. Therefore, by plotting the initial and endpoints of the kept trajectories one gets approximants to the stable and unstable manifold, respectively, while the midpoints of all the kept trajectories approximate the chaotic saddle itself within the pre-selected region. Under ideal conditions this region should be chosen to fully contain the chaotic saddle.

Fig. 18 provides an example of this algorithm. In the shown range of the phase space 10^6 points are initially distributed uniformly, and followed up to 51 periods. Only a portion of the initial points remains all the time in the region. The initial point of such non-escaped trajectories, at discrete time $n = -25$, are visible in panel (a). This fractal set of points leads initial points to the saddle, thus it corresponds to the stable manifold of the saddle. The saddle itself is visible in panel (b), consisting of points taken at time $n = 0$. Such a set is typically a double fractal. The unstable manifold is traced out by the last points ($n = 25$) of the trajectories (panel c), and corresponds to an object which directs points from the saddle to the attractor points of three fixed points, shown in red in panels (a-c). In panel (d) the number N_n of nonescaped trajectories is shown as a function of time, on a semi-logarithmic scale. The fitted value of the escape rate is $\kappa = 0.09$, the investigated time interval of 51 periods is thus about five times of the average lifetime of chaos.

Note that the unstable manifold in panel (c) contains the three (red) attractor points since an unstable manifold can only direct points into attractors. A comparison with Fig. 15 displaying the snapshot attractor belonging practically to the same driving amplitude enables us to complete the discussion at the end of the previous section on adiabaticity. The extended structure in these panels is nearly indistinguishable, although their dynamical role is very different: the extended structure of Fig. 15 is an attracting chaotic object and does *not* contain the red points, while Fig. 18(c) represents the unstable manifold of a chaotic saddle that incorporates the red points. Based, however, on our earlier observation according to which the snapshot attractor is an unstable foliation, we are comparing here the unstable foliations of the drifting and of the frozen system, and find that the difference is minor, tracking is fulfilled. We thus discover a dichotomy

in adiabaticity: the dissipative process studied in the scenario of Fig. 6 is *non-adiabatic for attractors, but adiabatic for unstable foliations*.

The features illustrated by Fig. 18 show up in systems subjected to parameter drift as well, see e.g. [37–39]. The main new point here is that the saddle changes with time (unlike in Fig. 18, where taking a larger n would only yield sets with less points but of the same shape), and therefore the sprinkler method provides sets belonging to *different* time instants. The algorithm applied for drifting systems thus depends on which of the characteristic sets is to be determined. Being interested in the chaotic saddle at time instant n, one should initiate trajectories at time $n - k_s$ (where k_s, the auxiliary time used for the sprinkler method, should be sufficiently large) and follow the non-escaping trajectories up to time $n+k_s$. The midpoints of these trajectories approximate the chaotic saddle at time n. This now changes with time n and should be called the *snapshot chaotic saddle*. The initial and end points of the non-escaped trajectories correspond to stable and unstable manifolds here, as well, just the former is now the snapshot stable manifold at time $n - k_s$, while the latter the snapshot unstable manifold at time $n + k_s$. This shift in time between the saddle and the manifolds generated this way results in the feature that these manifolds do not belong to the saddle at time n. It follows then, that if the stable (unstable) manifold is to be obtained at time n, then, using the framework of the sprinkler method with a given k_s, it arises as the initial (end) point of non-escaped trajectories in an algorithm aiming at generating the saddle at time $n + k_s$ ($n - k_s$). The manifolds obtained this way are the manifolds of the saddle at time n, and intersect each other in the snapshot chaotic saddle, as discussed earlier e.g. in [37,38].

4.2. Dissipative systems

Let us apply this method to the scenario of Fig. 6. Fig. 19 summarizes the results for the saddle at time $n = 60$ (the same instant as in Fig. 6(b)). Panel (a) shows the range in which trajectories are initiated at time $n - k_s = 20$, and the blue points belong to non-escaping orbits. They shade the full square, illustrating that no escape occurs, the stable manifold

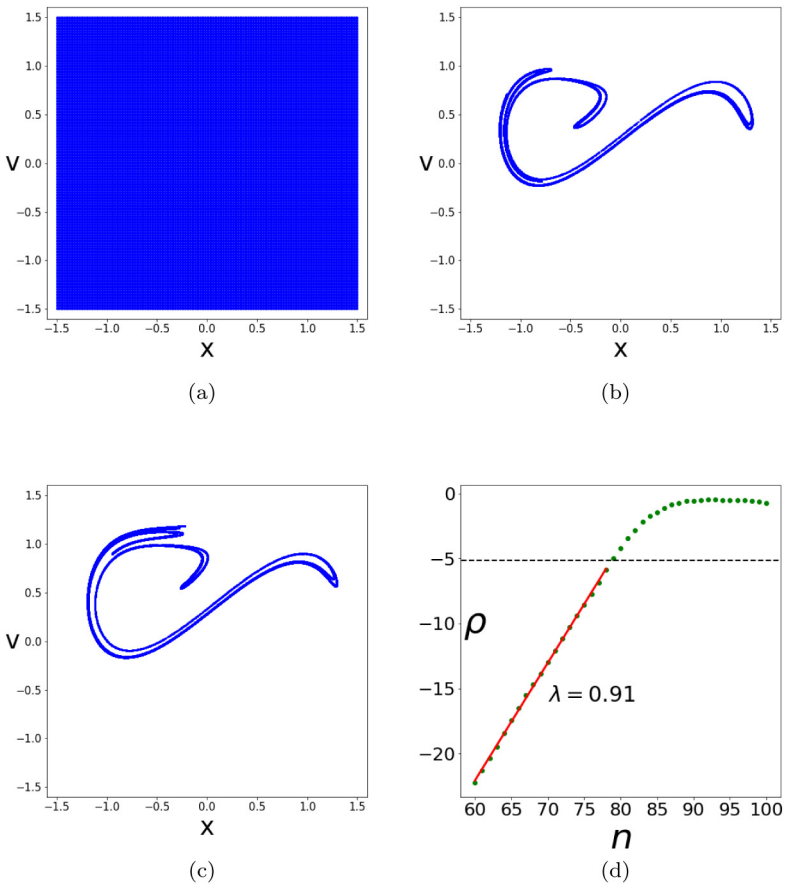

Fig. 19. Chaotic snapshot attractors as snapshot saddles. Here the sprinkler method for $n = 60$ was applied with $k_s = 40$, $N_{ext} = 90000$, in the scenario $\varepsilon_0 = 0.4$, $\alpha = 0.00045$, $n_{max} = 100$ and $\beta = 0.2$, resulting in characteristic sets (a) stable manifold, (b) saddle, (c) unstable manifold. The formal snapshot chaotic saddle in panel (b) is identical to the snapshot attractor at this time instant (Fig. 6). Panel (d) shows the EAPD curve initiated on this set.

is not a fractal, in fact it is the full phase space. This is, however, natural in view of the fact that the snapshot attractor is the only attracting set. Panel (b) shows the trajectories at time $n = 60$. Formally this is the chaotic saddle at this time, but it is not a double fractal, we see here a *degenerate* case. In fact, the saddle fully corresponds to the snapshot attractor of Fig. 6(b). We can thus conclude that a snapshot attractor can actually be considered a special snapshot saddle, when no other attractors are present. The last panel (c) is the end point of the investigated trajectories, the unstable manifold at time $n + k_s = 100$. This is nothing but the snapshot attractor at time $n = 100$ shown in Fig. 6(c).

These observations can be interpreted from the point of view of foliations, as well. It is important to add that Figs. 19(a) and 19(b) would be similar for later instances up to at least $n = 100$. A particular consequence of this is that the stable manifold would fill the region even at $n = 60$. Because of this, it should correspond to the stable foliation at this time, which is space filling because of the lack of any other attractors. The manifold in this case provides a more faithful view than Fig. 9(b), obtained via a direct generation of the stable foliation, in which the complete space-filling property is not yet fully evident. The unstable foliation was shown to coincide with the snapshot attractor in Section 3.2. Panel (b) of Fig. 19 shows thus nothing but the unstable foliation at $n = 60$. Thus any point of panel (b) is an intersection point of the two foliations, but since panel (b) is simultaneously the snapshot attractor, we conclude that *any point of the snapshot attractor is chaotic*, also supported by panel (d), indicating the positivity of the Lyapunov exponent. It can thus indeed be called chaotic snapshot attractor. In Section 5.1 we shall see that not all snapshot attractors are of this type.

These arguments, based on the view of transient chaos, deepen the observation formulated above according to which the snapshot attractor is the unstable foliation (see Figs. 6 and 9), which appears here as the unstable manifold of a (dense) snapshot saddle. Furthermore, based on this result, we can also say that for this type of snapshot attractor *the unstable manifold of a chaotic saddle coincides with the unstable foliation* belonging to the same time instant. Similarly, we can say that *the stable manifold of a chaotic saddle coincides with the stable foliation*. From the point of view of the convergence to the snapshot attractor, Fig. 19 shows the evolution of an initially broadly extended ensemble, in contrast to the localized ensemble of the plume diagram in Fig. 6(a), both converging to the same attractor.

4.3. Hamiltonian systems

Transient chaos is a useful tool for looking into the details of the dynamics of chaotic systems, by selecting a region within an interesting chaotic part of the phase space, and determining the points never escaping this region. The method is called *leaking* the dynamical system [97].

We apply this approach to find a relation to snapshot chaotic seas. We select a region, a square centered on the point (0.25,0) and determine the chaotic saddle within it in Fig. 20 in the course of the scenario of Fig. 7, at instant $n = 35$. The saddle (panel b) turns out to be rather sparse and unstable, therefore, a short interval $k_s = 2$ should be taken for its determination using the sprinkler method. Panels (a) and (c) display the stable and unstable manifold at times $n = 33$ and 37, respectively.

Fig. 21 provides a more global view. Panel (a) shows the stable and unstable foliations of Fig. 10 superimposed, as well as some surviving snapshot tori. The difference between the two foliations was mentioned in Section 3.2. From a dynamical point of view, the most basic components of chaos are Smale horseshoes, or the intersections between the two foliations. We shall call the set of intersections, that is the embedded chaotic saddle, the *chaotic subset* of the chaotic sea. In contrast to traditional chaos, this set proves to be *smaller* than any of the foliations. Panel (b) displays the same foliations, but it also contains two insets, out of which the one in the lower right corner is of interest for now (we will come back to the other one in Section 6.2). Here, the light blue points are identical with those of the chaotic saddle in Fig. 20(b). It is

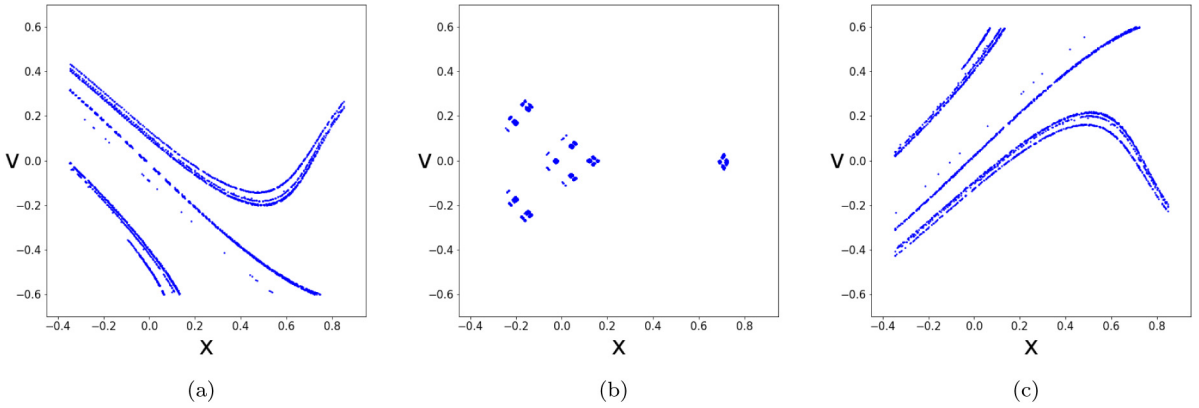

Fig. 20. Transient chaos within the snapshot chaotic sea in the scenario of Fig. 7. Panels (a)–(c) show the snapshot objects: stable manifold, the saddle, and the unstable manifold, respectively, obtained by using parameters $n = 35$, $k_s = 2$ and $N_{ext} = 10^6$ initial points distributed (at $n = 33$) uniformly on the square shown.

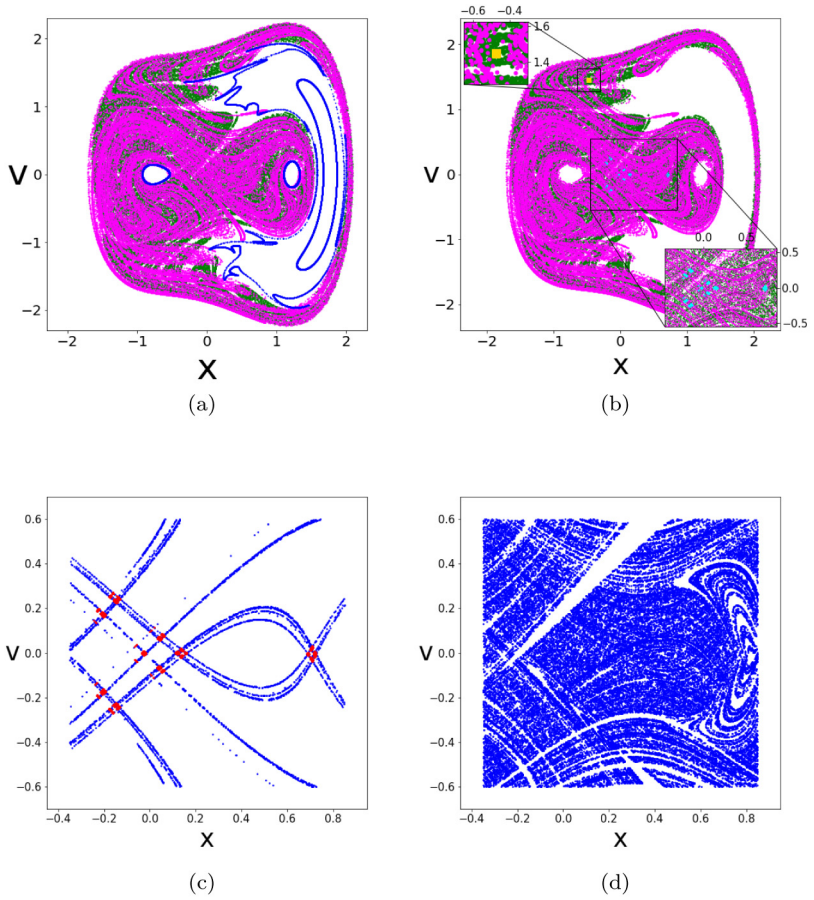

Fig. 21. Foliations and saddles in a Hamiltonian case. (a) Foliations of Fig. 10 overlaid. Initial conditions for the tori are $x_0 = -0.75, 0.96, 1.561, 1.65$, $v_0 = 0$. (b) The same without tori. The lower right inset shows, inside a square of edge length 1.2 centered at point (0.25, 0), points of the chaotic saddle of Fig. 20(b) in light blue. Upper left inset: a yellow square of edge length 0.04 centered at point $(-0.475, 1.45)$ magnified. (c) The snapshot chaotic saddle (red points) of Fig. 20(b) at time $n = 35$ along with the stable and unstable manifold belonging to the same instant, $k_s = 2$. (d) A saddle type object belonging to $n = 35$, generated with $k_s = 10$, and $N_{ext} = 2.25 \cdot 10^6$ initial points at $n = 25$, following the constraint that the trajectories are in the investigated region only at instants $n_{eval} = 25, 35, 45$.

satisfying to see that these *coincide with intersection points of the foliations*. The chaotic subset thus contains the snapshot chaotic saddle. The chaotic subset is of course much larger since the saddle is formed by never escaping points of the region shown in Fig. 20, which are rare.

Panel (c) displays the same saddle as Fig. 20(b) but plotted together with the stable and unstable manifolds belonging to the *same* time instant $n = 35$. By keeping parameter $k_s = 2$, these manifolds are emanated, in the framework of the sprinkler method, from the chaotic saddles of time $n = 37$ and $n = 33$, respectively, as described earlier. One clearly sees that the manifolds intersect each other in the points of the saddle. (This would not be the case with the manifolds shown in Fig. 20, which cannot be overlaid since they belong to different time instants.) This property is consistent with the observation that the chaotic subset of the chaotic sea is the intersection of the stable and unstable foliations belonging to the same time instant.

Panel (d) opens up a new view. Points of it are obtained by following the algorithm of the sprinkler method for a saddle at $n = 35$ by using $k_s = 10$, but trajectories escaped earlier than $n = 45$ are not excluded, and their presence in the investigated region is prescribed at certain times only, in this case at $n = 25$, 35 and 45. A saddle-like object is obtained with much more points than the traditional saddle. This offers a broader interpretation of the snapshot chaotic saddle, and it also comes with the advantage that the points of this new saddle are also part of the chaotic subset, providing a better approximation of it. A method of selecting trajectories which follow a given set of constraints in time was explored and called "leaking in history space" in [39], and led to a double fractal set at the midpoint, just like with the constraint of never escaping a region (i.e. the traditional sprinkler method). The case of panel (d) corresponds to this method by applying a constraint in certain instances only, and the regime being the same.

5. Advanced features in dissipative systems

To help us in the discussion of features in dissipative systems, it is beneficial to define two distinct regimes. In the examples treated up to now, if exists, time-dependent chaos is robust, with a chaotic snapshot attractor and a degenerate saddle that coincides with the attractor. This we call the *robust regime*. The other regime, that we shall present in this section, is characterized by the novel feature of weak time-dependent chaos, which is governed by a non-degenerate time-dependent chaotic saddle, and the resulting attractor is called a *strange snapshot attractor* [46]. We shall call this regime the *weak regime*. The limit of weak driving, treated in Section 2 in order to make perturbative results for snapshot points possible, is a subset of this regime. The two regimes in our system can be roughly distinguished by the typical values of parameters ε and β as well; typically where chaos is present in the robust regime, e.g. the case of Fig. 6, both are on the order of a few tenths, while in the weak regime β is typically smaller by 5–10 times. The transition between the two regimes based on these parameters will be investigated in Section 5.6.

5.1. The strange snapshot attractor

A quite peculiar feature of the weak regime is that a fractal-looking snapshot attractor is not necessarily fully chaotic. Then a chaotic component *coexists* with simple snapshot attractors, in such a way that chaos is of *finite* lifetime. The weak regime of (4) is well suited for illustrating this in parameter ranges where *no chaotic attractors exist* in the drift-free system.

This is reflected by the bifurcation diagram of Fig. 22 with weak dissipation $\beta = 0.01$, where narrower black bands correspond to simple fixed points. The construction of the diagram differs from that of its traditional counterparts in the sense that relatively short transients (of length 50 periods) are discarded here before plotting the x values. The striking broad gray bands indicate that the dynamics is chaotic before reaching the simple attractors. It has been shown in earlier papers (see e.g. [38,45]) that it is transient chaos in the drift-free system that enables the existence of snapshot attractors in the presence of parameter drift: the unstable manifold of the frozen chaotic saddles is deformed into a time-dependent attracting object.

In Fig. 23, panel (a) shows a snapshot attractor in the weak regime in the scenario $\varepsilon_0 = 0.08$, $\alpha = 0.0005$, $n_{max} = 100$ ($R = 0.04$, $R' = 4$, the scenario is the same as in the Hamiltonian case of Fig. 7), after $n = 25$ time units, where $\varepsilon_{25} = 0.158$. In the full range three simple point-like attractors, SNPs are present. Two of these lie close to the origin, and can be identified in a perturbative approach, as carried out in Section 2 and the Appendix, and happen to be close to ± 1, the minima of the double well potential (Fig. 1(a)) characterizing the external force in (4). The third one at $n = 25$ is located at $(1.6372, 0.8291)$, and its estimated position for a given n can only be determined numerically. This is carried out iteratively by a successive approximation approach: we estimate the location of the attractor point for a given ε_n by an initial guess, initiate trajectories at $n = 0$ around this point, then take their average position at n as the new guess, and repeat the process until convergence is reached. It is worth mentioning that the SHP determined in Section 2 is found to lie on the snapshot attractor, as expected. The drastic difference between the frozen and the snapshot attractors implies a break-down of tracking along the entire scenario, the process is thus *non-adiabatic* for attractors in the weak regime.

The existence of SNPs is the reason for the appearance of the dense blue regions in panel (a). The initiation of the ensemble occurs on an extended region of the phase space, covering all SNPs. Some of the points become immediately attracted to the SNPs. Other parts of the ensemble become stretched and folded leading to a fractal-like pattern in regions further away. The snapshot attractor thus contains all SNPs, their compact surroundings, and a fractal-like component, too.

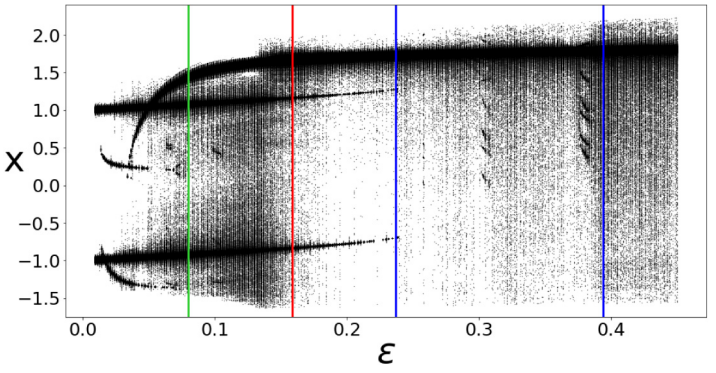

Fig. 22. Bifurcation diagram of (4) with a time-independent driving amplitude ε in the weak regime with $\beta = 0.01$ ($\omega = 1$), obtained by not excluding transients longer than 50 periods. The green line at $\varepsilon = \varepsilon_0 = 0.08$ marks the initial value of the driving amplitude in the scenario taken in Fig. 23, while the red line corresponds to $\varepsilon = \varepsilon_{25} = 0.158$, belonging to the attractor of Fig. 23(a). The blue lines mark the amplitudes $\varepsilon = \varepsilon_{50} = 0.237$ and the maximal $\varepsilon = \varepsilon_{100} = 0.394$ in the same scenario, at the end of the EAPD curves of Figs. 24(a) and 25(a), respectively.

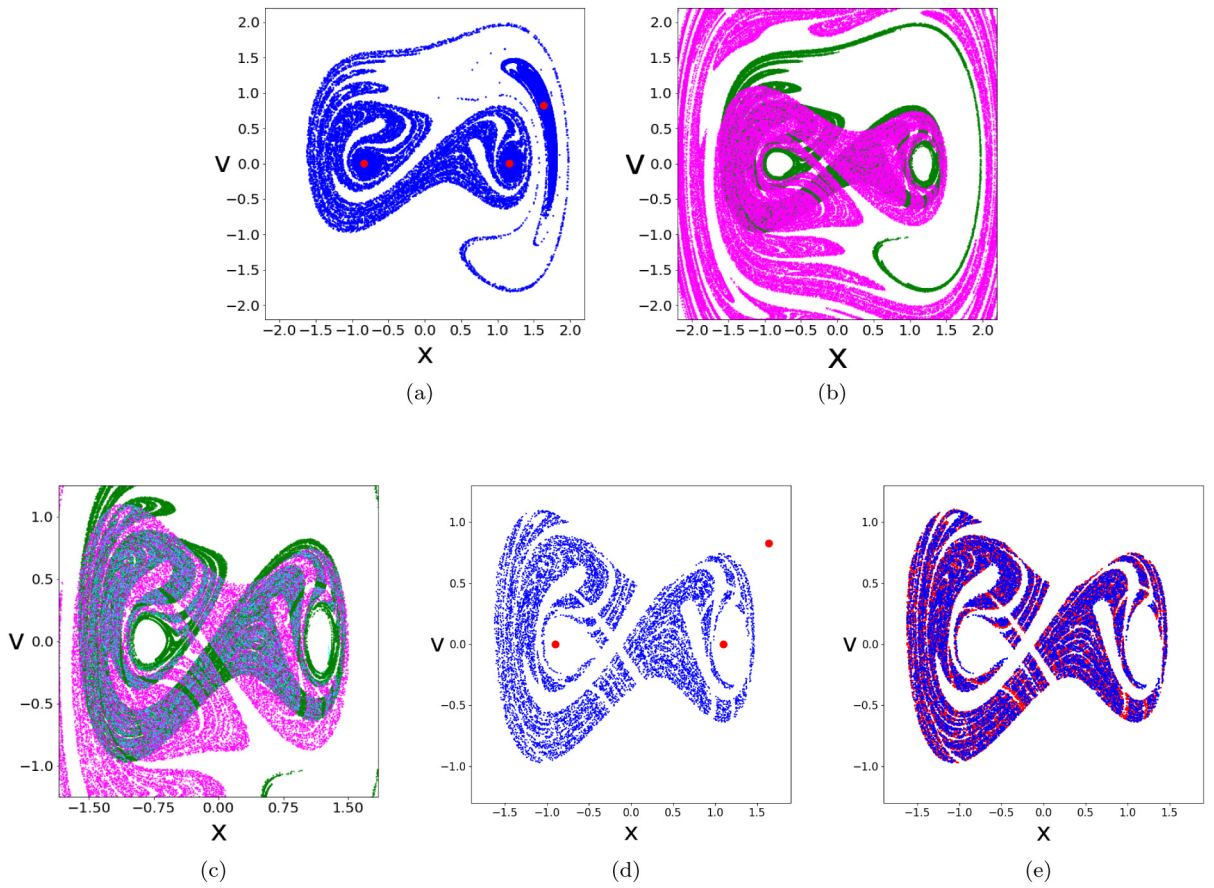

Fig. 23. (a) Strange snapshot attractor in the scenario $\varepsilon_0 = 0.08$, $\alpha = 0.0005$, $n_{max} = 100$, with $\beta = 0.01$, at time $n = 25$ ($\varepsilon_{25} = 0.159$) starting with $N_{ext} = 40000$ points on a square of side length 4 centered on the origin. (b) Unstable (green) and stable (pink) foliations generated for the instant $n = 25$ with $k = 10$ by initiating $N_{fol} = 50000$ points on 3 vertical sections of length $dl = 0.2$ around points $(-1, 0.8)$, $(0.25, 0)$, $(0.85, -0.5)$. (c) Blow-up of the previous panel around the intersection points. The cyan points show the chaotic saddle in good agreement with the intersection points of the foliations. The saddle was generated by the sprinkler method from $N_{ext} = 90000$ points on a rectangle of size 3.6×2.4 centered on the origin (note that the rightmost SNP is inside this rectangle), with $k_s = 20$. Escape towards the SNPs was studied by eliminating points that end up within a 0.1 radius of them. (d) The chaotic saddle obtained with $N_{ext} = 250000$ is shown separately, together with the SNPs (red dots). (e) The saddle of panel (d), shown in blue, compared with the chaotic saddle of the frozen case (red) corresponding to the driving amplitude of instant $n = 25$, $\varepsilon_{25} = 0.158$. Since both colors are visible, the two sets are not the same.

Such strange snapshot attractors do exhibit chaotic features, as the next panel illustrates, but chaos is not permanent, and hence it is useful to distinguish such cases from cases like those in Fig. 6, where a single permanently chaotic snapshot attractor exists. We note that the shape one sees in a particular simulation might depend on the choice of the region of initialization, and on the number of trajectories followed. If the region is far from the simple attractors and the scenario is not too long, the SNPs might be seen to be outside the snapshot attractor (see [46]). Furthermore, chaos being not permanent means that at the end of a very long scenario most of the points would be around the SNPs, connected with a sparsely populated filamentary pattern (as shown in [45] for a scenario with decreasing driving, and a similar case will be discussed in Fig. 26(d)).

In panel (b) the snapshot stable and unstable foliations at $n = 25$ obtained using auxiliary time $k = 10$ (past what we called "auxiliary convergence time" in Section 3.4) can be seen on top of each other. It is clear that the set of intersection points, the Smale horseshoe, is much smaller than the snapshot attractor visible in panel (a). The chaotic saddle is thus *not* populating the attractor, another reason to not to call it chaotic snapshot attractor. The term attractor is, however, properly used, since the blue object in panel (a) is an attracting set in the phase space, with a convergence time t_c of 8 periods.

The dynamics of this attractor is governed by transient chaos. To illustrate its snapshot chaotic saddle, panel (c) shows a blow-up image of panel (b), where cyan points indicate the chaotic saddle of this instant. The saddle is generated using the sprinkler method by discarding points that fell into a circle of radius 0.1 around the SNPs. It is clear from the image that the chaotic saddle obtained this way lies on the intersection points of the two foliations, the chaotic set of the problem

is thus an extended snapshot chaotic saddle (but not populating the full snapshot attractor). In panel (d) we highlight the saddle by showing it separately and with more points, as well as plotting the SNPs.

Transient chaos is present in the frozen dynamics as well, see Fig. 22, governed by a chaotic saddle. It is therefore natural to compare this frozen saddle to the snapshot saddle of panel (d). Panel (e) illustrates this comparison, with the snapshot saddle colored blue and the frozen one colored red. The latter belongs to the driving amplitude $\varepsilon = 0.158$, which is the same value as that of ε_{25} in the time-dependent scenario. While the shapes of the two sets are not very different, some red regions (e.g. around $(-0.25, -0.5)$) are visible, meaning that the sets are clearly not exactly the same either, again illustrating the observable difference between the drifting and frozen dynamics. Of course, the most significant difference is on the level of attractors, where the frozen ones are completely regular in the full ε range investigated. A similar property within a narrow periodic window of the frozen system was discussed in Section 3.5 in the robust regime. Here we complete this picture by showing that differences can be seen even at the level of chaotic saddles. The deviation is expected to depend on the specific system and scenario, for example, a much more pronounced difference was found in [38], when comparing the unstable manifold of the frozen chaotic saddle and the (strange) snapshot attractor itself. In the case of [38] parameter R can be estimated to be $R = 0.3$, and its value being close to unity suggests overall non-adiabaticity. In our examples with a much smaller value of R we conclude that processes in the weak regime are *non-adiabatic for attractors, but adiabatic for chaotic saddles*.

Finally, let us discuss the role of the foliations in relation to the strange snapshot attractor. The unstable one (green curve) is localized, exhibiting a fractal-looking structure. Note, however, the spiraling tendency appearing in the holes about the SNPs at $(\pm 1, 0)$. The length of the simulation ($k = 10$) is not long enough here to see that the foliation is approaching any of the SNPs, but we expect them to do so for larger k-s taken (up to k_{max}). On general grounds, the unstable foliation is expected to asymptotically reach the SNPs. Thus, *the unstable foliation is the same as the strange snapshot attractor*. The latter can be considered as the union of its two basic components: the chaotic saddle and the SNPs, along with the unstable foliation connecting them, and this statement is expected to hold throughout the scenario. It also follows then that *the unstable foliation coincides with the unstable manifold of the snapshot chaotic saddle* belonging to the same time instant. Concerning the stable foliation (pink curve), based on the observation that the chaotic set is a chaotic saddle, we can say that *the stable foliation coincides with the stable manifold of the snapshot chaotic saddle*. These statements are extensions of those mentioned at the end of Section 4.2.

5.2. EAPD of strange nonchaotic attractors and the disappearance of SNPs

When plotting the EAPD function of the strange snapshot attractor (Fig. 24(a)), we see that the distance growth is exponential at first, but then it stops, with a maximum at around $n = 30$, after which the average distance starts to slowly decrease. This can be interpreted as another manifestation of transient chaos: initially the chaotic motion around the saddle dominates, while later attraction towards the SNPs takes over. Note that the average distance remains orders of magnitude smaller than the extension of the phase space, meaning that the Lyapunov exponent can be evaluated throughout the whole range shown, which is why the cutoff line is absent from the image. Since the Lyapunov exponent is defined as the derivative of the EAPD function, *the value of the Lyapunov exponent reaches zero* at the maximum, and becomes negative when overall convergence towards the SNPs takes over.

Fig. 24(b) shows the shape of the attractor for $n = 30$ (at the maximum). It is similar to the one in Fig. 23(a), but now $\lambda = 0$, it is thus an *extended, fractal-like but non-chaotic attracting set*. We see here appearing the snapshot version of a *strange nonchaotic attractor*, an object intensively studied in the traditional chaos literature, see e.g. [98,99]. The EAPD curve suggests that the attractor remains non-chaotic for a while after $n = 30$. Note that the zero value, or even the

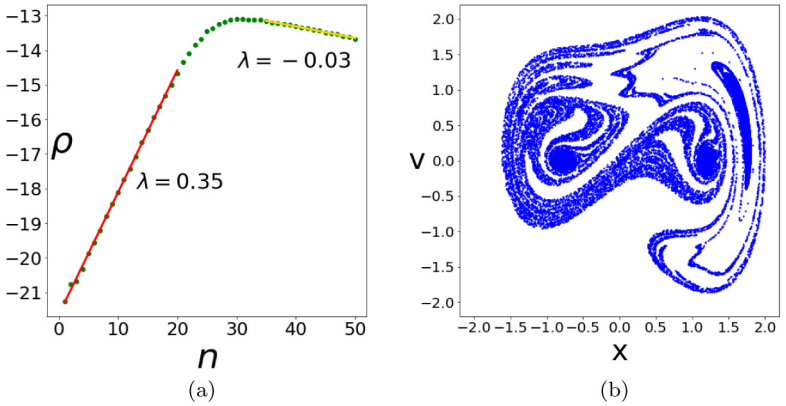

Fig. 24. (a) The EAPD function in the scenario of Fig. 23 up to $n = 50$. (b) The strange snapshot (nonchaotic) attractor at $n = 30$ ($\varepsilon_{30} = 0.174$) where the instantaneous Lyapunov exponent vanishes. This is the image of the attractor in Fig. 23(a) 5 iterations later.

negativity of the average Lyapunov exponent does not mean that there is no chaos at all, since individual trajectories can indeed be sensitive to initial conditions, but these are outcompeted by those converging towards the SNPs, thus we are justified in calling the overall dynamics non-chaotic.

However, a surprising phenomenon occurs when we continue to plot the EAPD curve (Fig. 25(a)): at around $n = 54$, for a short time interval the overall dynamics turns chaotic again, with a smaller positive Lyapunov exponent than before. After this the function again reaches a maximum and starts to decrease. The reason for this can be seen if we observe the attractor after this shift, at $n = 60$ (Fig. 25(b)) where it is clear that the two SNPs around $(\pm 1, 0)$ have disappeared, and only the third one remains. This suggests that points that have accumulated around the two disappeared SNPs start to be attracted by the remaining one. Also, the positive Lyapunov exponent suggests that these points first wander around the chaotic saddle before starting to converge. We note, however, that this chaotic saddle is *different* from the one that existed up to $n = 54$, since now the dynamics in the area around $(\pm 1, 0)$ is chaotic as well, which can also be observed in Fig. 25(b). The saddle belonging to $n = 60$ is shown in Fig. 25(c), and compared with the one in Fig. 23(c), it has a narrower and more sparse structure.

The values of the positive slopes in Fig. 25(a) suggest that this saddle is less chaotic than the one before, however this can be misleading since by now several points have already accumulated around the only remaining SNP, meaning that those skew the statistics towards a flatter slope. In order to obtain more accurate results, we consider the EAPD curve of a scenario with the same rate and the same β vale, but starting with an extended ensemble at $\varepsilon_{54} = 0.249$, i.e. at the beginning of the second positive slope in Fig. 25(a). This EAPD curve is shown in Fig. 25(d), and it shows that, in fact, this saddle has a larger instantaneous Lyapunov exponent than the preceding one (the first slope in Fig. 25(a)).

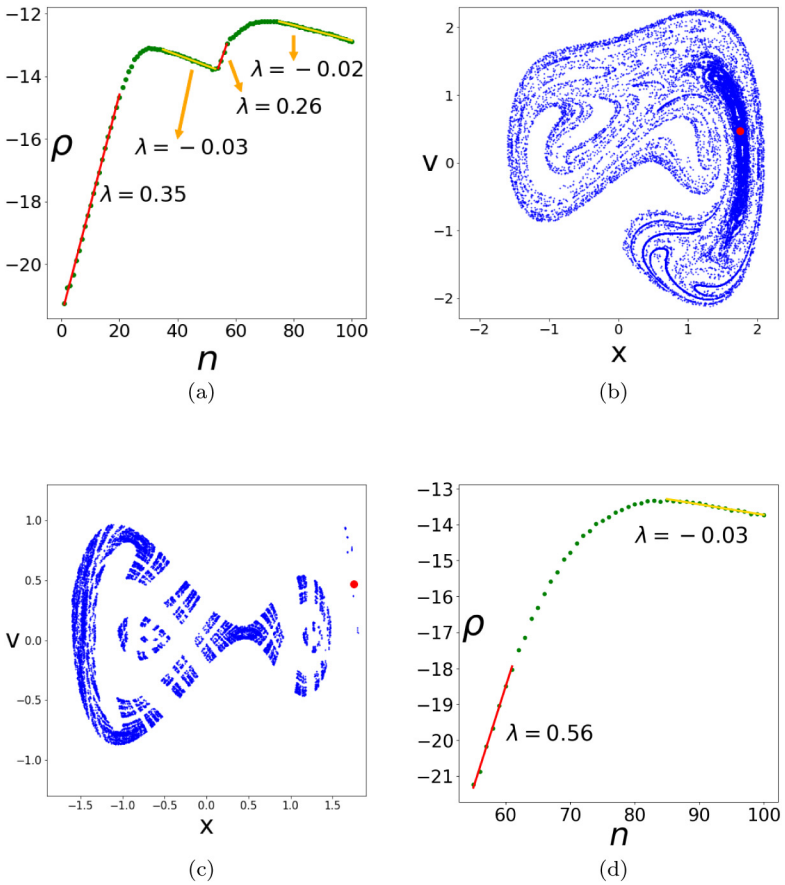

Fig. 25. (a) The EAPD function in the scenario of Fig. 23 plotted up to $n_{max} = 100$. (b) The snapshot attractor at $n = 60$ ($\varepsilon_{60} = 0.268$) where it possesses a positive Lyapunov exponent again. The single SNP existing here is plotted as a red dot. (c) The chaotic saddle inside the snapshot attractor at time instant $n = 60$ obtained with numerical parameters $k_s = 5$, $N_{ext} = 90000$. It contains the previous SNPs about $x = \pm 1$ converted into SHPs. Escape occurs upon entering a disk of radius 0.1 around the only SNP. (d) The EAPD function initiated on an extended ensemble at $n = 54$, corresponding to $\varepsilon_{54} = 0.249$. The positive slope corresponds to the Lyapunov exponent of the saddle in panel (c).

5.3. Natural measure on the strange snapshot attractor

We have seen that embedded into a strange snapshot attractor one finds a chaotic saddle and a few regular attracting points, SNP-s. Since a saddle is a non-attracting set, the natural measure $P^*(\mathbf{x}, t)$ of the attractor will have a tendency to accumulate about the regular points. The process might, however, take a long time. The time evolution of the natural measure is illustrated by the tableau of Fig. 26, in the scenario considered in this section. The convergence time t_c to the attractor was found to be 8 periods, thus the instances shown are a faithful representations of the dynamics.

On panel (a) we see the distribution on the attractor of Fig. 23(a) at $n = 25$, and the distribution is without any large peaks, although the density is markedly lower at the front and back edges of the attractor, plotted in blue. Panel (b) belongs to the time instant of the first maximum, $n = 30$, of the EAPD curve of Fig. 25(a), where the slope is zero, the instantaneous Lyapunov exponent vanishes. The extended and fractal nature of the distribution supports the view that the attractor is a strange non-chaotic attractor here. Note that this suggests that the disappearance of the average Lyapunov exponent does not necessarily mean that the distribution has to be trivial. The next panel exhibits the density at $n = 50$ about the end of the downward slope of the EAPD curve, where the Lyapunov exponent is negative. The regular attractors dominate, and one indeed sees two pronounced peaks at about $(\pm 1, 0)$ and an even larger one at the third SNP, while considerable portions of the filamentary pattern of the attractor are hardly populated. The distribution is even less uniform than before (but still a fractal), this is still a strange non-chaotic attractor. When going further, the two peaks disappear, indicating that the corresponding SNP-s became parts of the attractor (see Fig. 25(b), which is again a case of a strange snapshot attractor with a positive largest Lyapunov exponent). Finally, we show the distribution belonging to $n = 70$ in panel (d), where the EAPD slope is zero again, to illustrate that the attractor at this instant is another strange non-chaotic attractor, dominated by the peak at the third SNP.

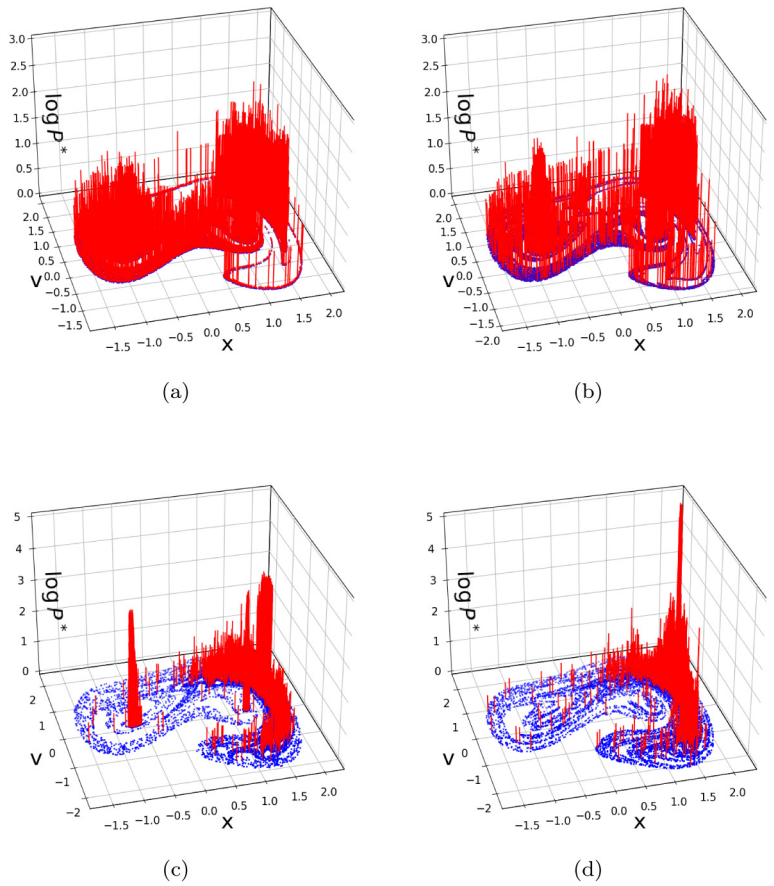

Fig. 26. Natural measure (red) on the strange snapshot attractor (blue) along the scenario used in this section, for instances $n = 25, 30$, belonging to Figs. 23(a) and 24(b) (panels (a) and (b)), and $n = 50, 70$ ($\varepsilon_{50} = 0.237$, $\varepsilon_{60} = 0.300$) (panels (c) and (d)).

5.4. Time-dependent basin structures

The stable foliation, shown in Figs. 23(b) and 23(c) in pink, turns out to be fractal-like (with zero area) and does not shade any area, while it penetrates into regions outside the shown frame as well. This is in contrast to the case of a chaotic snapshot attractor, where the stable foliation is space filling. The reason for this is that the saddle occupies only part of the attractor, so the set along which it can be reached must not be space filling. However, the whole strange snapshot attractor is the only attracting set governing the dynamics, thus its basin of attraction must be the whole phase space. It is then worth investigating if the gaps in the snapshot stable foliation could be filled.

Given the existence of the three simple attractors, SNPs in our example in Fig. 23, it is natural to ask where their basins of attraction are. These are also sets, just like the stable foliation, that describe points that converge to an object, an SNP, but these have finite area. Since SNPs are time-dependent, being snapshot objects, their basins should be also time-dependent.

To observe the basins of attraction, consider Fig. 27(a) in the scenario investigated. The basins of attraction are approximated by choosing compact regions about the SNPs at time $n = 35$ and iterating N_{bas} points in them *backward* in time over $k = 10$ units (the same auxiliary time that is used for the stable foliation). The basins of the SNPs about $(-1, 0)$ and $(1, 0)$ are colored green and yellow, respectively, while that of the third one (being at about $(1.7075, 0.6335)$ at $n = 35$) blue. One clearly sees that all three colors become mixed in extended regions.

The figure also contains the stable foliation of Fig. 23 plotted in pink, superimposed on the three basins. Bands of all three colors of the regular basins are seen to penetrate the tongues left empty by the stable foliation. White regions are also visible as consequences of the fact that the chosen compact regions do not fully match the basins, not even close to the SNPs. With an appropriately refined choice, however, the white areas would shrink. Since the regular basins' colors appear to be mixed with pink, we can say that the boundary of the basins accumulate on the snapshot stable foliation. We see here a case of a *snapshot fractal basin boundary*, that is, the sets that transport points to the snapshot chaotic saddle, as well as the SNPs, are time-dependent. A special class of boundaries is called the Wada boundary [37,100] if it is true that any small neighborhood of the fractal boundary contains all three (or more) basins. Since all colors are equally well mixed in our case, we suspect to see here a snapshot Wada type boundary. The three colors of the regular basins (up to the white patches) appear to cover the whole plane, indicating that the three SNPs (and therefore also the strange snapshot attractor) attract points in a space-filling way.

In Fig. 27(b) we illustrate the "basin structure" in the case of the snapshot attractor displayed in Fig. 25(b). Here two of the three SNPs no longer exist, thus the image contains only two colors, the white patches again come from not being able to perfectly cover the basin of the single SNP with compact regions. In pink we show the stable foliation, i.e. the time-dependent set along which points are attracted to the saddle. The basin of attraction of the remaining SNP is plotted in blue (just like in panel (a)), which now becomes space filling. The Wada-type mixing of basin boundaries present in panel (a) however has completely disappeared. These observations illustrate that the regular component(s) of strange snapshot attractors are robustly attracting.

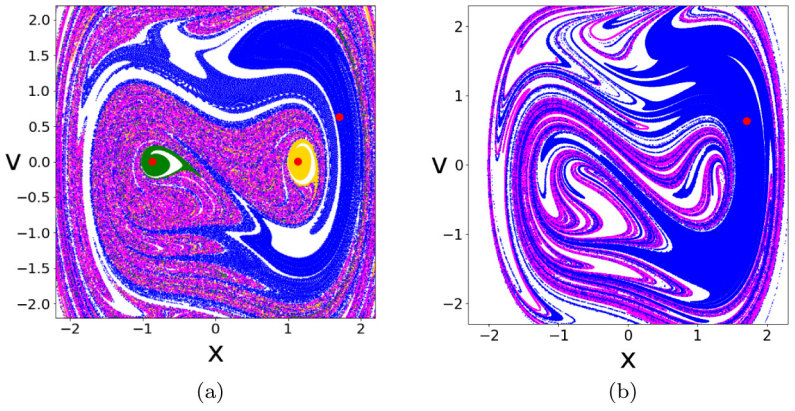

Fig. 27. (a) Basins of attraction of the three time-dependent attractor points at time $n = 25$ superimposed with the stable foliation of Fig. 23. The initialization for generating the basins occurs at $n = 35$ with $N_{bas} = 40000$ points in a circle (green and yellow) of radius 0.15 around the SNPs at $(\pm 1, 0)$ and in three (blue) rectangles around the SNP close to $(1.7075, 0.6335)$, centered at $(1.75, 0.5)$, $(0, 1.4)$, $(1.2, -1.4)$, of sizes 0.15×1, 1.5×0.2, 0.5×0.5, after which a backward iteration is applied over $k = 10$ time units. (b) The "basin structure" for $n = 60$ in the same scenario, belonging to the attractor of Fig. 25(b). In the construction of the foliation and the basin we have $k = 5$ with $N_{fol} = 200000$ and $N_{bas} = 90000$ trajectories. The latter number of points are distributed on each of the four initial rectangles centered at $(1.75, 0.1)$, $(0.9, 1.25)$, $(1.2, -1.3)$, $(1.3, -1.4)$ and of sizes 0.15×1.1, 0.8×0.6, 0.5×0.3, 0.15×0.55. at $n = 65$.

5.5. Time-dependent escape rates

A novel feature can be observed when considering the time evolution of the number of points remaining near the saddle of Fig. 23(d): the escape from the saddle is *not exponential*, as it can be seen in Fig. 28(a). This means that, contrary to traditional transient chaos (e.g. Fig. 18), here the dynamics cannot be described by one single escape rate, rather *the escape rate itself is changing in time*.

Generally, this time-dependence manifests in the derivative of the curve in Fig. 28(a). Let $N(t)$ and N_n give the number of survivors in continuous and discrete time, respectively. The time-dependent escape rates are then obtained as

$$\kappa(t) = -\frac{d}{dt}\ln N(t) = -\frac{\dot{N}(t)}{N(t)}, \quad \kappa_n = -\frac{\ln N_n}{\Delta t} = -(\ln N_{n+1} - \ln N_n) = -(\ln N_n)' \tag{40}$$

This is illustrated in Fig. 28(b), by numerically computing the derivative. In traditional transient chaos, the decay with $\exp(-\kappa t)$ starts after a convergence time only, needed by the ensemble to approach the chaotic saddle along the stable manifold. An example of convergence is provided by the beginning of the curve in Fig. 18(d). In the time-dependent context, we shall denote the convergence time after which the snapshot chaotic saddle is reached by $\tilde{t}$ and $\tilde{n}$ in continuous and discrete time, respectively. Based on this, we conclude that the first few outlier points in panel (a) are a sign of the convergence towards a snapshot saddle and discard them in the analysis, plotting κ from $\tilde{n} = 9$ onward only.

An important message of transient chaos theory is that the positivity of the average Lyapunov exponent does not imply chaoticity. A simple example is an isolated hyperbolic point, possessing a positive local Lyapunov exponent (which is also the average in this case), which is then the same as the escape rate, while of course the dynamics of a single isolated hyperbolic point is not chaotic. What matters is the difference of the two quantities since the global escape from a collection of hyperbolic orbits, the chaotic saddle, is *slower* than the typical stretching rate. This is expressed by the *positivity* of the metric entropy K, which has the form [37,82,101]

$$K = \lambda - \kappa > 0 \tag{41}$$

for systems with one positive Lyapunov exponent λ. A saddle is thus considered chaotic if $\kappa < \lambda$ holds. This statement implies that *typical* transient trajectories exhibit chaotic behavior before they escape. The general condition for the existence of complex transient dynamics is that the *topological entropy* [102] is positive, a quantity reflecting the exponential growth of permitted transient trajectories, i.e. the complexity of the dynamics. The topological entropy is larger than or equal to the metric one. If these two quantities are different, a fractal looking saddle may exist with $\kappa > \lambda$ as long as the topological entropy is positive.

These relations should hold for time-dependent quantities as well. Calculating the derivative of the EAPD function in Fig. 25(a), i.e. the Lyapunov exponent λ_n, we find that the escape rate κ_n of Fig. 28(b) remains for the first part of the scenario smaller than λ_n, but the difference changes sign at $n = 27$. Since the metric entropy is negative for $n > 27$, we can say that the saddle is a *strange nonchaotic saddle* in this range, implying that there are many trajectories exhibiting sensitivity to initial conditions, but they are atypical. Since this saddle is the chaotic component of the strange snapshot attractor, in a transient chaos based view, it should be said that the attractor is non-chaotic already for $n > 27$ (not only for $n > 30$ stated so far). This condition is illustrated by a black line in Fig. 28(b). Note however, that the topological entropy is expected to be positive for quite a long time, as long as the attractor appears to be fractal-like.

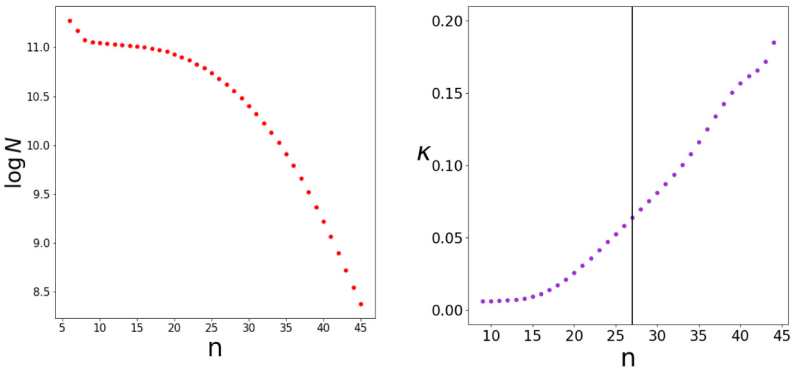

Fig. 28. (a) Number of survivors N_n in the rectangle mentioned in Fig. 23 in the scenario used there. The curve is not linear on the semi-logarithmic plot, thus the escape is not exponential here, meaning that it should be described by time-dependent escape rates. (b) Time-dependence of the escape rate κ based on the numerically obtained derivative of the curve in panel (a). In instants before the vertical line at $n = 27$ the snapshot saddle is chaotic, while after it the saddle is strange non-chaotic, and the figure shows that the escape rate remains defined in the latter case as well.

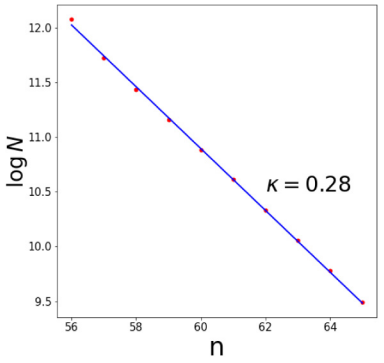

Fig. 29. Number of survivors for the snapshot chaotic saddle of Fig. 25(c), existing for $n > 54$, in the scenario $\varepsilon_0 = 0.08$, $\alpha = 0.0005$, $n_{max} = 100$, with $\beta = 0.01$, associated with the strange snapshot attractor of Fig. 25(b), The escape is now exponential, contrary to Fig. 28.

It is worth noting that the presence of a time-dependent escape rate does not imply that the naively expected relations

$$N(t) \sim e^{-\kappa(t)t}, \quad N_n \sim e^{-\kappa_n n} \tag{42}$$

would be valid. As follows from the relations in (40), the exponents should contain a time *integral*, or a *sum*, over the previous instances. The correct relations, valid after the convergence time $\tilde{t}$, $\tilde{n}$, are

$$N(t) = \tilde{N} e^{-\int_{\tilde{t}}^{t} \kappa(t')dt'}, \quad N_n = \tilde{N} e^{-\sum_{\tilde{n}}^{n} \kappa_i}, \tag{43}$$

where $\tilde{N}$ is the number of non-escaped particles at the instant of $\tilde{t}$, $\tilde{n}$. These might lead to results differing considerably from those of the naive estimates (42) since a value taken at the last instant multiplied by a time interval is not the same as the integral of the investigated quantity over the time interval.

After $n = 54$, and the disappearance of two SNPs, the chaotic saddle becomes different, as can be seen in Fig. 25(c), it is thus worth separately calculating κ for this case. Using the same method as before, the result shown in Fig. 29 is quite interesting in view of the previous example: *the escape becomes exponential*. Not only that, but the linear fit results in the escape rate $\kappa = 0.28$, which is larger than the values in Fig. 28(b), meaning that now the escape is faster than before. An explanation might be related to the basins of attraction in Fig. 27. With the disappearance of two SNPs on panel (b), the Wada-type basin boundary vanishes, after which, once a trajectory leaves the vicinity of the saddle, it can only escape one way, towards the one remaining SNP. In the case of panel (a) however, one can speculate that the extended Wada-type boundary allows the trajectory to "hesitate" between which SNP it would eventually escape to, meaning that in this case escape is *slowed down* by the time-dependent Wada-type basin boundary.

5.6. Transition between the weak and robust regimes

We have seen that chaotic snapshot attractors exist in the robust regime (illustrated with driving and damping $\varepsilon \sim 0.55, \beta = 0.2$), while in the weak regime (illustrated with driving and damping $\varepsilon \sim 0.2, \beta = 0.01$) the snapshot attractor is strange. We found that a transition can be shown to occur between these qualitatively different types of snapshot attractors, and this is what we investigate in this section.

We start with the frozen system, and generate the bifurcation diagram along a *curve* of the (ε, β) plane, i.e. we change these parameters simultaneously, according to a functional relation between them. We have found that a linear relation

$$\varepsilon - \varepsilon_0 = s(\beta - \beta_0) \tag{44}$$

suffices, where β_0 is the damping constant belonging to the driving amplitude ε_0. For the constant parameters we choose the values $s = 1.92$, $\beta_0 = 0.032$, $\varepsilon_0 = 0.1$ (in the weak regime).

Fig. 30 shows this two-parameter bifurcation diagram obtained by cutting out short transients only. Fixed point attractors appear in this view as bold, black curves. It is clear that the two basic attracting fixed points originating from $x = \pm 1$ exist up to about ($\varepsilon \approx 0.23$, $\beta \approx 0.12$), and are surrounded by transient chaos in the whole of this interval. After this parameter pair, the bifurcation diagram is consistent with the presence of a single extended chaotic attractor which undergoes internal crises, and ceases to exist at the far right of the picture.

As a next step, we apply a drift in *both* ε and β with rates α and γ, respectively, and investigate the fate of snapshot attractors. The drift follows the line prescribed by (44) in the parameter plane with the choice $s = \alpha/\gamma$. We thus consider a Duffing system with two time-dependent parameters:

$$\ddot{x} = x - x^3 - 2\beta(t)\dot{x} + \varepsilon(t)\cos\omega t, \tag{45}$$

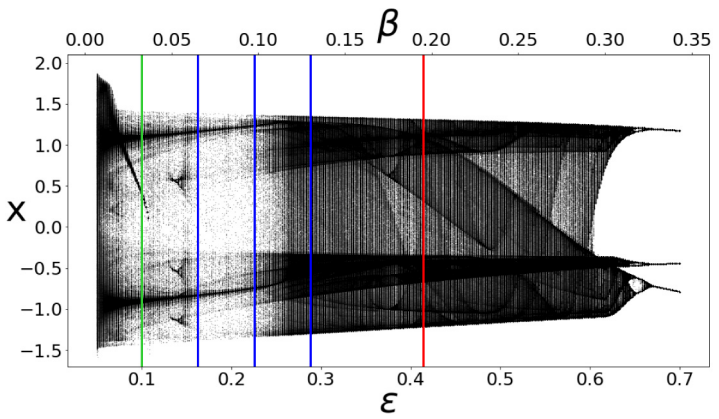

Fig. 30. Bifurcation diagram taken along the $\varepsilon(\beta)$ line (44) of the parameter plane with $s = 1.92$ by cutting out short transients of length 25 iterations only. The green line is at the chosen values of $\varepsilon_0 = 0.1$, $\beta_0 = 0.032$, blue lines: $\varepsilon = 0.162, 0.225, 0.288$, $\beta = 0.064, 0.097, 0.130$, red line: $\varepsilon = 0.414$, $\beta = 0.195$. The lines colored blue and red mark values at which snapshot attractors are shown in Fig. 31 in a scenario with two drifting parameters.

taken at stroboscopic instances $t = Tn$, with parameter drifts as

$$\varepsilon(t) = \varepsilon_0 + \alpha t, \quad \beta(t) = \beta_0 + \gamma t, \quad 0 \le t \le t_{max}. \tag{46}$$

The rate α is taken 0.0005 as in this section so far, and γ is chosen as $\alpha/s = 0.00026$. The initialization occurs at time $n = 0$ with $N_{ext} = 250000$ points distributed uniformly on a square of side length 3 centered at the origin. This parameter pair is marked by a green line in Fig. 30.

Before showing the snapshot attractors along this scenario, let us note that as long as the two basic attracting fixed points originating from $x = \pm 1$ exist, there should be two regular snapshot objects, SNPs, close to their location in the bifurcations diagram. (The precise locations were calculated for weak driving in Section 2, but the results are not applicable for about $\varepsilon > 0.2$.) The SNPs are expected to disappear approximately at the ε, β values where the fixed points cease to exit. Afterwards the SNPs might become converted into unstable SHPs, a possibility we have discussed in Section 3.4. The disappearance of SNPs marks the emergence of chaotic snapshot attractors. In view of this discussion, the structural changes visible in the shape of snapshot attractors in the sequence shown in Fig. 31 is easy to interpret.

Panel (a) arises at iteration $n = 20$ and belongs, from the point of view of parameters, to the first blue line in Fig. 30. The snapshot attractor contains two dense patches about $x = \pm 1$, in accordance with the existence of two SNPs there, as well as a filamentary part connecting them. Its shape is similar indeed to that visible in Fig. 23(a), without the third SNP specific to that case. (The bifurcation diagram of Fig. 30 also contains a third fixed point, originating from the top left, which ceases to exist at about $\varepsilon = 0.11$.) The situation is similar in panel (b) ($n = 40$, second blue line in Fig. 30) just the dense blue regions are shifted more to the right and have shrank, as a considerable amount of trajectories converged towards the SNPs, which is also apparent on the emptier filamentary regions. The dense regions are no longer present in panel (c) ($n = 60$ third blue line in Fig. 30) marking the loss of SNPs and the conversion into a chaotic snapshot attractor. It is not yet densely populated, since (based on the bifurcation diagram) the SNPs have just disappeared, meaning probably that the earlier densely populated regions have now been transported away from $x = \pm 1$, but are not yet fully stretched. The last panel exhibits the snapshot attractor at $n = 100$ (red line in Fig. 30), at parameters $\varepsilon_{100} = 0.414$, $\beta_{100} = 0.195$. This attractor is indeed similar in appearance to that of Fig. 6. The sequence of Fig. 30 illustrates that there exists a transition from strange to chaotic snapshot attractors when going from the weak towards the robust regime. At the beginning of the transition the process is non-adiabatic for the attractor, while the frozen attractor belonging to panel (d) is found to be very similar with the one shown, tracking, and thus adiabaticity, holds by the end of the scenario.

6. Advanced features in Hamiltonian systems

It is worth differentiating between two cases related to Hamiltonian systems too. One of them is such a scenario where the dynamics is becoming more chaotic over time, called a *chaos enhancing scenario* (treated up to now), while the other is one where the strength of chaos is ever decreasing, the *chaos weakening scenario* (to be discussed in Section 6.4). In the former, snapshot tori typically break up and the size of the snapshot chaotic sea is growing, while in the latter tori do not break up. In the context of our system with a linear parameter drift, the enhancing and weakening scenarios correspond to a positive rate and a negative rate α, respectively. Note that the fact that such a clear distinction can be made is a beneficial property of our specific system and the chosen drift.

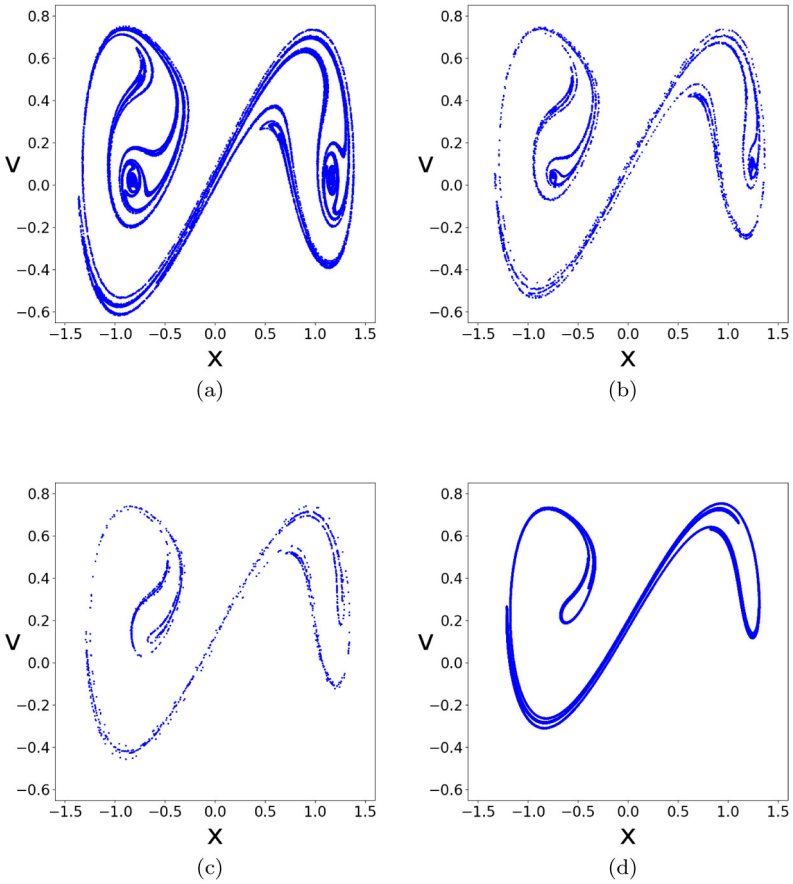

Fig. 31. Snapshot attractor in the scenario $\varepsilon_0 = 0.1$, $\beta_0 = 0.032$, $\alpha = 0.0005$, $\gamma = 0.00026$, $n_{max} = 100$, with $N_{ext} = 250000$ points distributed initially on a square of side length 3 centered at the origin, shown at discrete times (a) $n = 20$, (b) $n = 40$, (c) $n = 60$, and (d) $n = 100$.

6.1. Predicting the torus break-up

The phenomenon of torus break-up, characteristic of chaos enhancing scenarios, was mentioned in Section 3.1 as a dramatic event in the history of a snapshot torus, the process during which it loses the smooth loop character, i.e. when it gets entrained into the snapshot chaotic sea. We note that, besides the features mentioned at the end of Section 3.5, this process can also be loosely considered as an example of rate induced tipping [58] since a transition occurs between two distinct states, regular and chaotic dynamics. In this section we concentrate on the dynamical condition of torus break-up. A hint in this direction might be provided by a careful observation of Fig. 21(a) where one discovers that in certain regions the pink snapshot stable foliation slightly overlaps with some of the blue tori belonging to the same time instant. Such a behavior would be impossible in traditional chaos, where phase space curves are forbidden to cross each other. This is, however, not impossible in systems subjected to parameter drift. Since the stable foliation directs points into chaos in the future, an intersection of this foliation and a torus at a certain instant means that the intersection region will be mapped into a chaotic region at some later time, implying the break-up of the torus.

Concerning previous efforts, the first attempt in understanding the mechanism was the observation in [35] that the stable manifold of a snapshot hyperbolic point (SHP), which can be perturbatively determined for small driving amplitudes, can be used to signal torus break-up. The stable manifold is generated from a small segment along the local stable direction of the SHP, which itself lies in the chaotic sea. If a minimum of k backward iterates are needed to have an intersection with a given torus *at time zero*, then it was said that the break-up of that torus starts approximately k time units later. In the discrete-time problem treated in [36], where identification of SHPs was hopeless, a similar condition was found with the stable manifold of hyperbolic points of the drift-free problem. This observation showed that the precise knowledge of the SHPs is not needed for finding the condition of torus break-up, and a more robust feature of the dynamics, the snapshot stable foliation can be used.

Here we thus present this mechanism in detail, using the general language of time-dependent foliations. The torus selected as an example is the red torus on the right of Fig. 7(a). This curve belongs to the initial instant, and we are interested in the moment when the break-up process of this torus starts in the scenario followed in that figure. To this

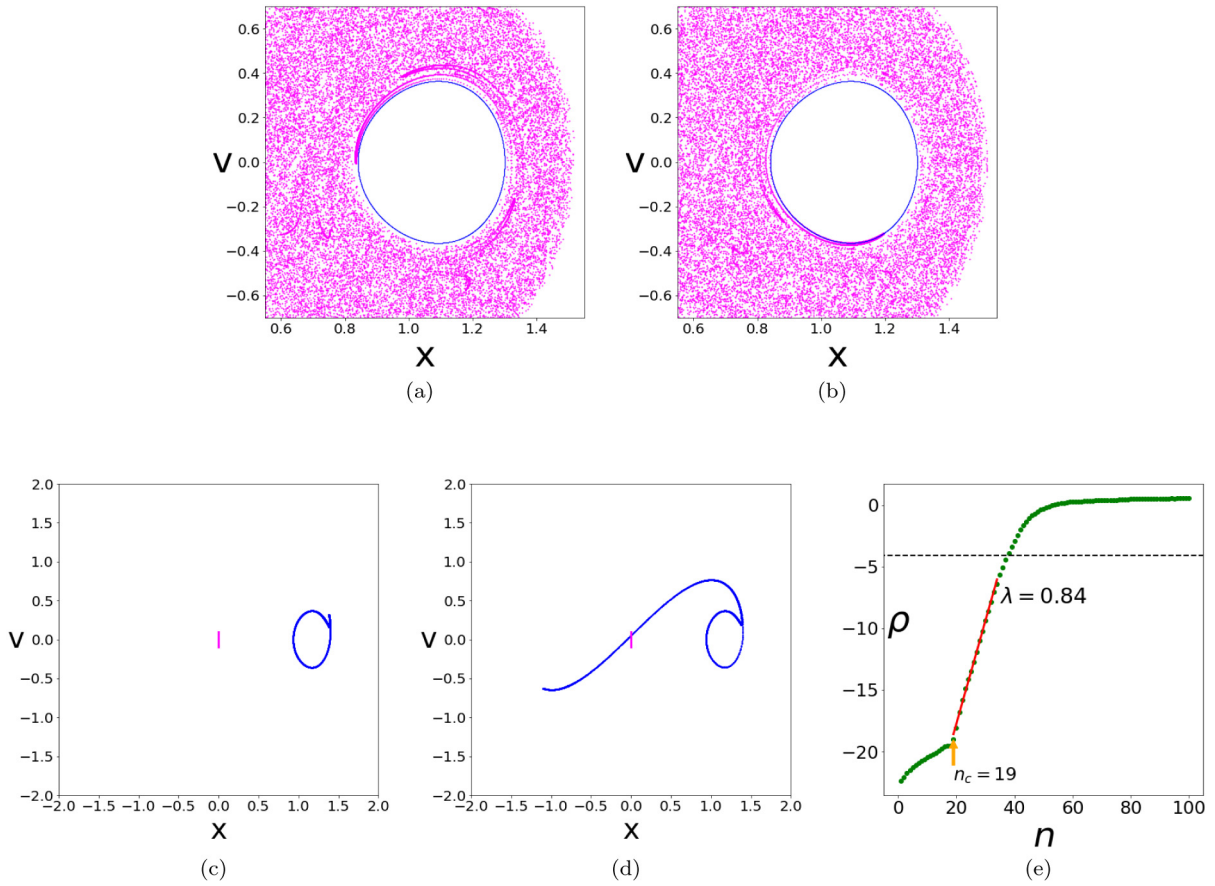

Fig. 32. Dynamical condition for torus break-up in the same scenario as in Fig. 7 ($\varepsilon_0 = 0.08$, $\alpha = 0.0005$, $n_{max} = 100$). In panels (a), (b) the red torus on the right of panel (a) of Fig. 7 is shown in blue (at the initial time instant $n = 0$). The stable foliation (pink curve) was generated by iterating the same initial segment of length $dl = 0.2$ around the origin (marked pink in panels (c), (d) with $N_{fol} = 100000$ points on it) backward over $k = 18$ and 19 time periods in panels (a) and (b), respectively. Panels (c) and (d) show the image of the torus after 18 and 19 iterations, respectively. Note that in the latter, the deformed torus intersects the small segment. Panel (e) exhibits the EAPD curve belonging to the time evolution of the torus.

end, we keep looking at the torus at the initial instant, but compare it in Figs. 32(a) and 32(b) with the stable foliation generated via backward iterations initiated at different k time units later on a small segment (marked by pink in panels (c) and (d)) in the middle of the chaotic sea. In panel (a) $k = 18$, i.e., we see the stable foliation at the initial time instant which leads to chaos by time $n = 18$. The pink curve comes quite close to the torus, here plotted in blue for contrast, but remains outside it, indicating that the image of the torus will not yet be in the chaotic sea after $n = 18$ steps. In contrast, with $k = 19$ (panel (b)) a crossing of the same blue curve can be seen at the bottom of the torus. This implies that some portions of the image of the torus are in the chaotic sea after $n = 19$ steps, i.e., the break-up process has started.

Panels (c) and (d), showing the image of the torus at time instants $n = 18$ and 19, respectively, fully support this expectation as the snapshot torus is yet about its original location in panel (c), but one step later has developed a long tongue crossing through the origin, which belongs, at all instants, to the middle of the snapshot chaotic sea. A further feature supporting the view presented is provided by panel (e). It shows the EAPD curve (24) of the torus through the scenario. The initial phase is represented by a rather low value of function ρ, but at a critical $n_c = 19$ a sudden change occurs, and a rapidly increasing phase, indicating chaos, starts. It is therefore natural to consider the critical instant $n_c = 19$ the instant when the torus break-up starts.

The dynamical condition for torus break-up thus appears to be that *the stable foliation originating at time* n_c *intersects, at time* 0, *the snapshot torus* in question, with n_c being the smallest discrete time instant where this intersection occurs. Note that the right EAPD curve of Fig. 11 also characterizes a torus break-up. Although not said there, the argument above implies that the critical time $n_c = 52$ has the property that this is the first instance whose stable foliation intersects the torus (the red one on the left of Fig. 7(a)) at time $n = 0$. A comparison of the two EAPD curves indicates that the critical time depends on the torus in question. Since the red torus on the right is closer to the edge of the elliptic island containing it than the left one, it is natural that the one on the right breaks up earlier.

The phenomenon of torus break-up contributes to a more detailed understanding of the difference between the foliations illustrated in Fig. 10. We have seen, e.g. in Figs. 21(a) and 32(b), that the stable foliation, and only it, penetrates

into the surroundings of tori, as a basic element of the torus break-up mechanism. This implies that the stable foliation is of somewhat larger extent than the unstable one. More generally, we can say that *in chaos enhancing scenarios the stable foliation is more extended* than the unstable one.

6.2. Time-dependent non-chaotic regions

In this section, we intend to explore the fine structures of the snapshot chaotic sea in chaos enhancing scenarios. Fig. 21 clearly indicates that stable and unstable foliations are not fully identical. The intersection points of an instant correspond to the chaotic subset, but there are small regions where the foliations do not overlap. Points belonging *solely* to the stable foliation at n, appearing in Fig. 21(a) in pink for $n = 35$, were not chaotic in the past, since if they were, they would have to be on the unstable foliation as well (which was initiated from chaos k units earlier). These points are also not chaotic at the moment, but are going to be chaotic in the future (after k units), since the construction of the stable foliation starts with a small segment in the chaotic region at time $n + k$, and subjected to backward iteration. Such points correspond to the mechanism that the stable foliation moves snapshot tori towards chaos, just discussed in Section 6.1. Alternatively, points belonging *solely* to the unstable foliation, appearing in green, were chaotic k times earlier but are not so at the moment (at n), and, crucially, will not be chaotic in the future either, due to them not being on the stable foliation. Such a case is exemplified, after magnification, in the upper left inset of Fig. 21(b), the center of which is marked by a yellow square. In this scenario $k = 10$ for the foliations, thus we expect points on the small yellow square to be not chaotic 10 steps later.

To gain further insight, in panel (a) of Fig. 33 the shape of this yellow square is shown $k = 10$ steps later. The panel also contains the unstable foliation belonging to the same time instant ($n = 45$) in green (obtained with the same $k = 10$) and the snapshot chaotic sea in blue. A snapshot torus is also shown, one that is close to the outermost still surviving snapshot torus at this instant and is about to break up in a few steps. Earlier we made the observation, that the unstable foliation is similar in shape to the snapshot chaotic sea, but here we see that they are not exactly the same. Points of the snapshot chaotic sea are plotted in blue if lying close to the foliation, but those being farther away than a threshold value are plotted in red. The threshold value is so small that the shape of the blue region cannot be distinguished by naked eye from the unstable foliation, and the blue points are hardly visible over the green ones. This property will be kept in following analyses of this type, namely Figs. 34 and 37, thus on those figures we omit plotting the foliation, in order to highlight the chaotic and non–chaotic parts of the chaotic sea. In panel (b), the full snapshot chaotic sea can be seen in blue for comparison, along with the selected torus, while panel (c) shows the stable and unstable foliation overlaid, in order to highlight the intersection points.

Panel (a) clearly indicates that the yellow points are indeed *not chaotic* at this later instant, instead, they form a short band *inside the red region*. Note that the yellow trajectories have evolved from a small square that was part of the unstable foliation but not part of the stable, k iterations earlier. A similar statement is expected to be true concerning the origin of most of the red points as well. These mark the region in which the snapshot chaotic sea differs from the unstable foliation at time n, and appear to be close to a torus. In these regions, the dynamics is certainly not chaotic, since chaos would be indicated by the intersections of the snapshot stable and unstable foliations (see panel c), but these regions are not even parts of the unstable foliation, thus cannot be chaotic. The behavior of the yellow trajectories also supports this assertion. Therefore, these regions can be called *time-dependent non-chaotic regions*. It should be noted that this is an

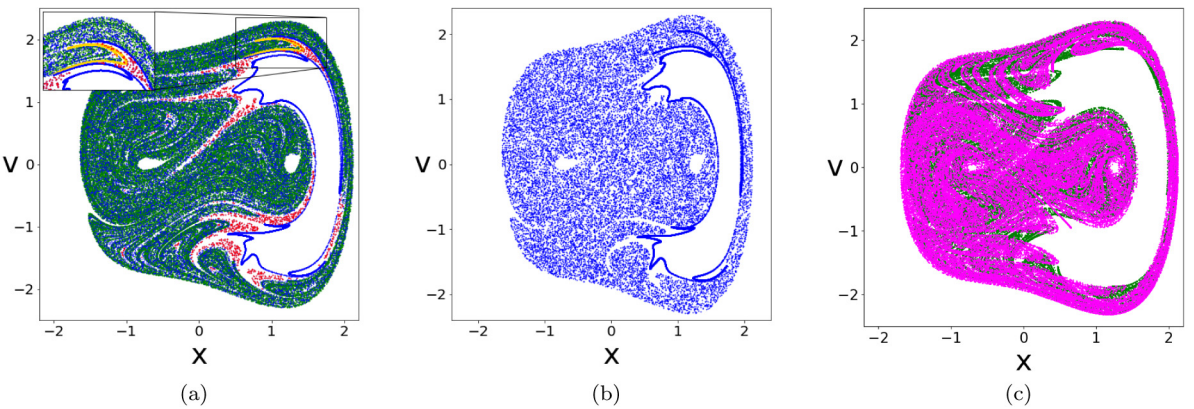

Fig. 33. Snapshot chaotic sea and its non-chaotic component in the same scenario as in Fig. 7 ($\varepsilon_0 = 0.08$, $\alpha = 0.0005$, $n_{max} = 100$). (a) The chaotic sea (blue) compared to the unstable foliation (green) at $n = 45$ generated with $k = 10$, $N_{fol} = 20000$, on 3 vertical sections of length $dl = 0.2$ around points $(-1.5, 0.25)$, $(-0.5, -0.5)$, $(0.25, 0.25)$. The initial conditions at $n = 0$ for the chaotic sea and the shown torus are $x_0 = 0.1, 1.579$, $v_0 = 0$, $N_{tor} = N_{cha} = 20000$. Condition for points of the chaotic sea plotted in red is that their distance from the unstable foliation is > 0.03. (b) The same torus and the chaotic sea shown on their own. (c) Stable (pink) and unstable (green) foliations overlaid.

approximation, the exact non-chaotic region should be defined as the *complement set of the chaotic saddle*. This is thus a larger set than the red region presented in Fig. 33(a), and the difference depends on the density of the intersections on the unstable foliation. Looking at the large number of intersections in panel (c), we can say that here the red region is a good enough approximation of the exact non-chaotic component. This means that, despite being the image of a fully chaotic object, *the snapshot chaotic sea contains both a chaotic and a non-chaotic component*.

At this point, the value of k is arbitrary, subjected to the constraint of a finite observation window (22). It is thus natural to think that the size of the red non-chaotic regions depends on the choice of k. In order to find the optimal value, we recall how the red regions are defined: they are trajectories that were not chaotic k iterations earlier (they were part of the unstable foliation but not of the stable), but were chaotic *another* k iterations earlier (they were inside a chaotic region on a small segment). Now let us have $k' > k$ for the same n, where in a chaos enhancing scenario we find that the non-chaotic component is smaller for k' than for k.[6] We realize that knowing that the non-chaotic trajectories were chaotic $2k$ iterations earlier means that at least $2k$ iterations have to fit into the scenario investigated up to n. This bounds k as $k \leq n/2$, taken together with the condition of not being able to go to negative times due to finite observation (22). In order to have the best-converged results, the maximal available integration time should be taken, i.e. we say that *our numerical method best approximates the non-chaotic component of the snapshot chaotic sea at a given n if the applied auxiliary time is* $k = n/2 \leq k_{max}$ in chaos enhancing scenarios.

We find that for larger n (and thus ε) values in such scenarios the non-chaotic regions all but disappear and the chaotic subset dominates the snapshot chaotic sea. For smaller n values however, pronounced non-chaotic regions can

6 The mechanism is that the extension of the stable (unstable) foliation is larger (smaller) at $n - k'$ than at $n - k$, leading to there being less points that are part of one foliation but not the other at $\varepsilon_{n-k'}$, i.e. smaller non-chaotic regions at n.

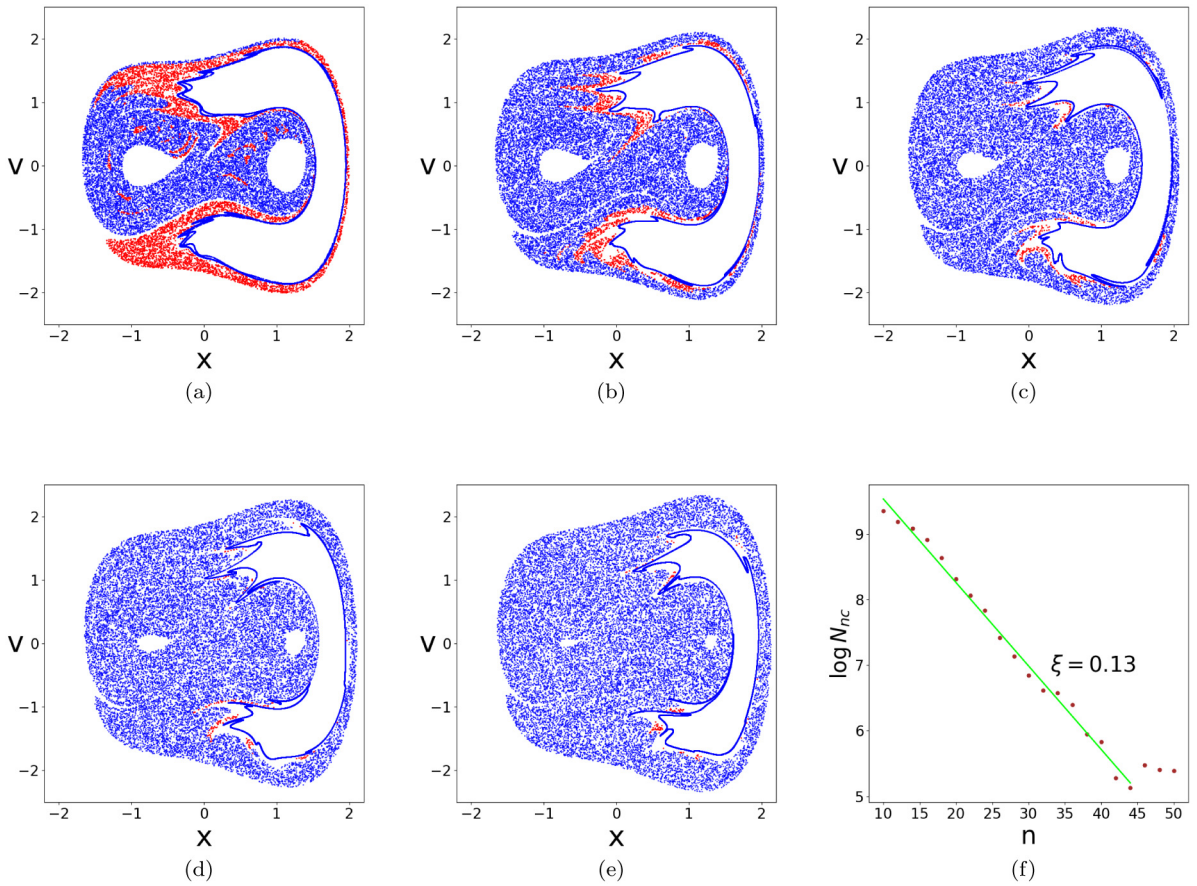

Fig. 34. (a)–(e) The change of the non-chaotic (red) and chaotic (blue) regions of the snapshot chaotic sea in time with fixed auxiliary time $k = n/2$ in the same scenario as in Fig. 33, at instants $n = 10, 20, 30, 40, 50$. In each case, a snapshot torus close the outermost one is displayed from the island on the right, corresponding the initial conditions $x_0 = -0.4, -0.3, -0.15, 0.05, 0.25$, $v_0 = 1.1$ for panels (a)–(e) (at $n = 0$), generated from $N_{tor} = 20000$ points. Initial conditions for the snapshot chaotic sea are $x_0 = 0.1$, $v_0 = 0$, and $N_{cha} = 20000$. The condition for points of the chaotic sea plotted in red is that their distance from the unstable foliation (not shown) is > 0.03. (f) The number of non-chaotic trajectories (red points in panels (a)–(e)) against time on a semi-logarithmic plot. The fitted straight line implies that the non-chaotic region disappears at an exponential rate.

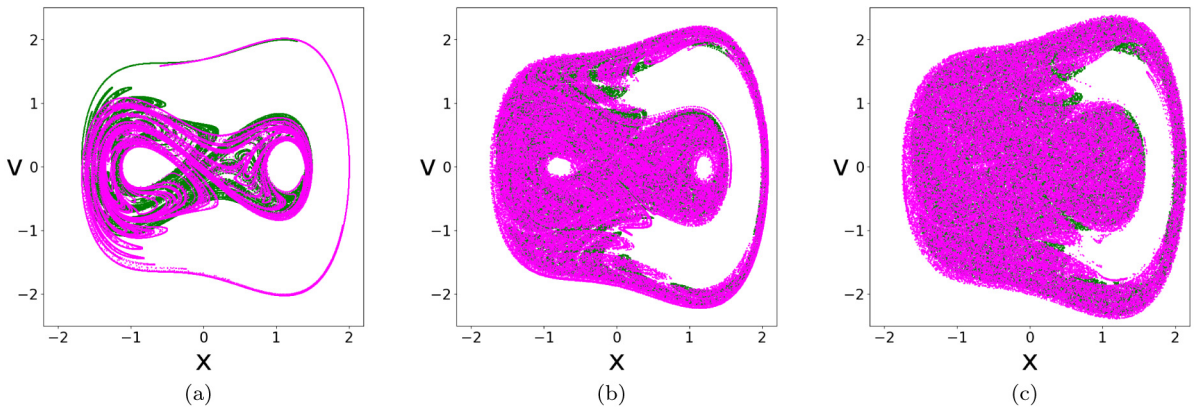

Fig. 35. The two foliations (stable in pink, unstable in green) overlaid for $n = 10$, 30 and 50, $k = 5$, 15 and 25, in panels (a), (b) and (c), respectively.

be observed. This is illustrated in Fig. 34, where we show the snapshot chaotic sea with the chaotic subset (blue) and the non-chaotic regions (red) in the same scenario as before, for instants $n = 10, 20, 30, 40, 50$, where the parameter values are $\varepsilon_n = 0.111, 0.142, 0.174, 0.205, 0.237$, generated with the optimal choice of $k = 5, 10, 15, 20, 25$. Observe that at the beginning the red area is of similar size than the blue, but by the end only very small patches can be found near the outermost snapshot torus. Note that it follows from the mechanism of torus break-up, see Section 6.1 and our observations below, that the stable foliation is a more extended set than the unstable. We thus find here that as time increases, the snapshot unstable foliation (effectively the extension of the blue points) provides a better and better approximation of the chaotic subset, as the time-dependent non-chaotic region disappears. The rate of this disappearance can be observed in panel (f), where we plot the number N_{nc} of non-chaotic points as a function of discrete time n. The curve shows an approximately *exponential* trend with the exponent $\xi \approx 0.13$ obtained from a linear fitting. Note that the observation that the unstable foliation of Fig. 10(a) is similar in shape to the full snapshot chaotic sea of Fig. 8(a) can be understood in the context of Fig. 34: the time instant shown in the former figures ($n = 35$) is between those of panels (c) and (d), in a region where the red points have nearly disappeared.

In order to monitor the above process from the point of view of intersections, we consider three examples from Fig. 34 (panels (a), (c) and (e)) with the stable and unstable foliations superimposed in Fig. 35. In panel (a) the unstable foliation is not yet densely crossed by the stable one, the chaotic saddle is sparse. In panels (b), (c) dense crossings are present, and the unstable foliation is a better approximation of the chaotic subset, the chaotic saddle, more so in panel (c) than in (b).

We conclude that if the scenario and the observational time window allows for such cases, *when the non-chaotic regions disappear completely, the unstable foliation is the same as the snapshot chaotic sea*. This is because the lack of red regions implies that the unstable foliation is completely covered with the stable one, meaning that every point of the unstable foliation is an intersection point, i.e. the saddle occupies the unstable foliation. In such a case, the unstable foliation is also identical with the snapshot chaotic sea, which is fully chaotic. Note that from this it does not follow that the two foliations are identical, only that in a chaos enhancing scenario, the stable is of larger extension than the unstable, such that the latter is completely inside the former. This is also supported by Fig. 35, where for increasing n the stable foliation is shown to cover the unstable one more and more, while another example was shown in [46]. Concerning the question if the unstable foliation, and thus the chaotic subset, is space filling, the numerical results of Fig. 35 suggest that this is approximately the case, while for a more accurate statement further studies are needed, just as for the question of adiabaticity concerning the chaotic subset.

6.3. Time-dependent non-hyperbolic regions

Typical Hamiltonian systems are known to exhibit non-hyperbolic behavior manifesting itself in slow dynamics. Because this implies long lifetimes around certain phase space regions, around last KAM surfaces in particular, the term stickiness is also used for this phenomenon (see e.g., [82,103]). Here we demonstrate that a similar behavior can be observed in systems subjected to parameter drift.

Upon further investigating the time-dependent non-chaotic region, one realizes that this is not a homogeneous set. Fig. 36(a) shows the full snapshot chaotic sea (plotted in blue) belonging to $n = 10$ on its own, i.e. the same instant as Fig. 34(a), an instance when the non-chaotic region is of considerable extension. Within this region, one can see areas of the snapshot chaotic sea that are much more dense than their surroundings, in particular around $x = -0.5$, to the left of the upper and lower tongues of the large torus. These areas, that are parts of the non-chaotic component, bear a clear resemblance to conventional non-hyperbolic (or sticky) regions of chaotic Hamiltonian systems.

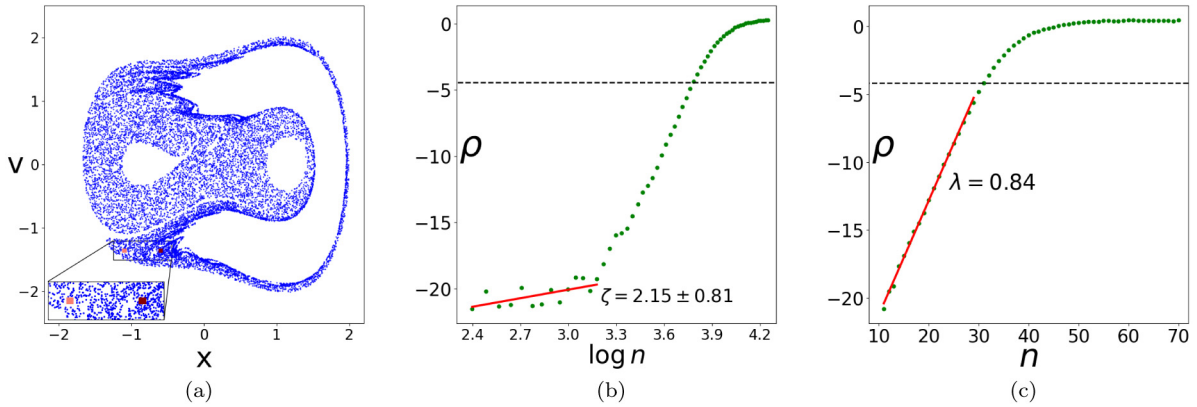

Fig. 36. Signature of non-hyperbolic behavior. (a) Snapshot chaotic sea of instant $n = 10$ in the scenario of Figs. 33, and 34, originated with $x_0 = -0.1$, $v_0 = 0$ and $N_{cha} = 15000$. The non-hyperbolic region can be observed as a more dense region along the inner perimeter of the chaotic sea. The inset shows two squares of side length 0.02, centered at $(-1.1, -1.35)$ (light brown), $(-0.6, -1.35)$ (dark brown). (b) The EAPD curve of the dark brown square on a logarithmic time scale. The linear fit signals power-law-like behavior, with the exponent indicated in the figure. (c) The EAPD curve of the light brown square, indicating chaotic dynamics from the very beginning.

In order to characterize the dynamics of such regions, let us concentrate on the lower left non-chaotic part of the snapshot chaotic sea. Here we investigate the EAPD curves of two small squares, see the inset in Fig. 36(a). The darker brown on the right is inside, while the lighter brown on the left is outside the dense region. Fig. 36(b) shows the EAPD curve of the dark brown square. A logarithmic scale is used along the time axis, since in traditional chaos the distance $r(t)$ of trajectory pairs (the logarithm of which is described by ρ) within a sticky region evolves according to a power-law: $r(t) \sim t^{-\zeta}$ [82]. The initial part of the curve is similar to this: a linear fit can be carried out, resulting in the exponent $\zeta = 2.15 \pm 0.81$. The uncertainty can be attributed to the fact that the dynamics of the region only remains slow for a relatively short time, as the size of the non-chaotic regions shrinks – as we have just seen – at an exponential rate. At around $n = 24$, the average distance of point pairs starts to grow exponentially even starting from this dense region. This instance is between those of Figs. 34(b) and 34(c), where one can clearly observe a drastic decrease in the number of red points. Because of this, the fit in Fig. 36(b) can only indicate traces of the power-law-like behavior, since it is expected to be properly detectable after long times only [82]. Nevertheless, based on the observed accumulation of trajectories around the snapshot tori, as well as the slow dynamics exhibited on the EAPD curve, we call these regions *time-dependent non-hyperbolic regions*. They are a subset of the non-chaotic component of the snapshot chaotic sea, exhibiting prolonged regular dynamics.

As the time-dependent non-hyperbolic region can be observed as a more dense part of the snapshot chaotic sea, it is an interesting question what the fate of the light brown square in Fig. 36(a) is, since this is inside the non-chaotic region, but not in its non-hyperbolic part. Fig. 36(c) shows its EAPD curve, which suggests that its dynamics is immediately chaotic. This is unexpected, since the non-chaotic region certainly does not contain any intersections of the foliations (which signal chaos), as it is not even part of the unstable foliation. However, let us remember that the dynamics of this region was not chaotic k steps earlier, and is not chaotic at n. This, however, says nothing about the *future* (for times larger than n) of the trajectories in this region. They can remain non-chaotic, as is the case for the non-hyperbolic regions, or, evidently, they can turn chaotic even right after the observation, as Fig. 36(c) suggests. This assertion is again supported by the fact that the non-chaotic region disappears exponentially, meaning that it is possible that a large portion of non-chaotic trajectories turns chaotic in a very short time. It is interesting to conclude that what separates the non-hyperbolic regions from the simply non-chaotic ones on an observational level is that *the dynamics of the non-hyperbolic regions remains regular for a considerable time, while the rest of the non-chaotic component becomes chaotic relatively fast*.

6.4. Chaos weakening scenarios and convergence towards integrability

In this section, we explore the relation between chaotic seas and foliations in a chaos weakening scenario, which in our system corresponds to a *decreasing* trend in the driving amplitude. In order to illustrate the essential difference between chaos enhancing and weakening scenarios, let us recall that in Hamiltonian systems subjected to parameter drift, the dynamics is *not invariant* under time-reversal. Due to the particular form of the equation of motion (4) with vanishing dissipation $\beta = 0$, time reversal is equivalent to replacing the rate α by $-\alpha$ and keeping the original time direction, that is following a chaos weakening scenario.

The case of decreasing driving strength was investigated in dissipative cases, leading to the "death of chaos" in [38,45]. Here we concentrate on the Hamiltonian version of this problem, strictly in the context of finite observations. The scenario starts, as before, at $\varepsilon_0 = 0.08$, but the rate is now $\alpha = -0.0003$. Fig. 37(a) shows the phase space at the instance $n = 10$,

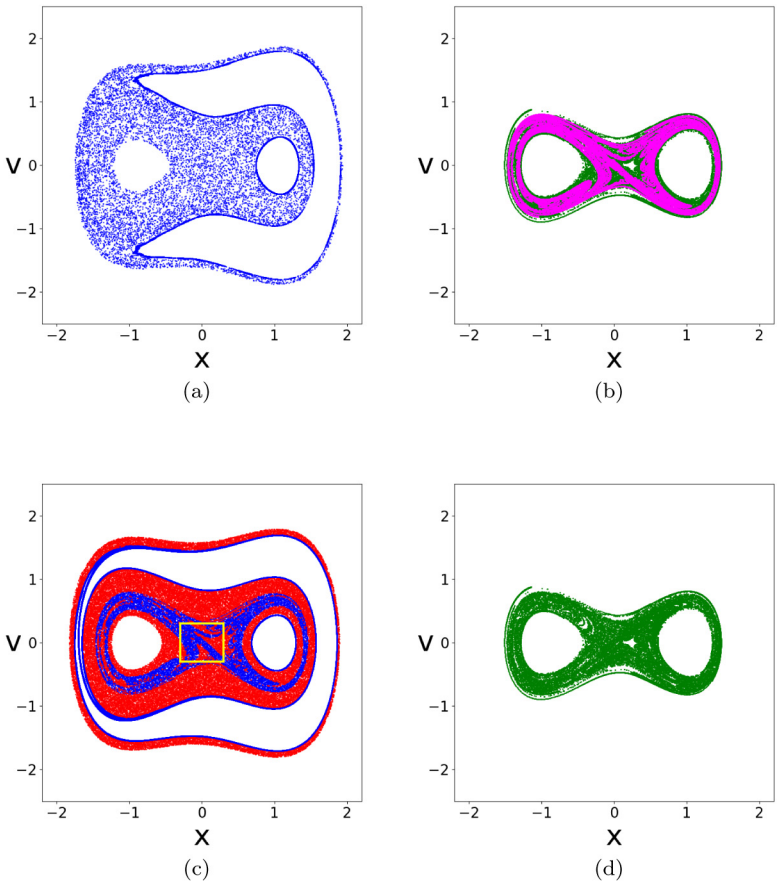

Fig. 37. (a) Phase space of the scenario $\varepsilon_0 = 0.08$, $\alpha = -0.0003$, $n_{max} = 42$ at $n = 10$, $\varepsilon_{10} = 0.061$. The initial conditions at $n = 0$ for the chaotic sea are $x_0 = 0.1$, $v_0 = 0$, while for the snapshot tori $x_0 = 0.78$, $v_0 = 0$ (smaller), $x_0 = -0.61$, $v_0 = 1.3$ (larger), with $N_{cha} = N_{tor} = 10000$. These were originally close to the outermost KAM tori. (b) Foliations (unstable in green, stable in pink), shown at $n = 28$, $\varepsilon_{28} = 0.027$, generated with $k = 14$, and initialized on 3 vertical sections of length $dl = 0.2$ around points $(-0.5, 0.5)$, $(0, 0)$, $(0.5, -0.5)$ with $N_{fol} = 10000$. (c) The snapshot chaotic sea with $N_{cha} = 70000$ at $n = 28$, with the non-chaotic region plotted in red. The threshold for the red points is their distance from the stable foliation being bigger than 0.01, while points closer to the foliation are plotted in blue. The snapshot tori evolving from those shown in panel (a) are also displayed in blue. The yellow frame is a square of side length 0.6×0.6, to be used in the next two figures. (d) The unstable foliation at $n = 28$.

with the snapshot chaotic sea, as well as two snapshot tori which were close to the outermost KAM tori at $n = 0$ in the respective islands. An interesting observation here is that the large snapshot torus is now more elongated than its original shape (see the rightmost island in Fig. 7(a)). This means that snapshot tori can increase in extension (in some directions) with decreasing driving as well. However, neither tori shown in panel (a) exhibit any sign of break-up, which would be signified by strongly stretching patterns in their shapes.

We show the foliations and the non-chaotic region at $n = 28$, where $\varepsilon_{28} = 0.027$, and since we are in a chaos weakening scenario, chaos is expected to exist in a restricted part of the phase space only. Panel (b) indicates indeed that the foliations stretch over a small portion of the phase space only, moreover we find that the stable one (pink) is of smaller extension than the unstable (green), unlike in the chaos enhancing case. We believe that this feature can be generally valid in any chaos weakening scenario. This means that *in chaos weakening scenarios, it is the stable foliation that well approximates the chaotic saddle* in case of a dense coverage of intersection points. These properties appear to be consistent with applying a time-reversal transformation to a drifting system, and leading to the exchange of the roles of the foliations. Because of this observation, and the fact that here we find that the intersection points can be dense on the stable foliation, we approximate the chaotic subset with the stable foliation, and say that the non-chaotic region is its complement set within the snapshot chaotic sea. For completeness, in panel (d) we present the unstable manifold on its own to illustrate that, in a comparison with the pink curve of panel (b), the intersections indeed are dense.

On panel (c) we show the snapshot chaotic sea (the image of the sea of panel (a) 18 steps later). Points farther away than a threshold distance from the stable foliation are plotted in red, and now they cover a more extended part of the phase space than in chaos enhancing scenarios. The chaotic subset is plotted in blue, where the threshold value is again so small that the shape of this region cannot be distinguished by naked eye from the stable foliation. The fact that the

snapshot chaotic sea is much broader than its chaotic subset implies that in such cases *the number of permitted states is large, but the chaotic ones only populate a small region.*

One can also observe on panel (c) the image of the two snapshot tori displayed on panel (a). They do not break up, even at this point in the scenario. The mechanism can be clearly seen in the image: the non-chaotic region effectively forms a boundary between the tori and the chaotic subset (this is more apparent for the smaller torus around (1, 0)). This makes it impossible for the dynamics of the tori to change to chaotic, thus we expect the tori not to break up at later times either. This conclusion complements a similar one made in [45], concerning the avoidance of torus break-up.

Observe that the snapshot chaotic sea, or rather the non-chaotic region, looks as though it broke into two separate sets. The reason for this apparent splitting becomes clear if we observe the large snapshot torus. By this point, its elongation had increased to such a degree that its two tongues have met on the left side, and the torus started to fold onto itself (without breaking up). Earlier in the scenario, the space on the left between the two tongues was occupied by the snapshot chaotic sea, like e.g. on panel (a). With the tongues meeting, only a very narrow band remains where the "outer" part of the chaotic sea can connect to the "inner" one. In principle, traces of this narrow band could even be visible on panel (c) as sparse red points (since it is part of the non-chaotic region) along the blue lines on the left, the meeting point of the tongues. However, in this illustration the blue lines are overlaid on the red points, thus they suppress them.

Note that the last stroboscopic instance in this scenario where the driving amplitude is positive is $n = 42$, where $\varepsilon_{42} = 0.00083$. Since we avoid negative amplitudes, the next instance, $n = 43$, is not allowed, i.e. $n_{max} = 42$. Even at $n = 28$, we see that transverse intersections only occur around the origin, and around the separatrix of the undriven case (green curve in Fig. 1(b)). This is in harmony with the spirit of the KAM theorem, valid strictly speaking in the frozen dynamics only [82], according to which the extension of chaos is proportional to the amplitude of perturbation, which is of order $\varepsilon \sim 0.03$ at that instant.

In order to monitor the scenario towards reaching zero driving amplitude, we define in Fig. 37(c) a relatively small square around the origin (drawn in yellow), and evaluate time-dependent characteristics of an ensemble distributed uniformly on this area at $n = 14$, as shown in Fig. 38. The Lyapunov exponent (panel (a)) decreases in time, the number of non-escaped orbits from this square (panel (b)) goes into saturation, while the escape rate (panel (c)) decreases to zero. The key in the background of this behavior is the white hole in the foliations at about $x = 0.2$, $v = 0$ in Fig. 37(b) and the small red area along the right edge of the square in Fig. 37(c). Both signal a small non-chaotic region at $n = 28$.

In the integrable limit, the phase space of which is plotted in Fig. 1(b), a single hyperbolic fixed point exists, the origin with a large positive Lyapunov exponent. Investigating a very small square around the origin in our scenario, we would see that the Lyapunov exponent tends to this value, and correspondingly, the unstable foliation initiated from a single short interval crossing through the origin would converge to the light green separatrix of Fig. 1(b). The presence of the non-chaotic hole within the yellow square shifts the focus away from the origin. While there is a shrinking chaotic saddle about the origin and along the separatrix, the fact that the number of trajectories do not decrease to 0 extremely rapidly in Fig. 38(b) suggests that there can exist another, weakly chaotic (or non-hyperbolic) set around the hole. Their joint contribution to the ensemble average carried out in the EAPD function leads to a Lyapunov exponent of decreasing trend as shown in Fig. 38(a). Panel (b) illustrates in addition that after about $n = 22$ the very slowly escaping points dominate.

Further insight into this process is provided by Fig. 39. In panels (a) and (b) we present the results of the sprinkler method applied to the yellow square with $N_{ext} = 250000$ points uniformly distributed at instant $n = 14$. Panel (a) and (b) exhibit the points not escaping up to n_{max}, at times $n = 28$ and $n_{max} = 42$, respectively. Formally, these sets are the analogs of the chaotic saddle and its unstable manifold. In fact, the escape from the chaotic saddle about the origin and the

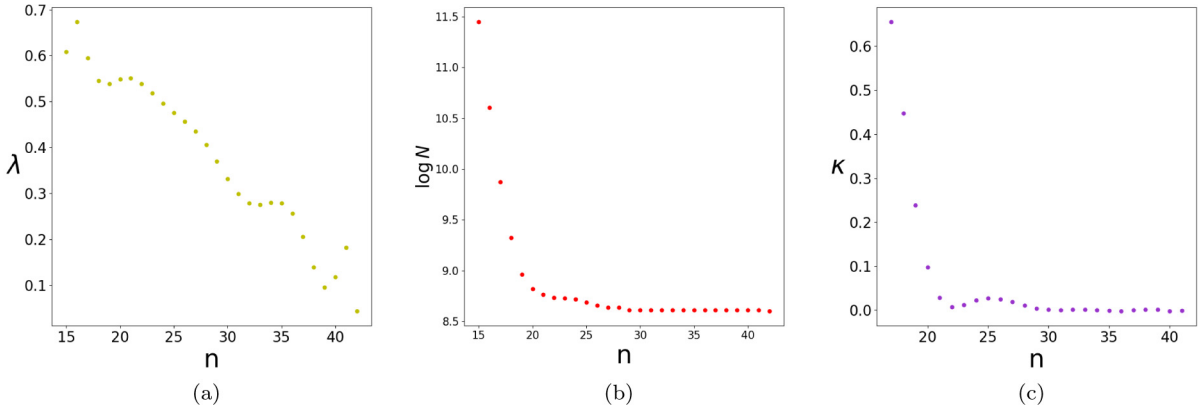

Fig. 38. Quantities evaluated on the yellow, 0.6 × 0.6 square of Fig. 37(c) with $N_{ext} = 10000$ for the EAPD function and $N_{ext} = 250000$ for the escape dynamics. The panels show(a) the Lyapunov exponent, i.e. the discrete-time derivative of the EAPD function, (b) the number N_n of the not yet escaped trajectories, and (c) the escape rate, the discrete-time derivative of $\log N_n$. The quantities are plotted from $n = 15$, $\varepsilon_{15} = 0.052$ up to $n_{max} = 42$, $\varepsilon_{42} = 0.00083$, where the driving amplitude is practically zero.

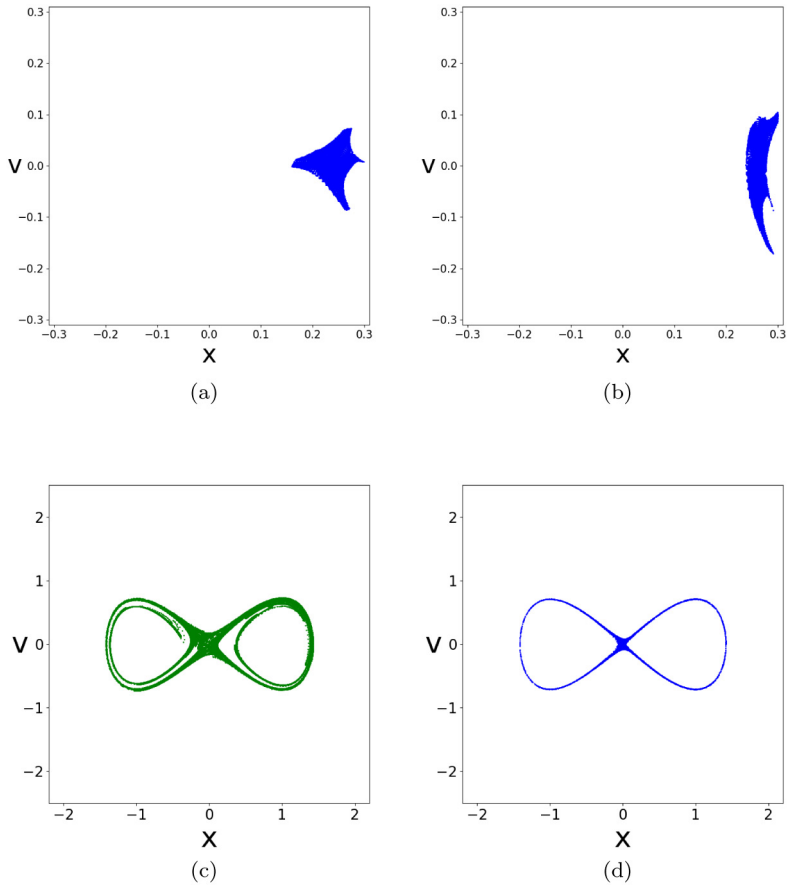

Fig. 39. Approaching the integrable limit. (a)–(b) The shape of the non-chaotic hole at $n = 28$, $\varepsilon_{28} = 0.027$ and $n_{max} = 42$, $\varepsilon_{42} = 0.00083$, respectively, obtained from the sprinkler method, initiated at $n = 14$ with $k_s = 14$. (c) The unstable foliation at $n_{max} = 42$, obtained with $k = 10$, initiated from a section of length $dl = 0.02$ at the origin. (d) The thin frozen chaotic sea at $\varepsilon = 0.00083$.

separatrix is so fast that we do not see any sign of the saddle in panel (a). What we do see is practically the non-chaotic hole which is indeed similar to the white hole visible in Fig. 37(b) at the same instant. The pattern in panel (b) is then the shape of the non-chaotic hole belonging to the practically vanishing driving amplitude at $\varepsilon_{42} = 0.00083$. It has changed its shape, became more elongated, and as a particular feature remains bounded with its longer sides being similar to the phase space trajectories of Fig. 1(b). We therefore conclude that we see here the *convergence towards integrability*.

At the endpoint of the scenario the chaotic subset cannot be generated using our method, since for that we would need to observe the intersections between the foliations, but the generation of the stable foliation by backwards integration from the future is impossible. Here we are facing a natural consequence of the finiteness of the observation window: in the very last permitted instant it is impossible to determine any dynamical quantity being related to the future. The small but positive value of ε_{42} might imply a small chaotic subset along the separatrix, but our method does not allow us to check if it is there. Therefore, on panel (c), we present the only set we are able to reliably provide, the unstable foliation. For comparison, in panel (d), we present the chaotic sea of the frozen Hamiltonian system at the same driving amplitude $\varepsilon = 0.00083$ as at the endpoint of the scenario. In the frozen system, this is the same as the unstable foliation, but its shape is clearly different from the snapshot foliation in panel (c), thus again we see an example for the difference between the drifting and non-drifting dynamics. It is unknown at the moment if there are any methods enabling one to construct the chaotic subset at the endpoint, thus we do not know what the difference is on this level, since from foliations we are unable to identify any intersection points.

It is interesting to mention that the problem of approaching integrability was investigated in [45] for a set-up where the driving amplitude was kept zero after the stroboscopic instant when this value was first reached. In such a case it is meaningful to follow the dynamics after arriving at the integrable case. The phase space of the problem contained snapshot tori and a large snapshot chaotic sea at the moment of arriving at zero driving. Afterwards, the phase space pattern was still changing in time, formally a chaotic sea survived, but this change of the pattern was a consequence of the stirring due to the phase space flow of the integrable problem, Fig. 1b. Since the dynamics is regular in the integrable case, even if the snapshot chaotic sea appeared to be extended at any later time, it had no chaotic subset at all.

7. Estimating the dimension of phase space objects

In addition to the famous fractal dimension [104], *fractal distributions* possess a continuous spectrum of dimensions reflecting fractality in different statistical characterizers of the distributions [105–110]. Among these, the so-called *information dimension* is perhaps the most important, because it refers to the most populated subset of the distribution. Furthermore, for natural measures of dynamical systems, it is this dimension which is related to chaos quantifiers, such as average Lyapunov exponents, exemplified by the Kaplan–Yorke [82,111] and Kantz–Grassberger [37,101] formulas. In this section, we give estimates for the dimension based on the previously defined time-dependent quantifiers, and the aforementioned formulas. Since we shall only be dealing with information dimensions, notation D is applied for it (and the subscript 1, often used in the literature, is omitted).

For general parameter drifts, fractality is ill-defined since the (statistical) self similarity of the fractal construction is not ensured due to the perpetual change of parameters. There are indeed examples (see. e.g. [76]), where a numerical scale-dependence of the dimension was found.

It is worth, however, mentioning that there is one subclass of drifting chaotic systems where one can speak of well-defined dimensions: random maps [14,112,113]. We emphasize here that the term random does not necessarily mean stochastic problems. In the context of noiseless systems, the subject of this paper, random maps arise when the time-continuous driving parameters are irregularly changing about a time-independent mean and, importantly, the observation of an ensemble can be arbitrarily long. On a stroboscopic map taken with a pre-selected time T, the dynamics is of the form of (3) in which the parameters μ_n can be written at discrete time n as $\mu_n = \mu_0 + \Delta\mu_n$, where μ_0 is the time-independent mean, and because of the irregular change in continuous time, $\Delta\mu_n$ can be considered a discrete-time random fluctuation. An example of such a process is the advection of floaters on the surface of an irregularly pumped bulk of fluid which was demonstrated, by the experiments of Sommerer and Ott [24,25], to be describable by the theory of random maps. The theory leads to the conclusion that under very general conditions the Kaplan–Yorke relation is valid [114] with the average Lyapunov exponents evaluated in the presence of random fluctuations, and are therefore not the same as in the system without such parameter fluctuations. Analogous statements hold for the Kantz–Grassberger relation [26,37,40,41]. Such results are obtained by averaging over *all* possible realizations of the random fluctuations, i.e. all possible scenarios [14,112,115], possessing different individual dimensions. For sufficiently long times n the deviation is proportional to $1/\sqrt{n}$, implying a rather slow convergence to a well-defined limit. The often used statement, according to which such systems possess a time-independent dimension, should be interpreted in this spirit.

Our approach differs from the one used for random maps in two important ways. For one, we rely on the finiteness of observation windows, and secondly, we do not intend to average over different scenarios. These make the existence of time-independent dimensions impossible in general (even for random maps). Because of this, and the fact that self-similarity is not ensured, here we can only give a heuristic *estimate* for the information dimension. Qualitatively, we believe that such results provide a faithful expression of the fractality observed by naked eye, i.e., on the largest scales.

7.1. Chaotic snapshot attractors

The Kaplan–Yorke formula [82,111] expresses the information dimension D of chaotic attractors with one positive and one negative average Lyapunov exponent. Expressing it in a time-dependent way via relations (25), (31), we obtain

$$D(t) = 2 + \frac{\lambda(t)}{|\lambda'(t)|} = 2 + \frac{\lambda(t)}{\lambda(t)+\sigma} = 2 + \frac{\dot{\rho}(t)}{\dot{\rho}(t)+\sigma}, \tag{47}$$

where the last equation is written to emphasize that the EAPD function determines the full time-dependent information dimension of chaotic snapshot attractors (for a constant σ). This quantity characterizes the attractor in the (x, v, t) three-dimensional phase space and is always smaller than 3. The analogous expression in discrete time is

$$D_n = 1 + \frac{\lambda_n}{|\lambda'_n|} = 1 + \frac{\lambda_n}{\lambda_n + \sigma T} = 1 + \frac{\rho'_n}{\rho'_n + \sigma T}. \tag{48}$$

This formula describes what one sees on the plane of stroboscopic map obtained by taking slices in the three-dimensional phase space at instances nT, $n = 0, 1, 2, \ldots$.

An example for the time-dependent information dimension on the stroboscopic map of the chaotic snapshot attractor of Fig. 6 characterized by the EAPD function of Fig. 11(a) with $\sigma = 2\beta = 0.4$ is given in Fig. 40 in which a decrease of the dimensionality can be observed in the middle of the scenario. This decrease reflects the passing through of a periodic window of the frozen system, resulting in a decrease of the instantaneous Lyapunov exponent there, plotted in Fig. 12.

A simpler case, where the whole investigated time interval can be (roughly) characterized by the same Lyapunov exponent is the chaotic snapshot attractor in Fig. 19 (identical to Fig. 6(b)). Here, using (48) with an approximately constant $\lambda_n \approx 0.91$ (in the interval read off from Fig. 19(d)) and $\sigma = 2\beta = 0.4$, we obtain $D \approx 1.26$. Note that the information dimension in both cases is simultaneously the dimension of the *unstable foliation* since it coincides with the chaotic attractor. The stable foliation is space filling as no other attractors exist.

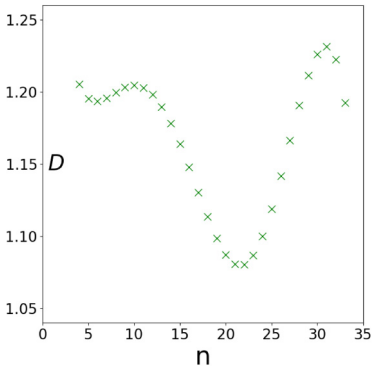

Fig. 40. Time-dependent information dimension of the chaotic snapshot attractor characterized by the Lyapunov exponent presented by the upper curve of Fig. 12.

7.2. Snapshot chaotic saddles, strange snapshot attractors

Since chaos is transient on a strange snapshot attractor, different transient-chaos-related dimensions can be considered in this case. The celebrated Kantz–Grassberger relation [37,101] provides the *information dimension* $D^{(1)}$ *of the chaotic saddle along its unstable direction* in terms of the escape rate and the positive Lyapunov exponent. Writing this in time-dependent form leads to

$$D^{(1)}(t) = 1 - \frac{\kappa(t)}{\lambda(t)} = 1 + \frac{\dot{N}(t)}{N(t)\dot{\rho}(t)}, \quad D_n^{(1)} = 1 - \frac{\kappa_n}{\lambda_n} = 1 + \frac{N_n'}{N_n\rho_n'}, \tag{49}$$

in continuous and discrete time, respectively, where (25) and (40) have been used. This formula suggests that beside the EAPD function ρ, the number of survivors N is another function which is needed to specify time-dependent fractality. Fig. 41a exhibits, with $\sigma = 2\beta = 0.02$, how $D^{(1)}$ changes on the stroboscopic map. Note that the positivity of the metric entropy (41) implies that these dimensions are never negative, that is, the information dimension is only defined for chaotic saddles. For strange nonchaotic saddles, existing for $n > 27$ in Fig. 28(b), the fractal dimension is still positive, while no information dimension exists.

The dimension along the stable direction, denoted by $D^{(2)}$, is $D^{(1)}$ multiplied by the ratio of the positive and the modulus of the negative Lyapunov exponents. In time-dependent forms

$$D^{(2)}(t) = \frac{\lambda(t)}{|\lambda'(t)|}D^{(1)}(t) = \frac{\lambda(t)}{\lambda(t)+\sigma}D^{(1)}(t), \quad D_n^{(2)} = \frac{\lambda_n}{|\lambda_n'|}D_n^{(1)} = \frac{\lambda_n}{\lambda_n+\sigma T}D_n^{(1)}. \tag{50}$$

Quantities $D^{(1)}, D^{(2)}$ are partial dimensions, always smaller than 1. Other relevant dimensions can be obtained via elementary modifications. The dimension of the saddle on the stroboscopic map is simply the sum $D_n^{(S)} = D_n^{(1)} + D_n^{(2)}$. Adding just 1 to the partial dimensions provides the dimensions of the stable and unstable manifold (coinciding with the foliations): $D_n^{(s)} = 1 + D_n^{(1)}$, $D_n^{(u)} = 1 + D_n^{(2)}$. The dimensions in the (x, v, t) phase space are $D^{(S)}(t) = 1 + D^{(1)}(t) + D^{(2)}(t)$ for the saddle, and $D^{(s)} = 2 + D^{(1)}(t)$ for the stable and $D^{(u)} = 2 + D^{(2)}(t)$ for the unstable manifold/foliation, respectively. These expressions clearly indicate that taking a slice of the phase space objects of the full phase space decreases the dimensionality by 1.

We write out these dimensions explicitly, with $\lambda(t) = \dot{\rho}(t)$ and $\lambda_n = \rho_n'$,

$$D^{(u)}(t) = 2 + \frac{\dot{\rho}(t)}{\dot{\rho}(t)+\sigma}\left(1 + \frac{\dot{N}(t)}{N(t)\dot{\rho}(t)}\right), \quad D_n^{(u)} = 1 + \frac{\rho_n'}{\rho_n'+\sigma T}\left(1 + \frac{N_n'}{N_n\rho_n'}\right), \tag{51}$$

and

$$D^{(s)}(t) = 3 + \frac{\dot{N}(t)}{N(t)\dot{\rho}(t)}, \quad D_n^{(s)} = 2 + \frac{N_n'}{N_n\rho_n'}, \tag{52}$$

The former is the *information dimension of the unstable manifold of the chaotic saddle* in continuous time and on the stroboscopic map, respectively. However, we have seen that the unstable manifold of the saddle embedded into the strange snapshot attractor is the same as the unstable foliation, while the latter is nothing but the strange snapshot attractor itself. This means that, quite remarkably, even if the origin of the fractality in (51) is transient chaos, *this dimension is the dimension of an attractor*, namely the strange snapshot attractor. An example is plotted in Fig. 23(a) for $n = 25$, along with the chaotic set governing the dynamics of this attractor, the snapshot chaotic saddle in Fig. 23(d). Fig. 41(b) exhibits the dimension of the unstable manifold as a function of discrete time n, while 41(a) displays the

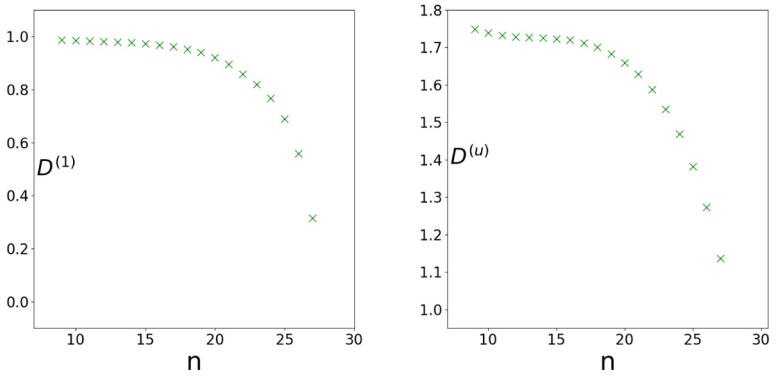

Fig. 41. Time-dependent dimensions related to strange snapshot attractors determined based on the number of survivors function of Fig. 28(a) and the EAPD function of Fig. 24(a). (a) Information dimension of the saddle along its unstable direction. (b) Information dimension of the unstable manifold/foliation which coincides with that of the attractor. The points are plotted until $n = 27$ only, because after this, κ_n is larger than the value of the Lyapunov-exponent, i.e. the snapshot chaotic saddle is replaced by a strange non-chaotic saddle.

dimension along the unstable direction. From panel (b) we can read off that the dimension of the strange snapshot attractor displayed in Fig. 23(a) is $D^{(u)}_{n=25} \approx 1.39$. Note that dimension $D^{(u)}_n$ originates in the chaotic part of the strange snapshot attractor, as in the parts spiraling around the SNPs the foliation is one-dimensional, the local Lyapunov exponent is expected to be negative. It is nevertheless correct to say that $D^{(u)}_n$ (as long as it is larger than 1) is the dimension of the full attractor since the dimension of the union of two sets (in this case the chaotic and spiraling parts) is the larger dimension of the sets.

Eq. (52) describes the *information dimension of the stable manifold of the chaotic saddle*. The time-dependence of this dimension can be obtained by just adding 1 to the points in Fig. 41(a), the dimension along the unstable direction, and characterizes the fractality of basin boundaries. In the particular case of Fig. 27(a), its value is $D^{(s)}_{n=25} \approx 1.68$. From the dimensions of the two manifolds, we have, for the snapshot chaotic saddle of Fig. 23(d), $D^{(S)}_{n=25} = D^{(s)}_{n=25} + D^{(u)}_{n=25} - 2 \approx 1.07$.

7.3. Hamiltonian snapshot chaotic saddles

A peculiar feature of snapshot chaotic seas is that they are not necessarily fully chaotic. We have seen that the Hamiltonian chaotic saddle is often a subset of the chaotic sea which also contains non-chaotic regions. It is thus a non-trivial question to ask whether, contrary to the traditional case, the dimension of the chaotic subset is different from the dimension of the phase space. Because of the existence of the non-chaotic regions, the saddle might be considered as a set governing the temporarily chaotic motion between incoming typically non-chaotic and outgoing non-chaotic dynamics. We can thus say that the process is a kind of *chaotic scattering* [82,86] in a system of *bounded phase space*. The analogy is valid since in traditional chaotic scattering both the incoming and outgoing motion is a free flight stretching to infinity, a special case of non-chaotic dynamics.

It is therefore meaningful to estimate the dimension of Hamiltonian snapshot chaotic saddles. Technically, the formulas follow from those of the previous subsection, just the phase space contraction rate σ should be set zero. From (51) we have for the dimension of the unstable manifold/foliation in continuous time and on the stroboscopic map:

$$D^{(u)}(t) = 3 - \frac{\kappa(t)}{\lambda(t)} = 3 + \frac{\dot{N}(t)}{N(t)\dot{\rho}(t)}, \qquad D^{(u)}_n = 2 - \frac{\kappa_n}{\lambda_n} = 2 + \frac{N'_n}{N_n \rho'_n}. \tag{53}$$

A peculiar feature following from the non-dissipative character is that the these expressions also hold for the stable manifold/foliation since for $\sigma = 0$ the partial dimensions are identical $D^{(1)} = D^{(2)}$ both in continuous and discrete time.

We apply these results to the scenario investigated in Section 6.4 since it is interesting to see the approach to the limit of integrability in terms of dimensionality. Based on the results given in Fig. 38 and relation (53) the time-dependent dimension of the foliations is determined and plotted in Fig. 42. One sees a quick initial increase and a saturation at dimensionality 2 after about $n = 22$, that is, the information dimension differs from the dimension of the phase space in the initial phase of the process only. This is in harmony with the discussion at the end of Section 6.4 according to which the set in Figs. 38(a) and 38(b) refer asymptotically to the non-hyperbolic component. It is thus natural to interpret the results as the non-hyperbolic component tending to be space-filling in the limit of integrability. A similar behavior is expected in the dimensionality of the non-chaotic component of the entire chaotic sea.

It is worth mentioning that non-chaotic regions might be part of snapshot chaotic seas in chaos enhancing scenarios, as well. An example is shown in Fig. 34 where the red non-chaotic region was shown to decrease with n. A similar dimension

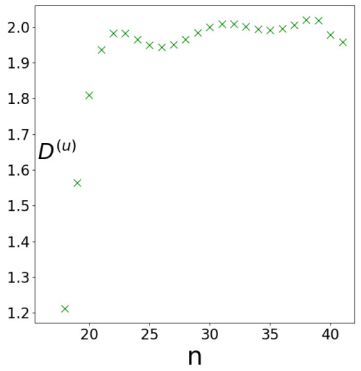

Fig. 42. Dimension of the unstable foliation (based on Fig. 38), which coincides with that of the stable foliation in this case, as a function of discrete time. The behavior is dominated by the non-hyperbolic component.

analysis would lead in that case, too, to an increasing dimensionality of the foliations, and a saturation at 2, the dimension of the phase space, if the escape rate vanishes. This is, however, a physically completely different situation from the one characterized by Fig. 42, since the data would reflect the unstable manifold of the chaotic saddle, and illustrate that the foliations and the chaotic saddle can become space-filling as time goes on. This is also the reason why that analysis would be more difficult to carry out: the area from which escape should be monitored is basically the chaotic subset of the snapshot chaotic sea, which, besides changing in time, has a very complicated shape.

8. Relevant aspects in dynamical systems theory

8.1. Other types of typical parameter drifts and scenarios

It is to be emphasized that the features discussed above hold for any type of parameter drift of any parameter. For example, the case of a quadratic drift is treated in the Appendix, and in Section 9.5 a Duffing case will be discussed with a linear trend in the driving frequency.

Fig. 43 provides a schematic summary of basic types of typical scenarios in terms of a general parameter μ, used in (1). Panel (a) represents the most straightforward generalization of the linear time-dependence followed up to now into a monotonic increasing (or decreasing) trend during the time window of observation.

Another type of time-dependence can be an aperiodic up and down change in the drifting parameter restricted to a bounded range, as illustrated by panel (b). This might be realistic, say, when modeling wind strength in environmental problems (see e.g. [84]). The theory of random maps mentioned in Section 7 is applicable to this type of scenario, however, only if there is no restriction on the length of the observation time window. A combination of type (a) and (b) is also possible, when oscillations occur about a monotonically changing curve.

Panel (c) represents a scenario bridging two constant values of the parameter. In dissipative cases, a simplifying feature here is that on the plateaus traditional attractors exist, even if the time of observation does not necessarily allow for a full convergence. If, in addition, the plateaus are allowed to be infinitely long, even $t \to \pm\infty$ limits can be properly

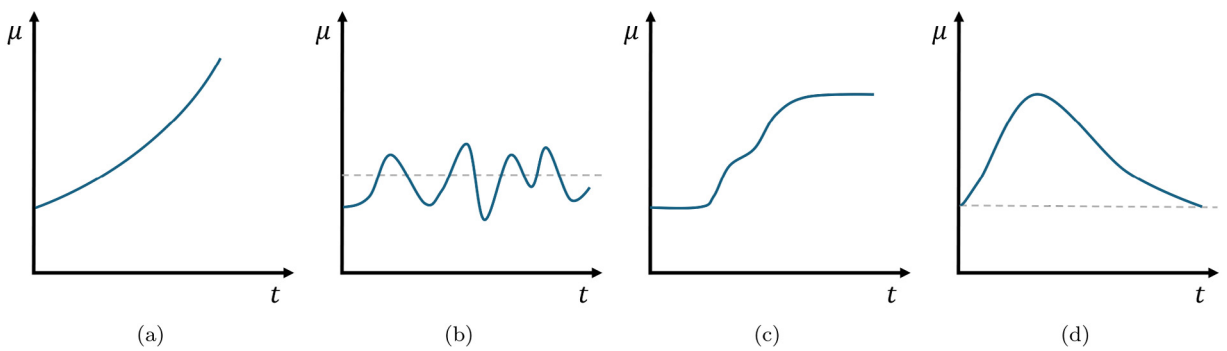

Fig. 43. Scenario types: (a) monotonic change, (b) aperiodic oscillations about a mean (dashed line), (c) crossover between two parameter plateaus, (d) return scenario to the initial level (denoted by a dashed line). All scenarios are drawn in the time window of observation, i.e. between $t = 0$ and $t = t_{max}$.

defined. In any case, phase space objects in scenario segments away from the plateaus can only be *snapshot* objects. The use of such plateau-scenarios (with infinitely long plateaus) is typical in the field of *rate induced tipping*. The literature, see e.g. [58,67–69], investigates if in a drifting system a qualitatively *different* attractor can be reached due to the drift, if the rate is sufficiently large. In the simplest settings, a crossover from a point attractor, or SNP, to another one occurs across a moving hyperbolic state, an SHP. We note here that the study of rate induced tippings has been extended from regular systems to tippings over snapshot chaotic saddles [52,53,116]. In this paper, we illustrated rate induced tippings from regular to chaotic dynamics in the context of snapshot attractors and the break-up of snapshot tori, in Sections 3.5 and 6.1, completing the picture by adding the issue of adiabaticity.

Panel (d) illustrates a scenario type in which a full return to the initial parameter $\mu(0)$ occurs at some later time. Such a scenario is particularly well suited for illustrating the difference between the drifting and the frozen dynamics since with drifting a *hysteresis* is present: the initial and the final states are *different*, although the parameter itself has returned to the same value.

The easiest way to illustrate the hysteresis is to consider the linear problem formulated for snapshot points in Section 2. Consider a piecewise linear version of Fig. 43(d) with driving amplitude $\mu(t) = \varepsilon(t) = \varepsilon_0 + \alpha t$ with $\alpha > 0$ valid from $t = 0$ up to some $t = t_1$, when the sign of the first derivative suddenly changes, and

$$\mu(t > t_1) = \varepsilon(t > t_1) = \varepsilon_0 + \alpha(2t_1 - t) \quad \text{for} \quad t_1 \le t \le 2t_1, \tag{54}$$

so that the amplitude is ε_0 again at $t = 2t_1$. Now the parameter drift is continuous at $t = t_1$, but there is a jump in the derivative, and hence also in the graph of the position of the snapshot point $y^*(t)$. Based on (12), for $t > t_1$ the expression of $y^*(t)$ is also of the form of (12) (the coefficients are given in the Appendix):

$$y^*(t > t_1) = a_0\big[\varepsilon_0 + \alpha(2t_1 - t)\big]\cos\omega t + b_0\big[\varepsilon_0 + \alpha(2t_1 - t)\big]\sin\omega t - a_1\alpha\cos\omega t - b_1\alpha\sin\omega t \quad \text{for} \quad t_1 \le t \le 2t_1. \tag{55}$$

By time $t = 2t_1$, the solution $y^*(2t_1)$ is different form $y^*(0)$ given by (12) at $t = 0$. The difference $\Delta y^* = y^*(0) - y^*(2t_1)$ has a particularly simple form when t_1 is an integer multiple, say n_1, of the driving period $T = 2\pi/\omega$ implying $\cos(\omega 2t_1) = 1$, and $\sin(\omega 2t_1) = 0$. We can then follow the process in stroboscopic instances. The coordinate of the snapshot point is given by y_n^* in (17) along the increasing ramp up to $n = n_1$. In the decreasing phase the y^* coordinates follow from (55) to be

$$y_n^* = a_0\varepsilon_{n>n_1} - a_1\alpha = a_0\big[\varepsilon_0 + \alpha(2n_1 - n)T\big] - a_1\alpha, \quad n_1 \le n \le 2n_1. \tag{56}$$

Plotting the coordinates as a function of the corresponding driving amplitude, i.e. eliminating n, a "hysteresis loop" is found on the ε, y^* plane, consisting of two parallel lines of discrete points, vertically shifted by

$$\Delta y^* = 2\alpha a_1. \tag{57}$$

The height Δy^* of the hysteresis loop is set by the *rate* of the parameter drift. The hysteresis disappears only for the frozen system without any drift.

It is common to speak about hystereses in relation to attractors, and such dynamical hystereses were found in ensemble averages of chaotic snapshot attractors, see e.g. [32,38,47,117,118]. Our simple analysis is, however valid for any snapshot points, and this suggests that the hysteresis phenomenon can be present in the dynamics of *any kind* of snapshot objects. Examples for snapshot torus hysteresis was given in [36], as well as in Supplementary Material S6 of [35].

8.2. Undriven non-autonomous Hamiltonian systems

Throughout this paper, we have been focusing on *driven* dynamical systems, where the proper characterization of the phase space can be achieved through a stroboscopic mapping. Although the most general features of chaotic systems subjected to parameter drift can certainly be inferred from these, we have yet to touch on an important class of chaotic dynamical systems: *undriven*, closed Hamiltonian systems. In the time-independent case, they possess an even-dimensional phase space, which can be reduced by considering a Poincaré section. Here, one of the coordinates is fixed while another one can be expressed from energy conservation. Countless examples of such two-dimensional, simple systems exist, for example the double and spring pendula, or masses swinging on a pulley [82,86], all with air drag neglected.

The non-autonomous version of this type of systems is still yet to be properly analyzed and described. Nevertheless, we can formulate some expectations about these, based on what we know so far. One coordinate of the phase space can be eliminated by a Poincaré section, however the energy is no longer conserved since its expression becomes explicitly time-dependent. This means that only one dimension can be reduced, leaving us, in the case of planar motion, with a three-dimensional phase space of the map. The mapping connects points of the same Poincaré section but of different flying times. In the presence of parameter drift, a new feature is that the distribution of the flying times over the section is in itself *time-dependent*. We expect that the objects in this phase space behave similarly to those we encountered so far: some initial ensembles represent regular, while some others chaotic motion, and these objects change their shape in time, with a chance for predictable motion to turn into chaotic via a break-up process of snapshot tori in a scenario. Snapshot tori are defined, as in all cases up to now, as images of tori on the Poincaré plane of the frozen Hamiltonian system, followed in a dynamics subjected to parameter drift. These tori remain one-dimensional objects which are able to

deform in the third dimension, and their convenient monitoring occurs in a projection on a 2-dimensional plane, where different tori might intersect. In a different view, snapshot stable and unstable foliations, as well as chaotic saddles should also exist in these systems, and we expect these to generally behave similarly to the ones studied in this paper, only living in a four dimensional phase space. We also expect the EAPD to work the same way, and we expect it to be an accurate indicator of chaos here as well.

8.3. Doubly transient chaos

An other type of system that provides a peculiar class of chaotic dynamics is that of undriven autonomous dissipative systems. They generally exhibit complex time-dependence, and are often used as experimental demonstrations of chaos, as e.g. the double pendulum (with air drag being relevant). This is, however, misleading since permanent chaos certainly cannot be present in such systems. Due to friction being present, the intensity of such motions decreases in time, along with a monotonous decrease of the total mechanical energy: the final state is a rest state, the attractor can only be of fixed point type. Transiently chaotic dynamics could, in principle, govern such systems due to a usual chaotic saddle, but its existence requires the presence of unstable periodic orbits of infinite lifetime, and friction excludes the existence of such orbits. Chaotic dynamics is thus not only transient, but also time-dependent in such a way that it ceases to exist ultimately. The term doubly transient chaos was introduced in [76] as a proper term for chaos that undriven autonomous dissipative systems exhibit.

The properties of such systems were investigated in the examples (all in the presence of dissipation) of the two- and three-magnet magnetic pendula [45,76,119], of the motion of a ball in a bowl [120,121], of a roulette [122], of the double pendulum and of a ball bouncing between two wedges [119]. As particular consequences of the perpetual decay, a time-dependent escape rate $\kappa(t)$ was defined to characterize the escape form chaos towards the state of rest and found to exhibit a strongly increasing trend [76]. Fractal-looking basin boundaries turned out to exhibit smaller and smaller fractal dimensions when observed with increasing magnifications [76,119–122].

The usefulness of an ensemble view in the context of doubly transient chaos was explored in [45,119] leading to the conclusion that a clear view is provided if one identifies first the basic phase space structures of the dissipation-free, Hamiltonian version of the problem. Particle ensembles can be initiated on KAM tori or on chaotic regions on the initial (frozen) Poincaré plane, and their time evolution is followed with dissipation turned on. Although there is no driving here whose amplitude would be subject to parameter drift, *the total energy is time-dependent (is monotonically decreasing), and can be considered a drifting parameter (of negative rate)*. Thus, all the techniques used in the paper apply here as well. An ensemble initiated on a frozen KAM torus might exhibit torus break-up, despite the chaos weakening scenario. The minimal phase space dimension for autonomous chaos in the presence of dissipation is 4, thus after applying a Poincaré section, the phase space is 3-dimensional and cannot be reduced further due to the lack of energy conservation, just like in the case of undriven non-autonomous Hamiltonian systems. Snapshot tori thus exist in a 3-dimensional space, and can be monitored on a 2-dimensional projection. Nevertheless, the break-up can clearly be followed [45,119], and it is interesting to observe that tori dissolve into chaos well before all motion stops. An ensemble initiated on a chaotic sea of the Hamiltonian counterpart evolves as a snapshot chaotic sea which is defined as earlier, i.e. the image of the Hamiltonian chaotic sea, but evaluated in the dissipative dynamics. At first it might grow, but asymptotically it always decreases in extension, and shrinks, ultimately, onto the fixed point attractor. Note that the term snapshot chaotic sea characterizes in this case a *dissipative* system. It can again be seen that even if such a sea appears on the map as an extended set of points, its chaoticity might be rather weak. In fact, the EAPD curve can be evaluated in such cases both for tori and chaotic seas, and one finds an initial strong increase in both cases, followed by reaching a maximum, after which a decrease towards large negative values can be seen [45,119].

Recently the concept of doubly transient chaos has been extended to *open* systems [123]. The analog of transient chaos in autonomous Hamiltonian systems of unbounded phase spaces is traditional chaotic scattering [37,124], as also mentioned in relation to the dimension of Hamiltonian snapshot chaotic saddles in Section 7.3. Such processes start with an incoming free motion which becomes convoluted in the central scattering regions, and ends with a free outgoing motion. The term used in [123] is dissipative chaotic scattering, and the aim is to understand the effect of dissipation on the scattering dynamics. Besides mechanical friction, dissipation can play an important role even in astronomy where radiation pressure might break the motion [125]. Dissipation was found to alter the escape rate since the perpetual energy decay implies that the particle motion is slowing down. It also affects the nonhyperbolic behavior: dissipation typically destroys elliptic orbits and the surrounding KAM tori. The authors of [123] apply an ensemble view, start with an extended initial distribution, and investigate the survival probability in a phase space region. In contrast to usual chaotic scattering, the initialization is not in the incoming region of free motion, rather in a central part of the potential, in the scattering region, since otherwise dissipation might hinder the arrival to this region. The survival probability $P(t)$ of trajectories within the scattering region is shown to decay ever slower: the escape rate $\kappa(t)$ decreases in time. The decrease is due to the fact that the typical energy of particles is decaying in time and the escape rate of the dissipation-free Hamiltonian system is smaller at lower energies. The authors suggest to define a sub-ensemble by selecting particles of the full ensemble possessing a particular energy value E, one of the values accessible in the Hamiltonian counterpart. This can be done because they use small dissipation. The authors find that particles of instantaneous energy E are distributed along a fractal-like filamentation. Furthermore, this filamentation is practically the same as the unstable manifold of the chaotic saddle governing the scattering in the dissipation-free scattering process at fixed energy E. This implies that dissipation enhances trapping, and certain aspects of the process can be approximated via properties of the Hamiltonian counterpart, in the case of small dissipation.

9. Potential applications

9.1. Climate science

The dynamics of the climate can be called chaotic-like as it is certainly a complex dynamics exhibiting complicated time-dependencies. A climate model has $10^6 - 10^9$ different variables, the dynamics is thus describable by Eq. (1) with a very high-dimensional vector **x**, and, in addition, it also governs important spatial aspects related to a hierarchy of relevant time-scales. These differences motivate us not to call climate simply chaotic, rather chaotic-like. An important common feature with low-dimensional chaos is certainly unpredictability. Climate dynamics could also be called turbulent, or considered an example of spatio-temporal chaos, in our current context it is, however, worth concentrating on similarities with usual chaotic dynamics.

Due to the frictional forces, present in the atmosphere and oceans, climate dynamics is dissipative, and possesses an attractor. Even in an unchanging climate, this attractor is high-dimensional and complex. Its fractal character cannot be unfolded since only projections can be observed (and the projection of a high-dimensional fractal on low-dimensional spaces is space-filling). The attractor of an unchanging climate represents the set of all states permitted to coexist, and it has a natural periodicity due to seasonal changes.

The main reason of the climate change occurring in our days is considered to be the observed increase of greenhouse gas concentrations, in particular that of the well-measurable carbon dioxide on the scale of a century, while other (e.g. geophysical) factors like the total solar irradiation might play a smaller role [126]. This change in CO_2 concentration represents a kind of external driving, $\mu(t)$ in Eq. (1), whose amplitude increases in time, with a scenario similar to the schematics of Fig. 43(a). In a qualitative comparison with Eq. (4), the time-dependence of the concentrations of greenhouse gases is the analog of the driving amplitude $\varepsilon(t)$ with a positive rate α (and ω corresponds to the frequency of the annual periodicity). As this analogy also shows, our changing climate is a system subjected to parameter drift. Since the driving contains a nonperiodic component, too, there is no strict repetition, and the climate attractor is strictly aperiodic. It is in fact a high-dimensional snapshot attractor, that can be considered to be representing the plethora of all permitted climate histories (after convergence to this attractor took place). As in low-dimensional cases, a proper representation of the snapshot attractor requires ensemble simulations. By now, an increasing number of ensemble simulations are available in climate science, and the ones corresponding to what we have discussed up to now use a single climate model with a chosen forcing (e.g. greenhouse gas concentration) scenario, and run with an ensemble of initial conditions without any change in the model and in the scenario (see e.g. [127–130]). A qualitative term characterizing this approach is the "theory of parallel climate realizations" [32–34]. A very important message of ensemble simulations is that a statistical characterization of the climate can only be given in terms of instantaneous quantities, one cannot rely on the temporal (e.g. 30-year) averages widely applied in earlier approaches.

A well-spread visualization method of the snapshot attractor in climate science is showing the projection of a *single* global variable, e.g. the annual mean surface temperature, as a function of time. As ensemble results are presented, a band of data appears at any instant (in any year), the permitted values of all the parallel climate realizations.

As an example, Fig. 44 presents the projection of the high-dimensional snapshot attractor on the global mean surface temperature variable, denoted here as TS, in the last 100 years, using the CO_2 scenario based on the measured data. One

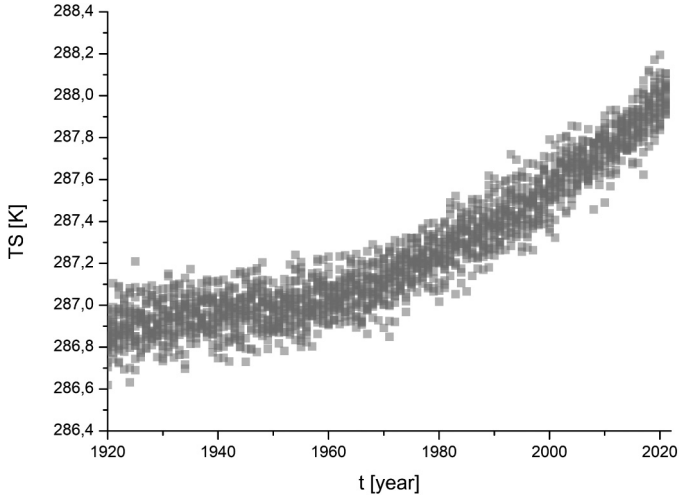

Fig. 44. Projection of the climate snapshot attractor on the annual global mean surface temperature (TS) variable in a climate ensemble simulation (gray shading) in the period 1920–2020. The simulation was performed with a freely accessible intermediate complexity model, the Planet Simulator [131] with a 20-member ensemble. Data by M. Herein, used with permission.

clearly sees an increasing trend, in particular after 1960, a visualization of what is called global warming in plain language. The width of the gray band is the size of the snapshot attractor in this variable.

The very high dimensionality of the climate attractor severely limits the illustration of the methods presented in this paper for dissipative systems, since neither foliations nor chaotic saddles can be sufficiently visualized. There is however one method that could be viable even in this case: the EAPD. It speaks to the universality of the EAPD method that it can indeed be measured in any projection of the phase space as it is only about the strongest separation rate between initially close trajectories. In practice, however, a recent study shows [132] that the time scale of separation in a climate model is about a month, since after this the distances do not grow further considerably. This means that, especially compared to the time scale of a few hundred years of climate models, one measurement of the EAPD is expected to characterize the system on *meteorological* time scales. This approach does have potential, however, since meteorological prediction times are, for obvious reasons, of interest, for which the reciprocal of the (meteorological) instantaneous largest Lyapunov exponent might be a natural candidate. At the same time, characterizing the long-term climate can still be possible using the EAPD. For this, repeated measurements have to be taken in subsequent years, similarly to the method described in [132]. In this way, one could obtain the long-term time-dependence of the instantaneous Lyapunov-exponent in a climate model.

Before the now more widely accepted practice of ensemble simulations, climate predictions have largely been based on single simulations, however, it follows from the overall approach presented here that these cannot be considered reliable. These days, some of the professional models using ensemble simulations yield results that turn out to be in harmony with observations of the recent past in global quantities at least, like temperature TS in Fig. 44, see e.g. [3,4,127,130,133]. (It has to be noted that due to the overwhelming numerical demand of state-of-the-art climate models, an ensemble is considered large, if the number of ensemble members is a few times 10 [134,135].) However, it is worth emphasizing that even with ensemble simulations, there can be a problem if no care is taken of the convergence time t_c to the attractor. There is a considerable literature dealing with this aspect [32,93,136,137]. The convergence time in processes influenced mainly by the atmosphere is estimated to be a few decades, and for the ocean it can be hundreds of years. If ensemble simulation results are taken for time instances earlier then t_c after initialization, they do not characterize the climate since initial condition chosen in the numerics are not yet forgotten, see relation (36). In this spirit, the simulation of the ensemble presented in Fig. 44 was initiated in 1850 (with an already converged ocean), so it is fair to say that in the displayed time interval the data represent the climate attractor.

We mention in brief that tipping transitions are essential also in climatic contexts, and illustrate this with a few examples. Rate induced tipping was identified in [138] in a wind-driven ocean model between a basic state and a self-sustained periodic regime due to the drift in the external forcing. The unstable state across which tipping occurs in large climate models is a high-dimensional chaotic saddle. The terminology of the literature on turbulence in pipe flows was taken over, and such a state is called an *edge state* [139], if governed by a saddle whose stable manifold cuts the phase space into two. In the problem of the Snowball Earth-Warm Earth transition, taking place due to a change in the solar irradiation intensity, tipping is on the boundary between these stationary states as investigated in detail in [140]. In a subsequent study [141] with a return scenario, long term tipping or no tipping was found to occur with certain probabilities which can be determined via ensemble simulations.

A feature of the climate certainly not present in low dimensional models, is spatial aspects. The many temporal scales combined with spatial ones lead to the striking phenomenon of teleconnections, i.e. pronounced correlations or anticorrelations in the behavior of remote geographical locations. These are subject to alterations due to climate change. Their investigation from the point of view of snapshot attractors has started in [32]. As an example, we mention here the case of the perhaps best known teleconnection, the El Niño Southern Oscillation (or ENSO) phenomenon, see e.g. [74,142–145]. A particularly efficient method of pattern analysis is the search for Empirical Orthogonal Functions (EOFs). In relation to teleconnections, their generalization to ensemble approaches has been worked out by Haszpra and coworkers [146] in the framework in which temporal averages are replaced by averages taken with respect to the natural measure on the snapshot attractor, the method is therefore called the *snapshot EOF*, SEOF analysis [145–148]. To our knowledge, in physics research the focus is not yet on pattern forming systems subjected to parameter drift. Examples could be partial differential equations or cellular map lattices with changing parameters, or turbulent flows of increasing or decreasing intensity. In any case, the methods developed in climate science could be worth taking over, such as teleconnection analysis and in particular, the SEOF method.

An important issue has not been discussed in the paper, namely extreme behavior. The study of extreme events is a hot topic in climate science and in environmental problems, see e.g. [149–152]. In view of the need of an ensemble approach for drifting systems, very little is known about how to study the dynamics of extremes in such cases. In a climatic concept, an example is provided in [132] where the typical growth rate of extremes was studied. On the ensemble representing the snapshot attractor, sub-ensembles were considered originating from well localized initial distributions at a given instant, enabling one to "zoom in" into the dynamics of the system. Out of these sub-ensembles plume diagrams evolve (similar to that of Fig. 6(a)), and the difference between the maximum and minimum values of a quantity in such a plume diagram was considered an extreme deviation, followed in time. The dynamics of typical extreme deviations is then obtained by averaging over all sub-ensembles on the attractor. The application of this method might be promising in low-dimensional systems, too.

Concerning *experiments* related to climate change, the first and only example we are aware of is that of Vincze and co-workers [153]. The authors followed a traditional setup for modeling large scale flows on Earth, and used a rotating

annulus filled with water subjected to a horizontal temperature gradient, mimicking the temperature contrast between the Equator and one of the Poles. The novelty of the experimental procedure was that the temperature contrast *decreased* in time continuously, and that the surface temperature was measured (via a thermographic camera) in an *ensemble* of experiments driven with a practically identical decay in the temperature contrast in all cases. Mean and variance of the surface temperature field was evaluated over the ensemble. We would like to emphasize that the experimental investigation of any system subjected to non-adiabatic drifts would require similar ensemble experiments.

9.2. Lagrangian coherent structures

The problem of advection is of central importance in environmental science. May the advected particle be harmful (like e.g. pollution) or beneficial (like e.g. plankton for fishes) the advection dynamics for small sized particles (whose extent is much smaller than the characteristic size of the flow) is described by the equation

$$\dot{\mathbf{r}} = \mathbf{v}(\mathbf{r}, t), \tag{58}$$

where $\mathbf{v}$ is the space and time-dependent velocity field whose form is assumed to be known, and is typically incompressible:

$$\mathrm{div}\mathbf{v} = 0. \tag{59}$$

Position $\mathbf{r}$ represents not only the spatial coordinate, but also the position of the advected particle. The content of (58) is thus that the particle takes on the velocity of the neighboring fluid immediately, a natural assumption for small particles. Eq. (58) is a set of three first order differential equations, the phase space is thus identical with the geometrical space. Its solution in the Lagrangian view, the particle path $\mathbf{r}(t)$, is typically chaotic [154,155]. Due to the incompressibility condition (59) the dynamics is volume-preserving, and in the special case of two-dimensional advection, it can be transformed into a Hamiltonian form [37].

The time-dependence of velocity fields in nature is aperiodic: winds and oceanic currents often change strength and direction, although the magnitude of these is typically bounded. The parameter drift in this context is thus not monotonic, rather oscillatory in a nonperiodic manner, similarly to the schematics of Fig. 43(b). The topic of chaotic advection in flows of arbitrary time-dependence and over finite-time intervals attracted intense scientific interest in the last two decades (see e.g. [156,157].) The appearance of the concept of Lagrangian Coherent Structures (LCSs) [5–13] implied a kind of breakthrough. These are material objects, formed by fluid elements, that organize transport over finite time intervals, that is they separate different types of fluid motion. LCSs are thus transport barriers in problems appearing in the context of advection.

Hyperbolic LCSs are defined as surfaces (ridges) along which the stretching of fluid elements is maximal, and turn out to exhibit filamentary patterns. Material surfaces of large future stretching can be called stable manifolds, namely manifolds of certain hyperbolic cores. Similarly, material surfaces of large past stretching are typically considered as unstable manifolds of certain hyperbolic cores. We point out that the hyperbolic cores correspond to snapshot hyperbolic points (SHPs) in our terminology, and that *hyperbolic LCSs run parallel to the stable and unstable foliations of the dynamical system* (58). The LCSs are in fact subsets of the foliations, since the latters are not subject to any global maximizing condition.

Elliptic LCSs are closed surfaces along which shear is maximal, and their outermost element encircle long-lived *vortices*. The general property of LCSs, being barriers to transport, is particularly well manifested here: an elliptic LCS is a compact (rotating) surface that keeps material trapped, fluid elements inside it cannot escape. The outermost elliptic LCS corresponds to the vortex boundary, and this closed material surface remains smooth during the time of observation [158]. Interpreting this in view of the torus break-up phenomenon discussed in Section 6.1, we can say that in two-dimensional flows *elliptic LCSs are bounded by the outermost snapshot tori not yet broken up in the interval of observation*. In other words, the surrounding stable foliation has not yet entered the snapshot torus representing the vortex boundary. A visualization of this connection was shown in [35] using the so-called Polar Rotation Angle method [159].

The observation of [158] according to which three-dimensional time-dependent elliptic LCS-es, vortices, are rotating, material-holding tubular regions of the flow, can be illustrated via a set of simple laboratory experiments. The authors of [160,161] used magnetic stirrers to generate a rotating water column in a cylindrical container. The vertical rotational axis of the stirrer bar, brought into motion via a magnet rotating below the bottom of the container, is not fixed, rather is irregularly oscillating about a mean position. Consequently, the fluid is also brought into rotation but the emerging vortex is not stationary, it is time-dependent in an aperiodic manner. When injecting dye into the central region of the container, one finds that the dye remains captured around a central tubulus as shown in panel (a) of Fig. 45 over long stretches of time (over minutes in the experiment). This observation can be interpreted by having visualized a moving vortex, which turns out to be much narrower than the full rotating fluid. The central feature of a vortex is not its rotation, rather its material holding property [158]. In harmony with this, if a certain amount of dye enters a region outside the vortex, it becomes rapidly diluted. Figs. 45(b) and 45(c) illustrate this process. Here, injection occurs close to the vortex, and dye remains initially close to it (panel b). A short while later (on the time scale of a few seconds) dilution occurs, and a uniform mixing takes place (panel c), leading to a complete homogenization outside the vortex. What occurs in any horizontal slice can be interpreted by saying that the vortex is analogous to an island of yet unbroken snapshot tori,

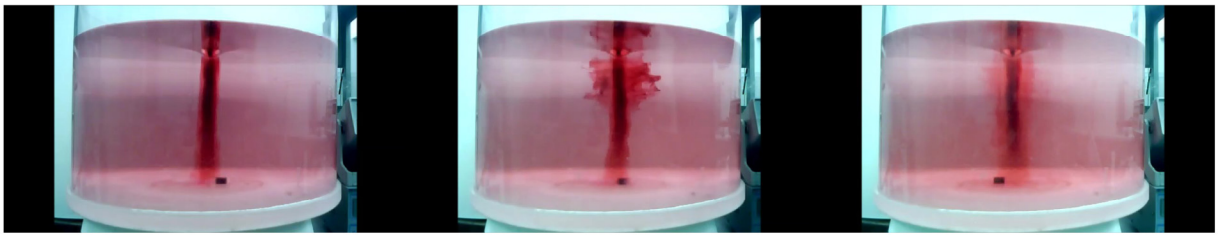

Fig. 45. Snapshots from a video recording of an experiment conducted by the authors of [160,161]. Panel (a): dye is injected in the central region from above and spreads along a column of approximately constant width, a vortex. Panel (b): dye injected outside the vortex might remain initially close to it but later, panel (c), becomes spread in an extended region. The short black segment at the bottom designates one end of the rotating stirrer bar. The images are snapshots from a video made by M. Vincze, used with permission.

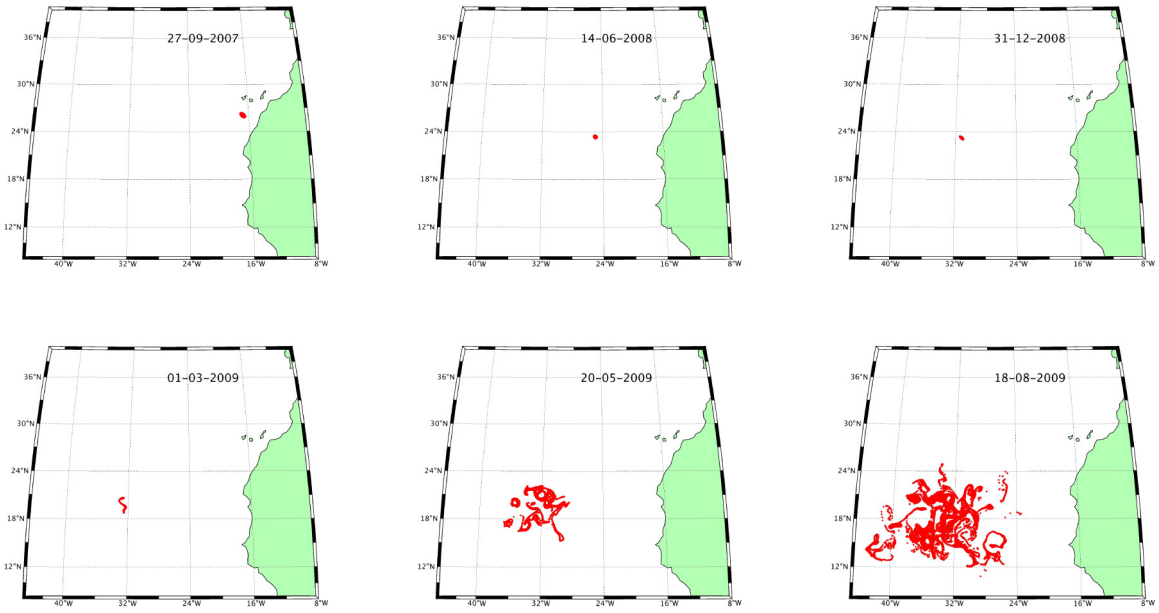

Fig. 46. Numerical monitoring of the material content (red) of an elliptic LCS identified off the Canary Islands in September 2007 ending in a break-up process which start on the 1st of March 2009. This break-up process is very similar to the break-up of snapshot tori presented in Section 3.1. The images are snapshots from the Supplementary Movie "M11" from the PhD thesis of Anass El-Aouni [165], used with permission.

and material entering the fluid outside this island enters the snapshot chaotic sea and becomes mixed accordingly. The analogy with snapshot tori is supported by the fact that the rotation of the fluid is aperiodically time-dependent, and that after sufficiently long times even the dye in the vortex mixes into the surrounding fluid, an analogous process to the torus break-up.

Concerning environmental flows in nature, elliptic LCSs also arise, among others, in the context of coastal upwellings, a well studied case of which is, e.g., the North-West African upwelling with characteristic mesoscale eddies [162–164]. As an example, we show in Fig. 46 the time-evolution of an elliptic LCS in this region [165]. A coherent vortex of 38 km in diameter was formed off the Canary Islands. Its material content is colored red, and as the pictures resulting from a numerical simulation based on the observed flow show this elliptic LCS kept its identity over about 450 days. Then it lost the compact form, broke up, similarly to the snapshot torus of Fig. 7, and became quickly stretched into an extended and convoluted filamentary structure, the unstable foliation of the fluid flow at that instant. Again we can establish an analogy between elliptic LCSs and snapshot tori.

9.3. Galaxy dynamics

Modern galaxy models usually utilize statistical approaches, as simulating the trajectory of every stellar object (stars, planets, etc.) would be hopeless. The central quantities of these models are mass distributions and the resulting gravitational potentials [166,167], in the spirit of classical mechanics. Furthermore, the general aim is the most effective

simulation of the dynamics of galaxies, using the least possible amount of parameters, while preserving the most general features of the galaxies. Most models use axisymmetric mass distributions and potentials, and direct interactions between stellar objects are usually neglected, which turns out to be a good approximation in most cases where the trajectories of objects are separated by great distances, meaning that collisions and close encounters are a rare occurrence [168]. In this way, simple models can be obtained that can easily be reconstructed from observational data.

It is common practice to model the components of galaxies, the central bulge, the disk, and the dark matter halo, using different potentials. The potential of the whole galaxy is then obtained by summing up for the components. A recent study [169] aims to describe galactic dynamics under mass exchange, using the Hernquist (spherical) potential [170] for the bulge, the extended Myamoto-Nagai potential (disk of finite thickness) [171,172] for the disk, and the Navarro–Frenk–White potential [173,174] for the halo, applied for the Milky Way galaxy. In the context of dynamical systems, this is a chaotic Hamiltonian problem with two degrees of freedom, i.e. a four-dimensional phase space. The phase space of the time-independent version of the model treated in [169] can be reduced to two dimensions by Poincaré mapping, since the energy is conserved.

Parameter drift is introduced by decreasing the mass of the disk while simultaneously increasing the mass of the bulge with the same rate. This simple model aims to reproduce the observed process of disk galaxies forming larger classical- and pseudo-bulges, which shows up in different surveys and observations, and is still a relatively unknown process [175,176]. While mass is conserved in the whole system, mechanical energy is not, since the mass exchange effectively results in more contribution from the bulge and less contribution from the disk. Interestingly, because of the different forms of their potentials, this turns out to result in a small gradual decrease in overall energy in the simulations. Since this problem relies on Poincaré sections, the methods described in Section 8.2 can be used. Study [169] follows snapshot tori on a two-dimensional projection, applies the EAPD method, which is easy to use here as well, and also finds that sizeable time-dependent non-hyperbolic regions can be observed in the phase space.

9.4. Plasma physics

Besides the example of galaxy dynamics, the dynamical systems aspects mentioned in Section 8.2 can be relevant to any low-dimensional Hamiltonian system subjected to parameter drift. Among the many possibilities, we discuss here in some detail one particularly relevant field: plasma physics, and sketch two aspects of possible novelty, where there is tremendous potential for future theoretical results, as well as practical applications.

The dynamics of magnetically confined plasmas in fusion reactors follow a set of magnetohydrodynamical (MHD) differential equations [177]. These, however, are not always applicable, in particular if the dynamics of the charged particles becomes chaotic. Alternatively, one can apply the approximation that the particles within the plasma follow the magnetic field lines. This is because the trajectory of the particles is a spiraling motion around a finite magnetic flux, with the so-called Larmor radius and Larmor frequency, however in practice the radius is negligible compared to the size of the reactor, and the frequency is very large [177]. An averaging leads to the conclusion that particles practically move along field lines. Under this assumption, because the magnetic field is divergence-free, the confinement system becomes equivalent to a volume-preserving dynamical system with a three-dimensional phase space [178]. This can be reduced to two by making a Poincaré (or stroboscopic) cut, i.e. only observing the particles at a segment of the plasma chamber at a given toroidal angle (which plays the role of the time-like coordinate), and the magnetic confinement ensures that in this way we obtain an area-preserving Hamiltonian map. This map usually contains at least some macroscopic chaos, and can either be complicated, or as simple as the paradigmatic standard map [179].

Of course, subjecting such systems to parameter drift is a natural extension. This, in the context of a tokamak, would imply the time-dependence of some basic variables, such as components of the magnetic field or a divertor current. In this way we obtain a similar problem as the one mentioned in the previous section. Alternatively, one can study chaotic maps that are designed to reflect the magnetic geometry of tokamak reactors. This was done in a recent study [180] for the time-dependent version of the nontwist map developed by Ullmann and Caldas [181]. This map describes a magnetic configuration perturbed by a so-called ergodic limiter, causing chaotic regions to show up in the outer parts of the plasma. The authors of [180] introduced a linear time-dependence in the ratio of the plasma and limiter currents, and observed snapshot tori as parts of island chains behaving similarly to the ones described here, also evidenced by their EAPD curves. Furthermore, a considerable time-dependent non-hyperbolic region was found to exist, surrounding an island chain close to the boundary between the chaotic and strictly regular parts of the phase space. This time-dependent non-hyperbolic region was visualized by displaying the spatial distribution of the values trajectories contribute to the EAPD function in the chaotic sea. It was found that at a given instant non-hyperbolic trajectories contribute considerably smaller distances than chaotic ones.

The concept of time-dependent non-chaotic or non-hyperbolic regions could especially be relevant for the dynamics of runaway electrons in tokamak reactors, with far reaching consequences to the construction of ITER [182]. Runaway electrons occur when the friction between such electrons and particles of the plasma confined in the reactor cannot sufficiently counterbalance the kinetic energy of the electrons, which then leave the confined population at very high energies [183,184]. The created beam, traveling very fast, is then able to hit various components of the plasma chamber wall (e.g. diagnostic devices), damaging them. Therefore, analyzing the transport of these electrons in maps modeling fusion plasmas is of great importance. The currently best accepted model of non-diffusive plasma transport [185] is based

on the approximation of an exponential decay of the number of particles, i.e. purely chaotic transport in the phase space. This approach neglects the significant presence of elliptic islands within fusion plasma, and with them the effect of the non-hyperbolic regions surrounding them. The inclusion of these regions might already provide a better description of the transport, since it is well known in chaos theory that after the initial exponential decay, a power-law tail takes over for long times, see e.g. [103,186–188]. As a particularly powerful tool for describing the mechanism behind this phenomenon, several models were developed based on the hierarchical structure of microscopic island chains within chaotic seas [189,190]. For reviews on the subject, see [97,191]. For recent findings concerning the properties of the power-law tail, and a possible first step towards application, see [192]. If a parameter drift is introduced, via the presence of e.g. a prescribed time-dependent divertor current, the time-dependent non-hyperbolic regions explored in Section 6.3 could become the appropriate concepts for the description of the non-exponential transport, where a non-trivial function is expected to describe the decay of the particles.

9.5. Engineering applications

There is a number of cases of engineering relevance where some parameter is changing in time either in a controlled way or because of a natural process. Notable examples can be the effect of moving components in machines [193,194], or parameter changes in optical or mechanical systems, where even experiments have been completed [195–197]. In most of these cases however, the drift was chosen to be slow, strictly adiabatic, while the phenomena presented in the paper will only become observable with faster changing parameters. Examples where a non-negligible parameter drift could play a role are e.g. the change of resistance due to an external change of temperature, or ships subjected to waves generated by a wind of increasing strength [198].

Here we explore a case that fits to the overall topics of the paper, by considering a problem related to acceleration or deceleration of rotating machine elements like centrifuges. This, by considering the least possible deviation from the simple model studied throughout the paper, can be illustrated by discussing a version of the Duffing equation in which

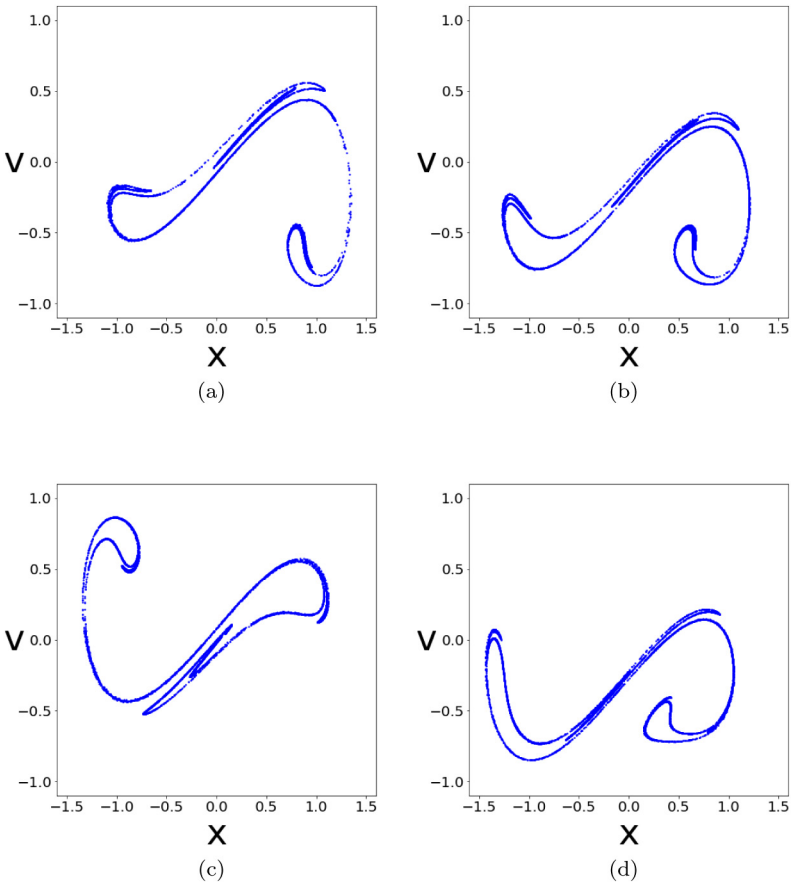

Fig. 47. Snapshot attractor in the scenario $\omega_0 = 1$, $\alpha = 0.001$, $n_{max} = 30$ ($\beta = 0.2$, $\varepsilon = 0.08$) of (60) shown at stroboscopic time instances $n = 15, 20, 25, 30$ in panels (a)–(d), obtained from an extended initial distribution with $N_{ext} = 10000$ particles at time 0.

the driving frequency is drifting. The governing dimensionless equation is then

$$\ddot{x} = x - x^3 - 2\beta\dot{x} + \varepsilon\cos(\omega(t)t), \tag{60}$$

where ε is a fixed driving amplitude, and $\omega(t)$ is a time-dependent driving frequency. To keep similarity with our main example, we choose the frequency to be

$$\omega(t) = \omega_0 + \alpha t, \quad 0 \le t \le t_{max}, \tag{61}$$

where α is again the rate of the parameter drift, i.e. the angular acceleration of the driving signal.

The snapshot attractor can again be obtained as the instantaneous shape of an initially compact ensemble (after a convergence to the attractor took place). Such instances are shown in Fig. 47. Although the driving has no periodic component, we have the freedom to choose a time unit T and take slices at integer multiples of it, again leading to a (non-autonomous) stroboscopic map, yielding $\omega_n = \omega_0 + \alpha nT$ in discrete time. Here, for simplicity, we take integer multiples of the initial period $T = 2\pi/\omega_0$, and follow the scenario over 30 such units. Note that no sign of coexisting other attractors can be observed, we see the evolution of a single chaotic snapshot attractor. A comparison with Figs. 6(b) and 6(c) reveals that the pattern is changing more drastically now. This might be explained by the fact that system (4) is close to an anharmonic oscillator driven with a constant frequency, while here the shift in frequency from 1 to $\omega_{max} = 1.188$ is considerable, therefore the stroboscopic slicing alters the dynamics more significantly.

The main message from an engineering point of view could be that individual simulations (and/or experiments) are to be avoided. Besides the numerical uncertainties, such a simulation would only provide a single point on the (x, v) plane, instead of the extended attractor evolved from ensemble simulations. It is quite clear that the former cannot be a faithful representation of the possible states of the systems, while the latter can, by giving a global overview of all permitted cases.

10. Conclusions

We conclude this review by providing some general thoughts.

The study of drifting systems provides new discoveries in the realm of chaotic dynamics. One important aspect is that the relation between trajectory based and ensemble based simulations should be reevaluated. The constraint of finite time observation cannot be avoided in general, requiring a new attitude concerning mathematical accuracy. Relevant phase space objects and quantities, including chaotic attractors, chaotic seas, natural measures, Lyapunov exponents and escape rates become time-dependent. Foliations turn out to be the basis of phase space structures. In dissipative cases the unstable ones coincide with the snapshot attractors. In Hamiltonian systems stable and unstable foliations differ, and whether one or the other is more closely related to the chaotic subset of the chaotic sea might depend on the type of the scenario. A number of traditional concepts, like e.g. basin and Wada boundaries, strange nonchaotic attractors, KAM tori, non-hyperbolic regions, chaotic scattering, hysteresis, etc., are not only time-dependent, but also call for a redefined approach. The question of adiabaticity, characterizing the speed of the drifting process, becomes especially relevant. We have found a chaos-related new property: adiabaticity might depend on which phase space object is followed within the same scenario. It can also happen that for a given object the process is non-adiabatic first, and then crosses over into being adiabatic.

The essence of chaos is, of course, the presence of a Smale horseshoe, or a chaotic saddle, designated by a multitude of intersection points between the two foliations. In chaotic systems subjected to parameter drift, the saddle is a snapshot chaotic saddle, found to be incorporated into both snapshot attractors and snapshot chaotic seas. Therefore such systems are not only transiently chaotic, but since the strength of transient chaos is changing in time, from this point of view they can be considered as instances of doubly transient chaos in a generalized sense (even if no final asymptotic state exists).

All the examples presented show that chaotic dynamical systems subjected to non-negligible parameter drift possess a plethora of permitted states, whose time dependence should be described by monitoring an ensemble of trajectories. The set of permitted states at an instant is described in dissipative and Hamiltonian cases by the snapshot attractor and the snapshot phase portrait (tori and chaotic seas), respectively. These of course are changing in time, along with the associated natural measure. As a plausible picture behind this view, we can speak of the theory of parallel dynamical evolutions [45] of the systems, in analogy with the theory of parallel climate realizations, introduced earlier [32–34]. This phrase automatically expresses the non-representative nature of any approach based on individual trajectories in drifting chaotic systems.

Declaration of competing interest

The authors declare that they have no known competing financial interests or personal relationships that could have appeared to influence the work reported in this paper.

Acknowledgments

We are grateful for useful discussion with E. Altmann, T. Bódai, R. Börner, G. Drótos, A. El-Aouni, U. Feudel, G. Froyland, M. Ghil, G. Haller, M. Herein, E. Hernández-García, E. Illés, G. Károlyi, B. Kaszás, P. Koltai, T. Kovács, S. Pierini, I.P. Tóth, G. Veres and M. Vincze on different sections of the paper at different stages of its development. We acknowledge the generous support of A. El-Aouni, M. Herein and M. Vincze for permitting us the use of their figures or video snapshots. Special thanks are due to our Editor and the Editorial Office for their assistance during the proofreading process. D.J. was financially supported by the Hungarian National Research, Development and Innovation Office, under Grants No. KDP-2023 C2262591 and TKP-2021 BME-NVA-02, financed by the Ministry of Culture and Innovation of Hungary.

Appendix. Derivation of the snapshot points for polynomial forms of the parameter drift

An observation of (11) suggests that a particular solutions without any exponential contribution can be searched as a linear combination of the ith temporal derivatives $\varepsilon^{(i)}(t)$ of $\varepsilon(t)$ in an infinite series:

$$y^*(t) = \sum_{i=0} \varepsilon^{(i)}(t)(a_i cos\omega t + b_i \sin\omega t), \tag{62}$$

where $\varepsilon(t)$ is of polynomial time-dependence:

$$\varepsilon(t) = \varepsilon_0 + \sum_{j=1}^{\infty} \alpha_j t^j. \tag{63}$$

Substituting this into (11), we obtain similar terms on both sides, and after regrouping, from the vanishing of a given type of term, algebraic equations arise for the coefficients a_i, b_i.

For simplicity, we illustrate the general mechanism with the case of driving amplitudes $\varepsilon(t)$ of quadratic time-dependence (for which the third and higher time derivatives vanish). Therefore, we search for snapshot point orbits in the form of

$$y^*(t) = a_0\varepsilon(t)\cos\omega t + b_0\varepsilon(t)\sin\omega t + a_1\dot{\varepsilon}(t)\cos\omega t + b_1\dot{\varepsilon}(t)\sin\omega t + a_2\ddot{\varepsilon}(t)\cos\omega t + b_2\ddot{\varepsilon}(t)\sin\omega t, \tag{64}$$

valid as long as $|y^*(t)| \ll 1$. Substituting (64) into (11), the vanishing of terms $\varepsilon(t)\cos\omega t$ and $\varepsilon(t)\sin\omega t$ provides two constraints:

$$(\omega^2 - \omega_0^2)a_0 - 2\beta\omega b_0 + 1 = 0, \quad 2\beta\omega a_0 + (\omega^2 - \omega_0^2)b_0 = 0. \tag{65}$$

These determine coefficients a_0, b_0:

$$a_0 = -(\omega^2 - \omega_0^2)/Z, \quad b_0 = 2\beta\omega/Z, \tag{66}$$

where

$$Z = (\omega^2 - \omega_0^2)^2 + (2\beta\omega)^2. \tag{67}$$

These are the same as the a_0, b_0 coefficients in (12). It is worth recognizing that these relations are known from elementary mechanics: εa_0 and εb_0 determine via (13) the limit cycle attractor of the periodically driven harmonic oscillator of eigenfrequency ω_0, damping constant 2β, driven with a constant amplitude ε and driving frequency ω, see e.g. [54,71].

The vanishing of terms $\dot{\varepsilon}(t)\cos\omega t$ and $\dot{\varepsilon}(t)\sin\omega t$ provides the constraints:

$$-2\omega b_0 + a_1(\omega^2 - \omega_0^2) - 2\beta a_0 - 2\beta\omega b_1 = 0, \quad 2\omega a_0 + b_1(\omega^2 - \omega_0^2) - 2\beta b_0 + 2\beta\omega a_1 = 0. \tag{68}$$

These equation make it possible to express a_1, b_1 (the same as in (12)) in terms of the already known coefficients a_0, b_0:

$$a_1 = [-2\beta(\omega^2 + \omega_0^2)a_0 + 2\omega(2\beta^2 + \omega^2 - \omega_0^2)b_0]/Z, \quad b_1 = [-2\omega(2\beta^2 + \omega^2 - \omega_0^2)a_0 - 2\beta(\omega^2 + \omega_0^2)b_0]/Z. \tag{69}$$

Finally, from the vanishing of terms $\ddot{\varepsilon}(t)\cos\omega t$ and $\ddot{\varepsilon}(t)\sin\omega t$ we obtain:

$$-a_0 - 2\omega b_1 + a_2(\omega^2 - \omega_0^2) - 2\beta a_1 - 2\beta\omega b_2 = 0, \quad -b_0 + 2\omega a_1 + b_2(\omega^2 - \omega_0^2) - 2\beta b_1 + 2\beta\omega a_2 = 0. \tag{70}$$

By means of them, coefficients a_2, b_2, describing the new terms compared to (12), can be expressed with a_0, a_1, b_0, b_1 as:

$$\begin{aligned} a_2 =& [(\omega^2 - \omega_0^2)a_0 + 2\beta\omega b_0 - 2\beta(\omega^2 + \omega_0^2)a_1 + 2\omega(2\beta^2 + \omega^2 - \omega_0^2)b_1]/Z, \\ b_2 =& [-2\beta\omega a_0 + (\omega^2 - \omega_0^2)b_0 - 2\omega(2\beta^2 + \omega^2 - \omega_0^2)a_1 - 2\beta(\omega^2 + \omega_0^2)b_1]/Z. \end{aligned} \tag{71}$$

The snapshot point coordinates at stroboscopic instances at $t = nT$ are obtained from (64) as

$$y_n^* = a_0\varepsilon_n + a_1\dot{\varepsilon}_n + a_2 2\alpha_2, \tag{72}$$

where

$$\varepsilon_n = \varepsilon_0 + \alpha_1 nT + \alpha_2(nT)^2, \quad \dot{\varepsilon}_n = \alpha_1 + 2\alpha_2 nT. \tag{73}$$

The difference between the snapshot coordinate $y^*(t)$ and the frozen one $y^*_{frozen}(t)$, given by (13), holds for *any* $\varepsilon(t)$, as well as the spiral-like phase space patterns of the snapshot points, expressed in the form of (16). These properties are valid within the linear approximation applied. No analytic expressions are, however, known for the snapshot points of general drifting nonlinear problems, not even for the Duffing system (4) with a relatively large $\varepsilon(t)$.

References

[1] H.A. Dijkstra, Nonlinear Climate Dynamics, Cambridge University Press, Cambridge, 2013.
[2] M. Ghil, V. Lucarini, The physics of climate variability and climate change, Rev. Modern Phys. 92 (2020) 035002.
[3] C. Deser, Certain uncertainty: The role of internal climate variability in projections of regional climate change and risk management, Earth's Future 8 (2020) e2020EF110854.
[4] L. Suarez-Gutierrez, S. Milinski, N. Maher, Exploiting large ensembles for a better yet simpler climate model evaluation, Clim. Dyn. 57 (9) (2021) 2557–2580, http://dx.doi.org/10.1007/s00382-021-05821-w.
[5] G. Haller, Lagrangian coherent structures and mixing in two-dimensional turbulence, Chaos 10 (2000) 99–108.
[6] E.T. Kai, et al., Top marine predators track Lagrangian coherent structures, Proc. Natl. Acad. Sci. 106 (2009) 8245–8250.
[7] G. Froyland, An analytic framework for identifying finite-time coherent sets in time-dependent dynamical systems, Physica D 250 (2013) 1–19.
[8] G. Haller, Lagrangian coherent structures, Annu. Rev. Fluid Mech. 47 (2015) 137–162.
[9] C. Schneide, M. Stahn, A. Pandey, O. Junge, P. Koltai, K. Padberg-Gehle, J. Schumacher, Lagrangian coherent sets in turbulent Rayleigh-bénard convection, Phys. Rev. E 100 (2019) 053103, http://dx.doi.org/10.1103/PhysRevE.100.053103, URL https://link.aps.org/doi/10.1103/PhysRevE.100.053103.
[10] G. Froyland, P. Koltai, M. Stahn, Computation and optimal perturbation of finite-time coherent sets for aperiodic flows without trajectory integration, SIAM J. Appl. Dyn. Syst. 19 (3) (2020) 1659–1700, http://dx.doi.org/10.1137/19M1261791.
[11] P. Miron, F.J. Beron-Vera, L. Helfmann, P. Koltai, Transition paths of marine debris and the stability of the garbage patches, Chaos 31 (3) (2021) 033101, http://dx.doi.org/10.1063/5.0030535, arXiv:https://pubs.aip.org/aip/cha/article-pdf/doi/10.1063/5.0030535/16648445/033101_1_online.pdf.
[12] G. Haller, Transport Barriers and Coherent Structures in Flow Data, Cambridge University Press, 2023.
[13] G. Froyland, P. Koltai, Detecting the birth and death of finite-time coherent sets, Comm. Pure Appl. Math. 76 (12) (2023) 3642–3684, http://dx.doi.org/10.1002/cpa.22115, arXiv:https://onlinelibrary.wiley.com/doi/pdf/10.1002/cpa.22115, URL https://onlinelibrary.wiley.com/doi/abs/10.1002/cpa.22115.
[14] F.J. Romeiras, C. Grebogi, E. Ott, Multifractal properties of snapshot attractors of random maps, Phys. Rev. A 41 (1990) 784.
[15] P.E. Kloeden, Pullback attractors in non-autonomous difference equations, J. Difference Equ. Appl. 6 (2000) 33.
[16] X. Han, T. Caraballo, Applied Nonautonomous and Random Dynamical Systems: Applied Dynamical Systems, Spinger, New York, 2017.
[17] P.E. Kloeden, M. Yang, Introduction to Nonautonnomous Dynamical Systems and Their Attractors, World Scientific, Singapore, 2021.
[18] M. Ghil, M.D. Chekroun, E. Simonnet, Climate dynamics and fluid mechanics: Natural variability and related uncertainties, Physica D 237 (2008) 2111.
[19] M.D. Chekroun, E. Simonnet, M. Ghil, Stochastic climate dynamics: random attractors and time-dependent invariant measures, Physica D 240 (2011) 1685–1700.
[20] Y.C. Lai, U. Feudel, C. Grebogi, Scaling behavior of transition to chaos in quasiperiodically driven dynamical systems, Phys. Rev. E 54 (6) (1996) 6070.
[21] Y.-C. Lai, Transient fractal behavior in snapshot attractors of driven chaotic systems, Phys. Rev. E 60 (1999) 1558.
[22] R. Serquina, Y.-C. Lai, Q. Chen, Characterization of nonstationary chaotic systems, Phys. Rev. E 77 (2008) 026208.
[23] L. Yu, E. Ott, Q. Chen, Transition to chaos for random dynamical systems, Phys. Rev. Lett. 65 (24) (1990) 2935.
[24] J.C. Sommerer, E. Ott, Particles floating on a moving fluid: a dynamically comprehensible physical fractal, Science 259 (5093) (1993) 335.
[25] J.C. Sommerer, Fractal tracer distributions in complicated surface flows: an application of random maps to fluid dynamics, Physica D 76 (1994) 85–98.
[26] G. Károlyi, T. Tél, A.P.S. de Moura, C. Grebogi, Reactive processes in random flows, Phys. Rev. Lett. 92 (2004) 174101.
[27] K. Guseva, A. Daitche, T. Tél, A snapshot attractor view of the advection of inertial particles in the presence of history force, Eur. Phys. J. Spec. Top. 226 (2017) 2069–2078.
[28] J.L. Hansen, T. Bohr, Fractal tracer distributions in turbulent field theories, Physica D 118 (1998) 40.
[29] W.L. Ku, M. Girvan, E. Ott, Dynamical transitions in large systems of mean field-coupled Landau–Stuart oscillators: Extensive chaos and cluster states, Chaos 25 (2015) 123122.
[30] J. Cantisán, J.M. Seoane, M.A.F. Sanjuán, Transient chaos in time-delayed systems subjected to parameter drift, J. Phys. Complex. 2 (2021) 025001.
[31] T. Kovács, How can contemporary climate research help understand epidemic dynamics? Ensemble approach and snapshot attractors, J. R. Soc. Interface 17 (2020) Article 20200648.
[32] M. Herein, G. Drótos, T. Haszpra, J. Márfy, T. Tél, The theory of parallel climate realizations as a new framework for teleconnection analysis, Sci. Rep. 7 (2017) 44529.
[33] T. Tél, T. Bódai, G. Drótos, T. Haszpra, M. Herein, B. Kaszás, M. Vincze, The theory of parallel climate realizations: A new framework of ensemble methods in a changing climate – an overview, J. Stat. Phys. 179 (2020) 1496.
[34] M. Herein, T. Tél, T. Haszpra, Where are the coexisting parallel climates? Large ensemble climate projections from the point of view of chaos theory, Chaos 33 (2023) 031104.
[35] D. Jánosi, T. Tél, Chaos in Hamiltonian systems subjected to parameter drift, Chaos 29 (2019) 121105.
[36] D. Jánosi, T. Tél, Chaos in conservative discrete-time systems subjected to parameter drift, Chaos 31 (2021) 033142.
[37] Y.-C. Lai, T. Tél, Transient Chaos, Springer, New York, 2011.
[38] B. Kaszás, U. Feudel, T. Tél, Death and revival of chaos, Phys. Rev. E 94 (2016) 062221.
[39] B. Kaszás, U. Feudel, T. Tél, Leaking in history space: A way to analyze systems subjected to arbitrary driving, Chaos 28 (2018) 033612.
[40] J. Jacobs, E. Ott, T. Antonsen, J. Yorke, Modeling fractal entrainment sets of tracers advected by chaotic temporally irregular fluid flows using random maps, Physica D 110 (1997) 1.
[41] Z. Neufeld, T. Tél, Advection in chaotically time-dependent open flows, Phys. Rev. E 57 (1998) 2832.
[42] R.D. Vilela, Doubly transient chaos in a decaying open flow, J. Phys. Complex. 2 (2020) 035013.
[43] T. Haszpra, T. Tél, Escape rate: a Lagrangian measure of particle deposition from the atmosphere, Nonlinear Processes Geophys. 20 (2013) 867–881.

[44] A.C.-L. Chian, S.A. Suzana, S.S.A. Silva, E.L. Rempel, L.R. Bellot Rubio, M. Gošić, K. Kusano, S.-H. Park, Lagrangian chaotic saddles and objective vortices in solar plasmas, Phys. Rev. E 102 (2020).
[45] D. Jánosi, G. Károlyi, T. Tél, Climate change in mechanical systems: the snapshot view of parallel dynamical evolutions, Nonlinear Dynam. 106 (2021) 2781–2805.
[46] D. Jánosi, T. Tél, Characterizing chaos in systems subjected to parameter drift, Phys. Rev. E 105 (2022) L062202.
[47] T. Bódai, T. Tél, Annual variability in a conceptual climate model: Snapshot attractors, hysteresis in extreme events, and climate sensitivity, Chaos 22 (2012) 023110.
[48] D. Patel, D. Canaday, M. Girwan, A. Pomerance, E. Ott, Using machine learning to predict statistical properties of non-stationary dynamical processes: System climate, regime transitions, and the effect of stochasticity, Chaos 31 (2021) 033149.
[49] J. Argyris, G. Faust, M. Haase, R. Friedrich, An Exploration of Dynamical Systems and Chaos, Springer, New York, 2015.
[50] A. Hadjighasem, M. Farazmand, G. Haller, Detecting invariant manifolds, attractors and generalized KAM tori in aperiodically forced mechanical systems, Nonlinear Dynam. 73 (2013) 689.
[51] T. Kapitaniak, Chaos for Engineers, Springer, Berlin, 2000.
[52] T. Nishikawa, E. Ott, Controlling systems that drift through a tipping point, Chaos 24 (2014) 033107.
[53] B. Kaszás, U. Feudel, T. Tél, Tipping phenomena in typical dynamical systems subjected to parameter drift, Sci. Rep. 9 (2019) 8654.
[54] L. Landau, E. Lifshitz, Mechanics, third ed., Butterworth-Heinemann, 1976, http://dx.doi.org/10.1016/B978-0-08-050347-9.50005-8.
[55] E. Ott, Goodness of ergodic adiabatic invariants, Phys. Rev. Lett. 42 (1979) 1628–1631, http://dx.doi.org/10.1103/PhysRevLett.42.1628, URL https://link.aps.org/doi/10.1103/PhysRevLett.42.1628.
[56] R. Brown, E. Ott, C. Grebogi, Ergodic adiabatic invariants of chaotic systems, Phys. Rev. Lett. 59 (1987) 1173–1176, http://dx.doi.org/10.1103/PhysRevLett.59.1173, URL https://link.aps.org/doi/10.1103/PhysRevLett.59.1173.
[57] G. Haller, R. S. Kaundinya, Nonlinear model reduction to temporally aperiodic spectral submanifolds, Chaos 34 (4) (2024) 043152, http://dx.doi.org/10.1063/5.0187080, arXiv:https://pubs.aip.org/aip/cha/article-pdf/doi/10.1063/5.0187080/19904332/043152_1_5.0187080.pdf.
[58] P. Ashwin, S. Wieczorek, R. Vitolo, P. Cox, Tipping points in open systems: Bifurcation, noise-induced and rate-dependent examples in the climate system, Phil. Trans. R. Soc. A 370 (2012) 1166–1184.
[59] A.S. Pikovskii, Synchronization and stochastization of array of self-excited oscillators by external noise, Radiophys. Quantum Electron. 27 (5) (1984) 390–395, http://dx.doi.org/10.1007/BF01044784.
[60] G.R. Sell, Nonautonomous dfferential equations and dynamical systems, Trans. Amer. Math. Soc. 127 (1967) 241–283.
[61] C. Kuehn, Multiple Time Scale Dynamics, Springer, New York, 2015.
[62] G. Károlyi, R.D. Prokaj, I. Scheuring, T. Tél, Climate change in a conceptual atmosphere–phytoplankton model, Earth Syst. Dyn. 11 (3) (2020) 603–615, http://dx.doi.org/10.5194/esd-11-603-2020, URL https://esd.copernicus.org/articles/11/603/2020/.
[63] K. Ide, D. Small, S. Wiggins, Distinguished hyperbolic trajectories in time-dependent fluid flows: analytical and computational approach for velocity fields defined as data sets, Nonlinear Processes Geophys. 9 (2002) 237–263.
[64] S. Wiggins, Introduction to Applied Nonlinear Dynamical Systems and Chaos, second ed., Springer, Berlin, 2003.
[65] M. Mathur, G. Haller, T. Peacock, J.-E. Ruppert-Felsot, H.L. Swinney, Uncovering the Lagrangian skeleton of turbulence, Phys. Rev. Lett. 98 (2007) 144502.
[66] P. Ritchie, J. Sieber, Early-warning indicators for rate-induced tipping, Chaos 26 (2016) 093116.
[67] P. Ashwin, C. Perryman, S. Wieczorek, Parameter shifts for nonautonomous systems in low dimension: bifurcation- and rate-induced tipping, Nonlinearity 30 (2017) 2185.
[68] S. Wieczorek, X. Chun, P. Ashwin, Rate-induced tipping: Thresholds, edge states and connecting orbits, Nonlinearity 36 (2023) 3238–3293.
[69] X. Zhang, Y. Xu, Q. Liu, et al., Rate-dependent bifurcation dodging in a thermoacoustic system driven by colored noise, Nonlinear Dynam. 104 (2021) 2733–2743.
[70] A.K. Klose, J.F. Donges, U. Feudel, R. Winkelmann, Rate-induced tipping cascades arising from interactions between the greenland ice sheet and the atlantic meridional overturning circulation, Earth Syst. Dyn. 15 (2024) 635–652.
[71] S.T. Thornton, J.B. Marion, Classical Dynamics of Particles and Systems, fifth ed., Thomson Learning, Belmont, USA, 2004.
[72] P. Cvitanovic, R. Artuso, R. Mainieri, G. Tanner, G. Vattay, Chaos: Classical and quantum, ChaosBook.org, 2020, edition16.4.8.
[73] G. Drótos, T. Bódai, T. Tél, Quantifying nonergodicity in nonautonomous dissipative dynamical systems: An application to climate change, Phys. Rev. E 94 (2016) 022214.
[74] T. Bódai, G. Drótos, K.-J. Ha, J.-Y. Lee, E.-S. Chung, Nonlinear forced change and nonergodicity: The case of ENSO-Indian monsoon and global precipitation teleconnections, Front. Earth Sci. 8 (2021) http://dx.doi.org/10.3389/feart.2020.599785, URL https://www.frontiersin.org/journals/earth-science/articles/10.3389/feart.2020.599785.
[75] J.P. Eckmann, D. Ruelle, Ergodic theory of chaos and strange attractors, Rev. Modern Phys. 57 (1985) 617–656.
[76] A.E. Motter, M. Gruiz, G. Károlyi, T. Tél, Doubly transient chaos: Generic form of chaos in autonomous dissipative systems, Phys. Rev. Lett. 111 (2013) 194101.
[77] Y.G. Sinai, Dynamical systems with elastic reflections, Russian Math. Surveys 25 (1970) 137.
[78] Y.B. Pesin, Y.G. Sinai, Gibbs measures for partially hyperbolic attractors, Ergodic Theory Dynam. Systems 2 (1982) 417.
[79] D. Ruelle, Elements of differentiable Dynamics and Bifurcation Theory, Elsevier, 1989.
[80] S. Wiggins, Normally Hyperbolic Invariant Manifolds in Dynamical Systems, Spinger, New York, 1994.
[81] S. Smale, Differentiable dynamical systems, Bull. Amer. Math. Soc. 73 (1967) 747–817, http://dx.doi.org/10.1090/S0002-9904-1967-11798-1.
[82] E. Ott, Chaos in Dynamical Systems, Cambridge U. Press, Cambridge, 1993.
[83] B. Hunt, E. Ott, Defining chaos, Chaos 25 (2015) 097618.
[84] S. Pierini, M. Ghil, D. Chekroun, Exploring the pullback attractors of a low-order quasigeostrophic ocean model: the deterministic case, J. Clim. 29 (2016) 4185–4202.
[85] S. Pierini, D. Chekroun, M. Ghil, The onset of chaos in nonautonomous dissipative dynamical systems: A low-order ocean–model case study, Nonlinear Proc. Geophys. 25 (2018) 671–692.
[86] T. Tél, M. Gruiz, Chaotic Dynamics, Cambridge University Press, Cambridge, New York, 2006.
[87] P. Gaspard, Chaos, Scattering and Statistical Mechanics, Cambridge University Press, Cambridge, 2005.
[88] H. Risken, The Fokker-Planck Equation, second ed., Springer, 1996.
[89] C.W. Gardiner, Handbook of Stochastic Methods, Springer, New York, 1983.
[90] V. Lembo, V. Lucarini, F. Ragone, Beyond forcing scenarios: Predicting climate change through response operators in a coupled general circulation model, Sci. Rep. 10 (2020) 8668.
[91] T. Bódai, G. Károlyi, T. Tél, A chaotically driven model climate: extreme events and snapshot attractors, Nonlinear Processes Geophys. 18 (2011) 573–580.
[92] M. Ghil, A mathematical theory of climate sensitivity or, how to deal with both anthropogenic forcing and natural variability? in: Climate Change: Multidecadal and beyond, World Scientifc, Singapore, 2013, pp. 31–51.
[93] G. Drótos, T. Bódai, T. Tél, Probabilistic concepts in a changing climate: A snapshot attractor picture, J. Clim. 28 (2015) 3275.

[94] T. Bódai, G. Károlyi, T. Tél, A chaotically driven model climate: extreme events and snapshot attractors, Nonlinear Processes Geophys. 18 (2011) 573–580.
[95] T. Bódai, G. Károlyi, T. Tél, Fractal snapshot components in chaos induced by strong noise, Phys. Rev. E 83 (2011) 046201, http://dx.doi.org/10.1103/PhysRevE.83.046201, URL https://link.aps.org/doi/10.1103/PhysRevE.83.046201.
[96] G.-H. Hsu, E. Ott, C. Grebogi, Strange saddles and the dimensions of their invariant manifolds, Phys. Lett. A 127 (4) (1988) 199–204, http://dx.doi.org/10.1016/0375-9601(88)90102-8, URL https://www.sciencedirect.com/science/article/pii/0375960188901028.
[97] E.G. Altmann, J.S.E. Portela, T. Tél, Leaking chaotic systems, Rev. Modern Phys. 85 (2013) 869–918.
[98] U. Feudel, S. Kuznetsov, A. Pikovsky, Strange Nonchaotic Attractors, World Scientific, Singapore, 2006.
[99] J. Duan, Z. Wei, G. Li, D. Li, C. Grebogi, Strange nonchaotic attractors in a class of quasiperiodically forced piecewise smooth systems, Nonlinear Dynam. (2024) http://dx.doi.org/10.1007/s11071-024-09678-6.
[100] K. Kennedy, J.A. Yorke, Basins of wada, Physica D 51 (1991) 213–225.
[101] H. Kantz, R. P. Grassberger, semi-attractors, and long-lived chaotic transients, Physica D 17 (1985) 75–86.
[102] A. Katok, Fifty years of entropy in dynamics: 1958–2007, J. Mod. Dyn. 2007 (2007) 545–596.
[103] G. Cristadoro, R. Ketzmerick, Universality of algebraic decays in Hamiltonian systems, Phys. Rev. Lett. 100 (2008) 184101.
[104] B. Mandelbrot, The Fractal Geometry of Nature, W.H. Freeman, 1982.
[105] A. Rényi, Probability Theory, North Holland, 1970.
[106] P. Grassberger, I. Procaccia, Measuring the strangeness of strange attractors, Physica D 9 (1983) 189–2008.
[107] P. Grassberger, I. Procaccia, Characterization of strange attractors, Phys. Rev. Lett. 50 (1983) 346–349.
[108] H.G.E. Hentschel, T. I. Procaccia, Infinite number of generalized dimensions of fractals and strange attractors, Physica D 8 (1983) 435–444.
[109] P. Grassberger, Generalized dimensions of strange attractors, Phys. Lett. A 97 (1983) 227–230.
[110] T.C. Halsey, M.H. Jensen, L.P. Kadanoff, I. Procaccia, B.I. Shraiman, Fractal measures and their singularities: The characterization of strange sets, Phys. Rev. A 33 (1986) 1141.
[111] P. Frederickson, J. Kaplan, E. Yorke, J. Yorke, The Lyapunov dimension of strange attractors, J. Differential Equations 49 (1983) 185–207.
[112] E. Ott, T.M. Antonsen, Fractal measures of passively convected vector fields and scalar gradients in chaotic fiuid flows, Phys. Rev. A 39 (1989) 3660–3671.
[113] T. Bódai, E.G. Altmann, A. Endler, Stochastic perturbations in open chaotic systems: Random versus noisy maps, Phys. Rev. E 87 (2013) 042902, http://dx.doi.org/10.1103/PhysRevE.87.042902, URL https://link.aps.org/doi/10.1103/PhysRevE.87.042902.
[114] F. Ledrappier, L.S. Young, Dimension formula for random transformations, Comm. Math. Phys. 117 (1988) 529–548.
[115] A. Namenson, E. Ott, T.M. Antonsen, Fractal dimension fluctuations for snapshot attractors of random maps, Phys. Rev. E. 53 (1996) 2287–2291.
[116] P. Ashwin, J. Newman, Physical invariant measures and tipping probabilities for chaotic attractors of asymptotically autonomous systems, Eur. Phys. J. SPec. Top. 230 (2021) 3235–3248.
[117] V. Lucarini, K. Fraedrich, F. Lunkeit, Thermodynamic analysis of snowball Earth hysteresis experiment: Efficiency, entropy production and irreversibility, Q. J. R. Meteorol. Soc. 136 (646) (2010) 2–11, http://dx.doi.org/10.1002/qj.543, arXiv:https://rmets.onlinelibrary.wiley.com/doi/pdf/10.1002/qj.543, URL https://rmets.onlinelibrary.wiley.com/doi/abs/10.1002/qj.543.
[118] I. Bordi, K. Fraedrich, A. Sutera, X. Zhu, Transient response to well mixed greenhouse gas changes, Theor. Appl. Climatol. 109 (1992) 245–252.
[119] G. Károlyi, T. Tél, New features of doubly transient chaos: complexity of decay, J. Phys. Complex. 2 (2021) 035001.
[120] P. Nagy, P. Tasnádi, Irregular chaos in a bowl, in: E. Dębowska, T. Greczyło (Eds.), Key Competences in Physics Teaching and Learning, Proceedings of GIREP EPEC 2015, Institute of Experimental Physics, Wrocław, 2016, pp. 262–269.
[121] P. Nagy, P. Tasnádi, Double transient chaotic behaviour of a rolling ball, Open Access J. Phys. 2 (2018) 11.
[122] X. Chen, T. Nishikawa, A.E. Motter, Slim fractals: The geometry of doubly transient chaos, Phys. Rev. X 7 (2017) 021040.
[123] L.G. Burton, H.R. Dullin, E.G. Altmann, Probabilistic description of dissipative chaotic scattering, Phys. Rev. E 108 (2023) 054223.
[124] J.M. Seoane, M.A.F. Sanjuán, New developments in classical chaotic scattering, Rep. Prog. Phys. 76 (2013) 016001.
[125] A. Celletti, L. Stefanelli, E. Lega, C. Froeschlé, Some results on the global dynamics of the regularized restricted three-body problem with dissipation, Celest. Mech. Dyn. Astr. 109 (2011) 265.
[126] G. Drótos, M. Herein, T. Haszpra, I.M. Jánosi, Converged ensemble simulations of climate: possible trends in total solar irradiance cannot explain global warming alone, Front. Earth Sci. 12 (2024) http://dx.doi.org/10.3389/feart.2024.1240784, URL https://www.frontiersin.org/journals/earth-science/articles/10.3389/feart.2024.1240784.
[127] G. Danabasoglu, J.-F. Lamarque, J. Bacmeister, D.A. Bailey, A.K. DuVivier, J. Edwards, et al., The community earth system model version 2 (CESM2), J. Adv. Model. Earth Syst. 12 (2020) e2019MS001916.
[128] J.E. Kay, et al., The community earth system model (CESM) large ensemble project: A community resource for studying climate change in the presence of internal climate variability, Bull. Am. Meteorol. Soc. 96 (2015) 1333–1349.
[129] T. Haszpra, M. Herein, Ensemble-based analysis of the pollutant spreading intensity induced by climate change, Sci. Rep. 9 (1) (2019) 3896, http://dx.doi.org/10.1038/s41598-019-40451-7.
[130] N. Maher, S. Milinski, R. Ludwig, Large ensemble climate model simulations: Introduction, overview, and future prospects for utilising multiple types of large ensemble, Earth Syst. Dyn. 12 (2021) 401–418.
[131] K. Fraedrich, H. Jansen, E. Kirk, U. Luksch, F. Lunkeit, The planet simulator: Towards a user friendly model, Meteorol. Z. 14 (3) (2005) 299–304.
[132] M. Herein, D. Jánosi, T. Tél, An ensemble based approach for the effect of climate change on the dynamics of extremes, Front. Earth Sci. 11 (2023) Article 1267473.
[133] C. Deser, et al., Insights from earth system model initial-condition large ensembles and future prospects, Nature Clim. Change 10 (2020) 277–286.
[134] S. Milinski, N. Maher, D. Olonscheck, How large does a large ensemble need to be? Earth Syst. Dyn. 11 (2020) 885–901.
[135] S. Pierini, Statistical significance of small ensembles of simulations and detection of the internal climate variability: An excitable ocean system case study, J. Stat. Phys. 179 (2020) 1475–1495.
[136] G. Drótos, T. Bódai, T. Tél, On the importance of the convergence to climate attractors, Eur. Phys. J. Spec. Top. 226 (2017) 2031–2038.
[137] G. Drótos, T. Bódai, On defining climate by means of an ensemble, Authorea 10 (1002) (2022) 1–35.
[138] S. Pierini, M. Ghil, Climate tipping points induced by parameter drift: an excitable system study, Sci. Rep. 11 (2021) 11126.
[139] J.D. Skufca, J.A. Yorke, B. Eckhardt, Edge of chaos in a parallel shear flow, Phys. Rev. Lett. 96 (2006) 1741011.
[140] V. V. Lucarini, T. Bódai, Edge states in the climate system: exploring global instabilities and critical transitions, Nonlinearity 30 (2017) R32.
[141] B. Kaszás, T. Haszpra, M. Herein, The snowball earth transition in a climate model with drifting parameters: Splitting of the snapshot attractor, Chaos 29 (2019) 113102.
[142] M. Ghil, I. Zaliapin, Understanding ENSO variability and its extrema, in: M. Chavez, M. Ghil, J. Urrutia-Fucugauchi (Eds.), Extreme Events: Observations, Modeling and Economics, American Geophysical Union, Wiley, 2015, pp. 63–78.
[143] T. Haszpra, M. Herein, T. Bódai, Investigating ENSO and its teleconnections under climate change in an ensemble view - A new perspective, Earth Syst. Dyn. 11 (2020) 267–280.

[144] T. Bódai, et al., The forced response of the El Niño–Southern Oscillation–Indian Monsoon teleconnection in ensembles of Earth System, Models, J. Clim. 33 (2020) 2163–2182.
[145] J. Ma, P. Lin, L. Wang, B. Zhao, H. Xu, Increasing connections of the leading internal mode of the summertime northwest Pacific subtropical anticyclone with preceding ENSO under greenhouse warming in FGOALS "g3 super" large ensemble, Int. J. Climatol. 43 (13) (2023) 6164–6178.
[146] T. Haszpra, D. Topál, M. Herein, On the time evolution of the arctic oscillation and related wintertime phenomena under different forcing scenarios in an ensemble approach, J. Clim. 33 (2020) 3107–3124.
[147] T. Haszpra, D. Topál, M. Herein, Detecting forced changes in internal variability using large ensembles: On the use of methods based on the "snapshot view", US CLIVAR Var. 18 (2020) 36–43.
[148] J.P. O'Brien, C. Deser, Quantifying and understanding forced changes to unforced modes of atmospheric circulation variability over the North Pacific in a coupled model large ensemble, J. Clim. 26 (2023) 19–37.
[149] G. Ansmann, R. Karnatak, K. Lehnertz, U. Feudel, Extreme events in excitable systems and mechanisms of their generation, Phys. Rev. E 88 (2013) 052911, http://dx.doi.org/10.1103/PhysRevE.88.052911, URL https://link.aps.org/doi/10.1103/PhysRevE.88.052911.
[150] A. Mishra, S. Leo Kingston, C. Hens, T. Kapitaniak, U. Feudel, S.K. Dana, Routes to extreme events in dynamical systems: Dynamical and statistical characteristics, Chaos 30 (6) (2020) 063114, http://dx.doi.org/10.1063/1.5144143, arXiv:https://pubs.aip.org/aip/cha/article-pdf/doi/10.1063/1.5144143/14627171/063114_1_online.pdf.
[151] C.L.E. Franzke, Changing temporal volatility of precipitation extremes due to global warming, Int. J. Climatol. 42 (16) (2022) 8971–8983, http://dx.doi.org/10.1002/joc.7789, arXiv:https://rmets.onlinelibrary.wiley.com/doi/pdf/10.1002/joc.7789, URL https://rmets.onlinelibrary.wiley.com/doi/abs/10.1002/joc.7789.
[152] M. Vincze, C. Hancock, U. Harlander, C. Rodda, K. Speer, Extreme temperature fluctuations in laboratory models of the mid-latitude atmospheric circulation, Sci. Rep. 13 (1) (2023) 20904, http://dx.doi.org/10.1038/s41598-023-47724-2.
[153] M. Vincze, I. Dan Borcia, U. Harlander, Temperature fluctuations in a changing climate: an ensemble based experimental approach, Sci. Rep. 7 (2017) 254.
[154] J.M. Ottino, The Kinematics of Mixing: Stretching, Chaos, and Transport, Cambridge University Press, Cambridge, 1989.
[155] H. Aref, Stirring by chaotic advection, J. Fluid Mech. 143 (1984) 1–21, http://dx.doi.org/10.1017/S0022112084001233.
[156] G. Haller, A.C. Poje, Finite time transport in aperiodic flows, Physica D 119 (1998) 352–380.
[157] A.M. Mancho, D. Small, S. Wiggins, A tutorial on dynamical systems concepts applied to Lagrangian transport in oceanic flows defined as finite time data set: theoretical and computational issues, Phys. Rep. 437 (2006) 55–124.
[158] G. Haller, A. Hadjighasem, M. Farazmand, F. Huhn, Defining coherent vortices objectively from the vorticity, J. Fluid Mech. 795 (2016) 136–173.
[159] M. Farazmand, G. Haller, Polar rotation angle identifies elliptic islands in unsteady dynamical systems, Physica D 315 (2016) 1–12, http://dx.doi.org/10.1016/j.physd.2015.09.007, URL https://www.sciencedirect.com/science/article/pii/S0167278915001748.
[160] T. Tél, L. Kadi, I.M. Jánosi, M. Vincze, Experimental demonstration of the waterholding property of three-dimensional vortices, Eur. Phys. Lett. 123 (2018) 44001.
[161] T. Tél, I.M. Jánosi, M. Vincze, Vortices capturing matter: a classroom demonstration, Phys. Educ. 55 (2020) 015007.
[162] A.E. Aouni, K. Daoudi, H. Yahia, K. Minaoui, A. Benazzouz, Surface mixing and biological activity in the North-West African upwelling, Chaos 29 (2019) 011104.
[163] A.E. Aouni, V. Garçon, J. Sudre, H.M. Yahia, K. Daoudi, K. Minaoui, Physical and biological satellite observations of the Northwest African upwelling: Spatial extent and dynamics, IEEE Trans. Geosci. Remote Sens. 58 (2020) 1409.
[164] A.E. Aouni, A hybrid identification and tracking of Lagrangian mesoscale eddies, Phys. Fluids 33 (2021) 036604.
[165] A.E. Aouni, Lagrangian Coherent Structures and Physical Processes of Coastal Upwelling (Ph.D. thesis), University Bourdeaux, 2019.
[166] J.N. Bahcall, R.M. Soneira, Star counts as an indicator of galactic structure and quasar evolution, APJL 238 (1980) L17–L20, http://dx.doi.org/10.1086/183248.
[167] J.A.R. Caldwell, J.P. Ostriker, The mass distribution within our Galaxy - A three component model, APJ 251 (1981) 61–87, http://dx.doi.org/10.1086/159441.
[168] D. Maoz, Astrophysics in a Nutshell, second ed., Princeton Univ. Press, 2016.
[169] E. Illés, D. Jánosi, T. Kovács, Orbital dynamics in galactic potentials under mass transfer, Astron. Astrophys. (2024) submitted for publication.
[170] L. Hernquist, An analytical model for spherical galaxies and bulges, APJ 356 (1990) 359, http://dx.doi.org/10.1086/168845.
[171] M. Miyamoto, R. Nagai, Three-dimensional models for the distribution of mass in galaxies, PASJ 27 (1975) 533–543.
[172] D. Vogt, P.S. Letelier, On Multipolar Analytical Potentials for Galaxies, Publ. Astron. Soc. Japan 57 (6) (2005) 871–875, http://dx.doi.org/10.1093/pasj/57.6.871, arXiv:https://academic.oup.com/pasj/article-pdf/57/6/871/54710741/pasj_57_6_871.pdf.
[173] J.F. Navarro, C.S. Frenk, S.D.M. White, The Structure of Cold Dark Matter Halos, APJ 462 (1996) 563, http://dx.doi.org/10.1086/177173, arXiv:astro-ph/9508025.
[174] R.E. Sanderson, J. Hartke, A. Helmi, Modeling the gravitational potential of a cosmological dark matter halo with stellar streams, Astrophys. J. 836 (2) (2017) 234, http://dx.doi.org/10.3847/1538-4357/aa5eb4.
[175] L. Domínguez-Palmero, M. Balcells, The nature of growing bulges within z < 1.3 galaxy disks in the goods-n field, Astrophys. J. 694 (1) (2009) L69, http://dx.doi.org/10.1088/0004-637X/694/1/L69.
[176] A. Hashemizadeh, The Emergence of Bulges and Disks in the Universe (Ph.D. thesis), The University of Western Australia, 2020.
[177] J.P. Goedbloed, S. Poedts, Principles of magnetohydrodynamics, Cambridge University Press, 2004.
[178] J.S.E. Portela, I.L. Caldas, R.L. Viana, Tokamak magnetic field lines described by simple maps, Eur. Phys. J. Spec. Top. 165 (1) (2008) 195–210, http://dx.doi.org/10.1140/epjst/e2008-00863-y.
[179] D.F. Escande, Contributions of plasma physics to chaos and nonlinear dynamics, Plasma Phys. Control. Fusion 58 (11) (2016) 113001, http://dx.doi.org/10.1088/0741-3335/58/11/113001.
[180] D. Jánosi, A. Horváth, L. Édes, T. Kovács, Magnetic structures in the explicitly time-dependent nontwist map, Chaos (2024) submitted for publication.
[181] K. Ullmann, I. Caldas, A symplectic mapping for the ergodic magnetic limiter and its dynamical analysis, Chaos Solitons Fractals 11 (13) (2000) 2129–2140, http://dx.doi.org/10.1016/S0960-0779(99)00138-1, URL https://www.sciencedirect.com/science/article/pii/S0960077999001381.
[182] S. Abdullaev, Magnetic Stochasticity in Magnetically Confined Fusion Plasmas — Chaos of Field Lines and Charged Particle Dynamics, Springer, 2014.
[183] B.N. Breizman, P. Aleynikov, E.M. Hollmann, M. Lehnen, Physics of runaway electrons in tokamaks, Nucl. Fusion 59 (8) (2019) 083001, http://dx.doi.org/10.1088/1741-4326/ab1822.
[184] J. Zebrowski, L. Jakubowski, M. Rabinski, M.J. Sadowski, M.J. Jakubowski, R. Kwiatkowski, K. Malinowski, R. Mirowski, J. Mlynar, O. Ficker, V. Weinzettl, F. Causa, COMPASS, FTU Teams, Studies of runaway electrons via Cherenkov effect in tokamaks, J. Phys. Conf. Ser. 959 (1) (2018) 012002, http://dx.doi.org/10.1088/1742-6596/959/1/012002.
[185] A.B. Rechester, M.N. Rosenbluth, Electron heat transport in a tokamak with destroyed magnetic surfaces, Phys. Rev. Lett. 40 (1978) 38–41, http://dx.doi.org/10.1103/PhysRevLett.40.38, URL https://link.aps.org/doi/10.1103/PhysRevLett.40.38.
[186] S.R. Channon, J.L. Lebowitz, Numerical experiment in stochasticity and homoclinic oscillation, Ann. New York Acad. Sci. 357 (1980) 108–118.

[187] C.F. Karney, Long-time correlations in the stochastic regime, Physica D 8 (1983) 360–380, arXiv:nlin/0501023.
[188] J.D. Meiss, J.R. Cary, C. Grebogi, J.D. Crawford, A.N. Kaufman, H.D. Abarbanel, Correlations of periodic, area-preserving maps, Physica D 6 (1983) 375–384.
[189] J.D. Meiss, E. Ott, Markov-tree model of intrinsic transport in Hamiltonian systems, Phys. Rev. Lett. 55 (1985) 2741–2744.
[190] Y.T. Lau, J.M. Finn, E. Ott, Fractal dimension in nonhyperbolic chaotic scattering, Phys. Rev. Lett. 66 (1991) 978–981.
[191] J.D. Meiss, Thirty years of turnstiles and transport, Chaos 25 (2015) 097602.
[192] D. Jánosi, G. Károlyi, Macroscopic transport in mixed phase space Hamiltonian systems and the role of a distinct time-scale for the power-law decay, Chaos 34 (8) (2024) 081104, http://dx.doi.org/10.1063/5.0216731, arXiv:https://pubs.aip.org/aip/cha/article-pdf/doi/10.1063/5.0216731/20120535/081104_1_5.0216731.pdf.
[193] I.G. Tadibakhsh, Y.-M. Wangm, Transient vibrations of a tau inclined cable with a riding accelerating mass, Nonlinear Dynam. 6 (1994) 143.
[194] Z. Dombóvári, J. Munoa, R. Kuske, G. Stépán, Milling stability for slowly varying parameters, Procedia CIRP 77 (2018) 110.
[195] R.S. Chancellor, R.M. Alexander, S.T. Noah, Detecting Parameter Changes Using Experimental Nonlinear Dynamics and Chaos, J. Vib. Acoust. 118 (3) (1996) 375–383, http://dx.doi.org/10.1115/1.2888193, arXiv:https://asmedigitalcollection.asme.org/vibrationacoustics/article-pdf/118/3/375/5625803/375_1.pdf.
[196] A. Amon, M. Lefranc, Topological signature of deterministic chaos in short nonstationary signals from an optical parametric oscillator, Phys. Rev. Lett. 92 (2004) 094101.
[197] A. Chatteerjee, J.P. Cusumano, A. Chelidze, Optimal tracking of parameter drift in a chaotic system: Experiment and theory, J. Sound Vib. 250 (2002) 877–901.
[198] J.M.T. Thompson, R.C.T. Rainey, M.S. Soliman, Mechanics of ship capsize under direct and parametric wave excitation, Philos. Trans. R. Soc. 338 (1992) 471.